ABSTRACT

Title of Thesis: CATEGORIZING ADMITTANCE CONTROL
                                    PARAMETERS FOR THE RANGER 8-DOF
                                    TELE-OPERATED SPACE MANIPULATOR.

                                    Enrico Sabelli, Master of Science, 2007

Thesis Directed By: Dr. David L. Akin, Associate Professor,
                                    Department of Aerospace Engineering

Position-based admittance control of a robotic manipulator is a strategy that allows the manipulator to achieve compliance without sacrificing positional accuracy or modifying the underlying position controller. Desired manipulator stiffness and damping can be specified so that the tool tip behaves as a spring-dashpot system. This work characterizes the range of parameters that allows stable task execution in contact with an environment of varying stiffness for the Ranger dexterous manipulator. A classical stability analysis and simulation of the controller is conducted to predict its response in contact. The manipulator's behavior is then observed during a series of simple tasks involving contact in one and two degrees of freedom. Suitable gains are chosen such that interaction forces at the tool tip are kept low. A compliant peg-in-hole insertion task is successfully accomplished. The work also outlines the implementation of an algorithm that removes unwanted gravity forces measured at the tool tip.

CATEGORIZING ADMITTANCE CONTROL PARAMETERS FOR THE
RANGER 8-DOF TELE-OPERATED SPACE MANIPULATOR.

By

Enrico Sabelli

Thesis submitted to the Faculty of the Graduate School of the
University of Maryland, College Park, in partial fulfillment
of the requirements for the degree of
Master of Science
2007

Advisory Committee:
Associate Professor David L. Akin , Chair
Associate Professor Robert M. Sanner
Dr. Craig R. Carignan

Dedication

Per i miei Nonni.

Acknowledgements

A big thank-you goes out to my advisor Dave Akin, not just for his time and guidance, but mostly for his contagious enthusiasm for all that is space-related. Just seeing his face light up when you show him even the most insignificant hardware is all the motivation you need sometimes. To my other committee members, Craig Carignan and Rob Sanner, thanks for letting me pick your brains, for your valuable and expeditious feedback, and for fueling my interest in robotics and control.

Working in this lab with so many talented teammates has been a blessing. The spirit of cooperation here is unparalleled, and I hope it never changes. To my friends and colleagues who have been there from day one, or those I only met this year, thanks for making the SSL such a lively place to do research.

Stephen Roderick, my guru, I truly could not have finished this without you. I know I'm not the first to tell you that, and I certainly will not be the last. Your patience in dealing with my programming ineptitudes will not be forgotten.

Nathan, Leon, Nick, I couldn't have stayed sane through the weekends or the late nights without the laughs, the racquetball, or the re-fueling trips to Wawa. Tim, the "Kim cot" was the best idea ever. I don't know how I'll be able to work a real job after 3:00 pm without a siesta. Teresa, thanks for always being there. I told you we'd make it! Lynn, thanks for making this experience a little crazier. Shaner, thanks for

being a great leader; keep making Canada proud. I intend on hearing about all your accolades from across the border. To everyone else I've met here, thanks for the memories, the nerdy discussions, and especially for driving my car-less self around. I promise that if you're ever in my neck of the woods and need a ride, I'll be your personal chauffeur.

To my friends in Montreal, un gros merci, especially to Andreea, Maria and Robert, for encouraging me to do this, for always being a phone call or a few keystrokes away, and for always having more faith in me than I did. PJ, Steve, Liz, Franco, Mauro, thanks for bringing home here when I needed it.

Last, but certainly not least, a heartfelt thanks to my family for their endless support, for tying up my loose ends, and for never making a big deal every time I'd tell them it would be a little longer before I came back.

Finally, I cannot forget to thank the man upstairs for keeping me calm when no one else was around.

Table of Contents

List of Tables

List of Figures

Chapter 1

Introduction

Background

1.1.1 Robots in Space

Since human presence is limited in both location and numbers, the vast majority of space exploration depends on robotic systems. While the cost associated with human space exploration may be prohibitive for financially limited countries, by developing more expendable robotic systems, more nations can afford to participate in the exploration of space at the same level.

Robotic missions are now commonly proposed and carried out as precursors or replacements of their human extravehicular activity (EVA) equivalents. For example, a robotic mission to service the Hubble Space Telescope was planned and demonstrated in 2006, but was shelved in favor of another shuttle-based human servicing mission. Nevertheless, robots are indispensable for efficient space operations and the presence of humans and robots are complimentary for most modern space missions [1]. For example, the Space Shuttle now uses its Remote Manipulator System (SRMS) as a camera boom for damage inspection after launch. Additionally, the crew of the International Space Station (ISS) routinely uses its Remote Manipulator System (SSRMS) in collaboration with SRMS for handing off and assembling newly delivered components from the Shuttle cargo bay.

Figure 1.1: Canadarm 2 (Canadian Space Agency)

The collaboration between humans and robots will be essential for future interplanetary endeavors. With constant advances in robotic technology and autonomy, robots are now undertaking voyages to the farthest expanses of outer space that are presently unreachable by human astronauts. Autonomous ground, aerial and submersible vehicles provide an invaluable means of exploring the planets. Although less glamorous, robots that carry out the more mundane tasks of satellite or space station assembly and repair should not be overlooked. They accomplish tasks in microgravity with less risk and cost than EVA alone.

Robots intended for space manipulation tasks must be carefully designed for precision and dexterity. Arguably the most critical factor in the design of a space

robot is its control architecture. It must be capable of stiff, accurate positioning, while at the same time remaining flexible enough so that servicing can be done with minimal loads imparted to the spacecraft. Large forces from contact can drive an otherwise stable controller into instability. Furthermore, they can push the target spacecraft away, unnecessarily excite modes of oscillation, and/or damage lightweight and sensitive space hardware [2]. Unfortunately for autonomous robots, these issues are complicated by the fact that the environment they interact with is largely uncharacterized. A space manipulator must be robust enough to perform accurately and delicately in a variety of unpredictable circumstances. Hence, one of the main objectives of space manipulator control is to ensure that the manipulator reacts stably to contact with an unknown environment, which is the principal goal of this research.

Control of robotic manipulators for general assembly and positioning is a field that has been studied extensively over the last five decades and some of the latest findings are presented and discussed in later sections. Manipulation in space is a subset of that research. Space manipulators have much in common with their terrestrial counterparts. In particular, unconstrained motion, stability during contact transition and force-controller manipulation of the environment are some of the issues discussed thoroughly in this thesis.

The Space Systems Laboratory (SSL) at the University of Maryland specializes in tele-operated manipulators for space applications and has a unique neutral buoyancy research facility (NBRF) for simulating conditions similar to microgravity. The Ranger manipulator was developed as the SSL research test bed

for robotic manipulation in neutral buoyancy, and for human-robot interaction in general.

1.1.2 Motivation: The Ranger Manipulator

Ranger is a spaceflight qualified dexterous robotic servicing system that was developed under funding from NASA as part of their Space Telerobotics Program. A free-flight version of Ranger was first designed in the 1993 as the Ranger Telerobotic Flight Experiment (RTFX). Its incarnation as the Ranger Neutral Buoyancy Vehicle (NBV) was made operational in 1995, intended for underwater use in a neutral buoyancy test facility such as the one at the University of Maryland. RTFX evolved into the fixed-base Ranger Telerobotic Shuttle Experiment (RTSX), developed for potential use on the Space Shuttle and International Space Station while attached to a Spacelab pallet. The system is able to perform dexterous manipulation, body repositioning and stereo video viewing. Ultimately the termination of the NASA Space Telerobotics Program eliminated the potential for Ranger to be flown in space, but nevertheless it endured as an important research tool for the SSL and NASA. From 2004-2005 its use as a platform for servicing of the Hubble Space Telescope (HST) was considered. Although NASA selected MDA's Dextre Special Purpose Dexterous Manipulator (SPDM) as the servicing robot, the Ranger Satellite Servicing System (RSSS) served as a valuable test robot for evaluating SPDM requirements and the feasibility of certain Hubble servicing tasks. Unfortunately NASA's tentativeness led to the cancellation of a robotic servicing mission, citing concerns that it would not be ready in time. Though terminated early, the program succeeded in demonstrating

Ranger's capabilities in the field, and its potential to carry out complex, delicate tasks. Notwithstanding, Ranger's control system was still lacking in tactility, and its response to obstacle impact remained an issue to be addressed. This thesis undertakes this task by looking at the control scheme currently used on Ranger.
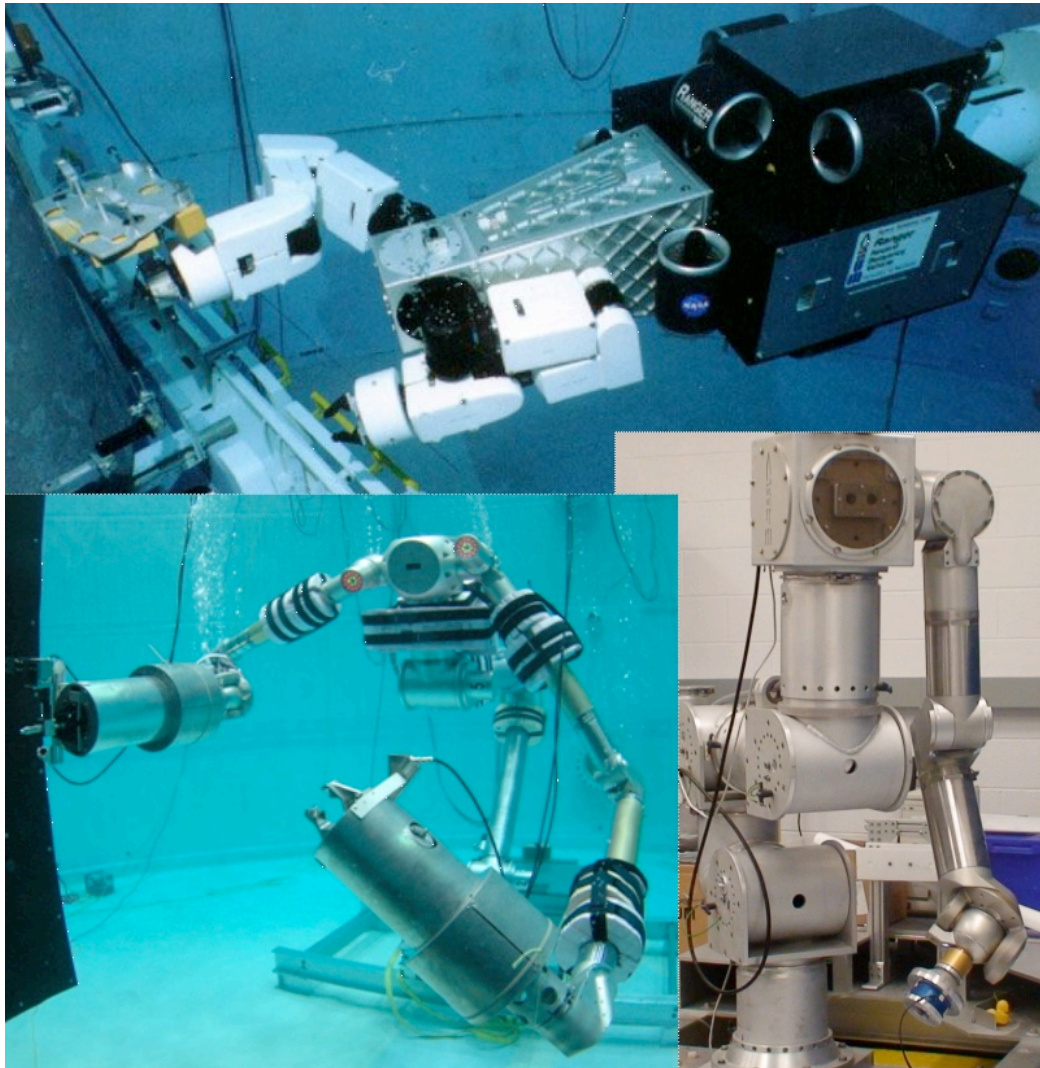
Figure 1.2: Ranger NBV (top), RSSS (left), RTSX (right)

1.2   Ranger Position Control Overview

1.2.2 Independent Joint Control

Like most other industrial manipulators, the basis of the Ranger control scheme is independent joint control (IJC). Each joint is individually controlled using a P-D controller with its own tuned proportional and derivative gains. This very simple control strategy is convenient and stable at low velocities for manipulators with unknown dynamics parameters (i.e. link mass and inertia, motor friction, etc.). At the most fundamental level, an operator can change the position of each joint independently by inputting a desired rotation angle. The operator can also separately select the speed of rotation. Once the position and velocity errors are determined, a high-gain P-D compensator ensures that the desired values are quickly tracked and that errors resulting from un-modeled dynamics as well as external disturbances due to dynamic coupling effects from neighboring joints are rejected.
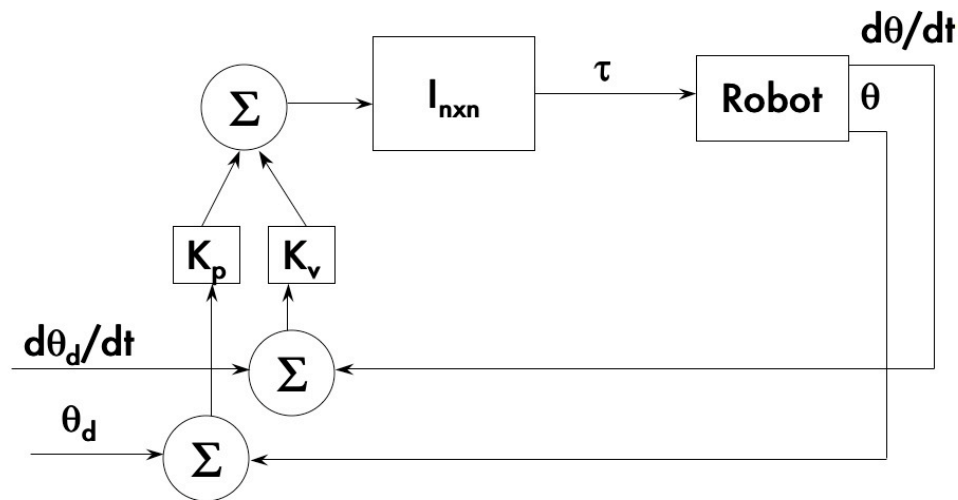
Figure 1.3: Independent Joint Control

6

1.2.3 Resolved Rate Control

The control scheme is different when position commands are given to the robot in Cartesian space. Such is the case when the hand controllers are used, and for certain trajectory-following scenarios. The hand controls effectively send a rate input (i.e. move forward/back/up/down at a given speed) proportional to the movement of the joystick(s). This rate is then multiplied by the sample period to obtain a position command. When the controller receives a command to a given position, it formulates a Cartesian error that is then distributed to each joint via the robot's inverse kinematics. The resulting joint error is then corrected using the IJC scheme discussed in the preceding section.
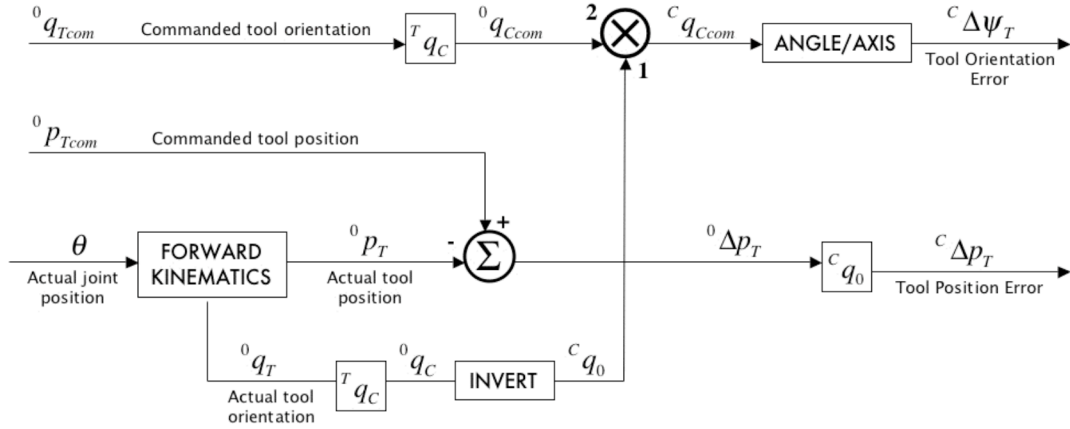
Figure 1.4: Cartesian Error Resolution for Resolved Rate Control

1.2.4 Limitations of Position Control

The high-gain position servo employed on Ranger produces commendable results in tracking commanded position and disturbance rejection. Positional accuracy is not the major concern with Ranger's control scheme. Ranger has demonstrated its ability

7

for positioning while performing mockup Hubble Space Telescope (HST) servicing tasks at NBRF in 2004. In addition to positioning its camera arm for optimal viewing, Ranger successfully accomplished insertion of several HST components in a simulated setting. While Ranger performs well at these end-effector positioning tasks, its performance is not optimal in contact situations. Generally Ranger's position controller is sufficiently well damped to remain stable in contact at low speeds, where the contact forces are treated as disturbances and rejected. Thus, operators must be careful to make contact very slowly and must manually halt forward progress if a surface appears to be impinged. This limits Ranger's capability to operate autonomously or to follow pre-planned trajectories in unknown environments. If contact with an obstacle is made and Ranger continues to be commanded forward, it will persistently force itself into the surface until its joint torques are saturated or, more catastrophically, until the obstacle is penetrated, deformed or crushed. Both of these scenarios are clearly unacceptable. The former can result in damage to Ranger's internals, while the latter can cause damage to the tool and manipulator in addition to the object that is impinged.

1.3   Mitigating Contact Issues:

1.3.2 Force and Compliance Control

The aforementioned problem is common for most position-controlled manipulators and methods for circumventing it have been developed quite extensively throughout the past twenty years. With the exception of the first method, an implicit

requirement for each of these is the ability to measure the contact forces at the some location on the manipulator (typically at the tool tip). Thus, the presence of a force/torque sensor or other method of determining/measuring forces and moments at this location is implied.

One manner of avoiding position control problems is to not use it, and instead control the force that is exerted on the environment. While force control may be more stable in contact, the ability to control position is lost. This compromise cannot be made on Ranger, whose tasks mainly involve positioning. Hybrid schemes have been proposed [3] although, as will be shown in Chapter 2, these are more suited toward structured assembly tasks where the directions of required position/force control are pre-defined.

To achieve the desired behavior and have the manipulator react to external forces that it encounters, it has been suggested to impose a relationship between the sensed forces and the manipulator's position or velocity. A useful implementation is compliance control or more specifically, impedance control, in which the force/position relationship imposed is that of a mass-spring damper system [4]. Thus, the manner in which the controller behaves depends on the selected values of the desired mass, stiffness and damping, or impedance, of the manipulator.

Pure impedance control does track position in a manner that is suitable enough for the needs of Ranger. The scheme used for Ranger is Position-Based Impedance Control which modifies the robot's desired trajectory according to the sensed force in order to achieve the specified impedance goal. This target impedance must be carefully selected so that the manipulator behaves the way that is intended. In

9

Ranger's case, this translates to maintaining a soft, stable contact with the surface.

1.3.3 Target Impedance Selection

It will be shown in Chapter 2 that to ensure stability of an impedance controller, matching the robot's impedance to that of the environment is paramount. Over the past 15 years there has been much research into how to best determine the appropriate gains to use for stable compliance. Offline strategies such as optimizations can be valuable for narrowing down a range of "initial guess" impedance parameters, which can then be fine-tuned [5]. One downside is that they require a dynamic manipulator model, which Ranger does not have (and even so, would be difficult to make accurate), in addition to knowledge of the environment as a basis on which to optimize the manipulator gains. In general, environment impedance is unknown and must be determined a priori, estimated, or adapted to. This will be discussed further in Chapter 2. Impedance gain bounds can also be found through the controller stability analysis, which will be presented in Chapter 4. It should be noted that stable impedance gains vary for the different phases of contact (free-space vs. sustained contact) and a controller that switches these gains based on detected forces is introduced in Chapter 2. It would be worthwhile to investigate the merits of such a scheme on Ranger.

1.4 Research Goals

Carignan and Smith previously conducted tests at the Space Systems Lab on suitable position-based impedance controllers for the Ranger dexterous manipulator

[6][7]. They investigated the effects of desired stiffness and damping, frequency, time delay, sample rates and bandwidth on the impedance error of the NASA Flight Telerobotic Servicer Demonstration Test Flight (DTF) and ADEPT controller for a shoulder joint. In addition, they determined controller stability boundaries for each of those parameters, but again only for one joint. They concluded that the ADEPT controller produced the lowest impedance error for all the listed factors and its utility should be evaluated on the full manipulator.

Carignan then implemented the ADEPT controller on the NBV arm, and demonstrated operation in a spring-dashpot, accommodation and mass simulation mode [8]. While the results were satisfactory, they also found that for stable operation in contact, damping gains had to be raised to 5-10 times their free-space values. This resulted in sluggish responses and could have been attributed to the compensator loop rates being limited by a communications bottleneck between the impedance and joint servo controllers. Since then, no further attempts were made at incorporating this controller on the current incarnation of Ranger (RTSX). The goal of this research is thus to integrate Carignan's original NBV controller into the existing framework and determine suitable gains for the stable execution of contact tasks. Improvements in processing as well as the use of corrective factors should lead to improved performance of this controller over its predecessor. Ranger's stability in contact tasks will be analyzed and the use of gain switching will be investigated. The stability analysis will be extended to the two-joint case for the two DOFs that provide the bulk of the impedance motion, namely the shoulder and elbow pitch. This analysis should provide stability bounds for the impedance gains. The culmination of these efforts

11

should be the inroads to a practical and reliable compliance controller for use with common manipulation tasks.
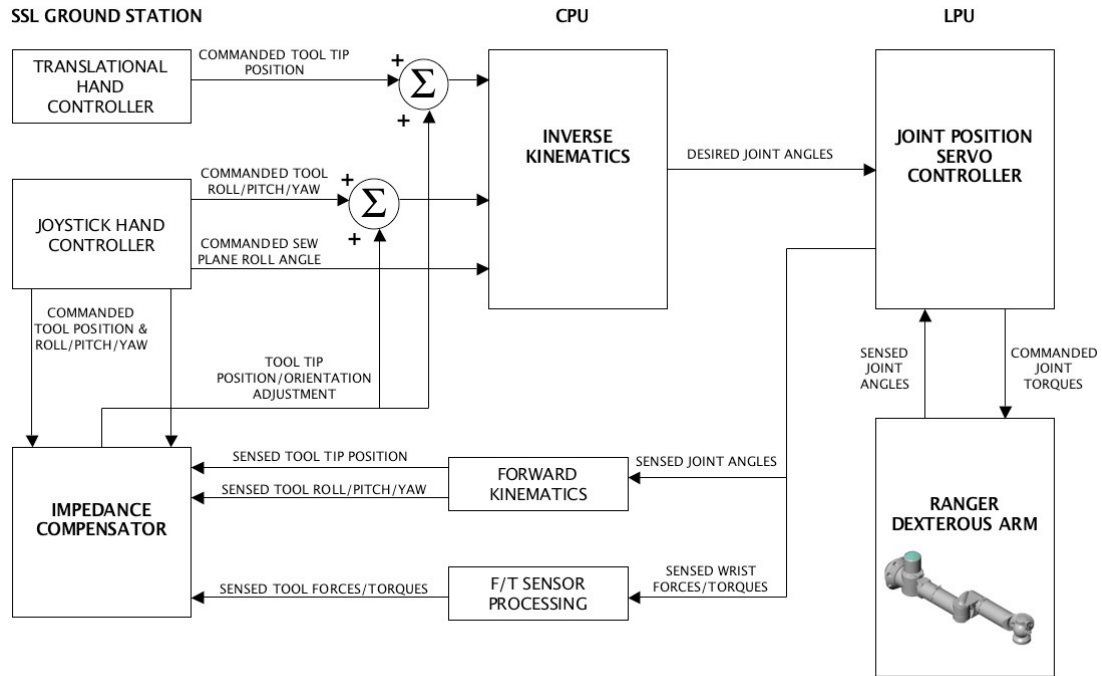
Figure 1.5: Overall Control Implementation

1.5   Outline of Thesis

Chapter 2 will expand on the theoretical background of compliance control and explain the position-based admittance controller used on Ranger. Methods for improving the controller will also be introduced. Chapter 3 will detail the experimental apparatus used as well as describe the actual experiments used for testing the controllers and the procedure for gain characterization. The gravity compensation algorithm used for the controller is also explained. Chapter 4 will describe the model of the manipulator as well as the control block diagram. These will then be used to examine the stability of the controller and establish stability

bounds on the admittance gains. The controller model is also used to develop a contact simulation, which is presented in Chapter 5 along with the findings of the actual contact experiments, a detailed analysis and comparison of the results. Finally Chapter 6 will summarize those findings, expose their limitations, and explain how the work can be advanced through future research.

Chapter 2

Theory

2.1 Compliance Controllers

The subject of compliance in manipulator control has been well studied over the last two decades. Numerous strategies and controllers have been proposed to address the issue [9], some of which are presented in this chapter.

2.1.1 Natural and Artificial Constraints

For the discussion to follow, it may be important to distinguish when position control alone would be appropriate and when force control would be necessary. This decision fundamentally depends on the *constraints* of the system [10]. Constraints can be set in terms of forces applied and velocities. In 3-space, if a robot is required or restricted to move in a certain direction, this is a velocity constraint that can occur in any translational or rotational direction, for a total of 6 velocity constraints. If a robot is required or limited to applying a given force (that force may also be zero if no force can be applied in that direction) then there is a force constraint along any translational or rotational axis, adding 6 more constraints for a total of 12 possible. In holonomic systems, such as the case with 6-DOF or greater manipulators, all 6 degrees of freedom are controllable and thus there should be 6 natural constraints. The remaining 6 constraints need to be imposed by the controller, and thus are termed *artificial* constraints.

An example here is helpful in illustrating their differences and implications in control.
Consider the following "classic" peg-in-hole insertion task:
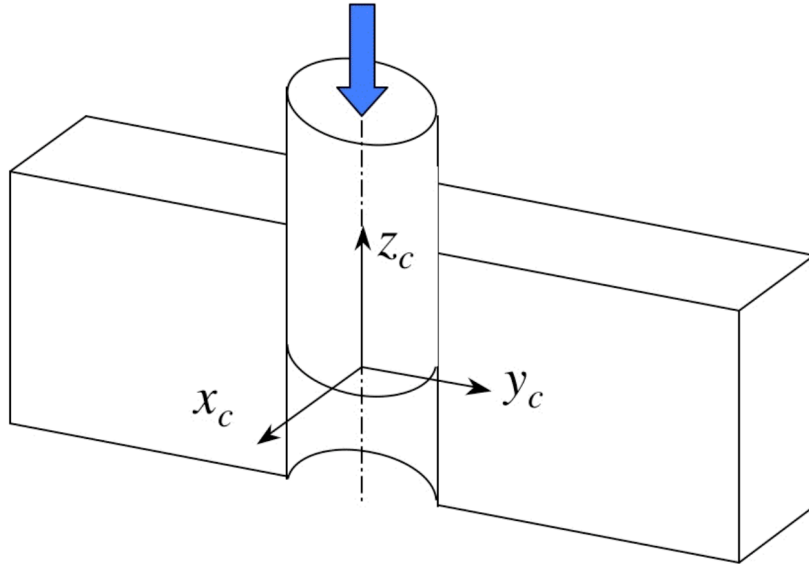
Figure 2.1: Peg-in-hole example for natural/artificial constraints

The coordinates of the compliance frame are denoted x_c, y_c, z_c, and happen to correspond with the task frame in this case. From this cutaway view it is visible that the peg is constrained to move in the z-direction only. The task involves positioning the peg along the z-axis. The peg cannot move in the x-y plane because of the presence of a rigid surface there. In addition, the peg cannot rotate around the x and y-axes due to the surrounding environment, nor can the constraining environment impose a force or moment in the z-direction. All these constraints due to implicit geometry are thus *natural* constraints. Forces could be applied in the x and y-directions, but it's best for assembly if those forces are zero. Similarly, there should be zero moments in these directions as well. If assembly required spinning of the part, a non-zero rotational velocity could be assigned in the z-direction, but for simplicity it

is deemed unnecessary. The only real requirement for assembly is that the peg moves in z with a pre-determined velocity, v_d.

Essentially all constraints that could be modified by the controller are artificial. Natural constraints, on the other hand, are invariable. A summary of the constraints for this example can thus be given as:

Natural Constraints	Artificial Constraints
$v_x = 0$	$v_z = v_d$
$v_y = 0$	$\omega_z = 0$
$\omega_x = 0$	$f_x = 0$
$\omega_y = 0$	$f_y = 0$
$f_z = 0$	$n_x = 0$
$n_z = 0$	$n_y = 0$

Table 2.1: Natural/artificial constraints for peg-in-hole example

The artificial constraints can be interpreted as a requirements list for the controller. In this case, the velocity in z is specified, so an appropriate position controller is necessary in this direction. Conversely, there is a condition that zero force be applied in the x and y-directions, which implies the use of force control in these directions. In Hybrid Control (discussed later), these orthogonal requirements become very relevant.

2.1.2 Salisbury Stiffness Control/Implicit Force Control

This was a sensor-less approach to compliant control first devised by Salisbury in 1980 [11]. Essentially the controller is designed such that the robot's joints behave like springs.

$$K_p\left[J^{-1}\left(\underline{x}_D - \underline{x}\right)\right] - J^T \underline{F}_{env} = \underline{\tau} \tag{2.1}$$

The controller converts a Cartesian position error into joint space via the inverse

Jacobian and then multiplies by a stiffness gain, as illustrated in Figure 2.2. This proportional controller compensates for the disturbance error introduced by the environmental contact force.
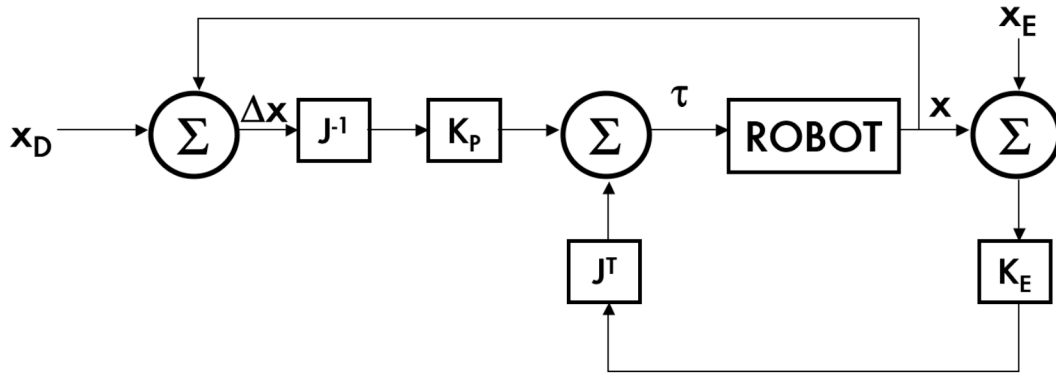
Figure 2.2 Salisbury Stiffness Control (modified from [12])

Where K_p is a matrix of stiffness values corresponding to each joint and K_E is the environmental stiffness.

2.1.3 Force Control (Explicit)

Developed by D.E Whitney in the late 1970s/early 1980s, explicit force control (Figure 2.3) essentially uses the same principle as position control, except force is tracked in lieu of a desired position. Thus, the operator commands a given force to be applied consistently throughout the manipulator's motion, without regard to position necessarily.

While conceptually practical for stable application of force to a surface, this control scheme is useless for precisely controlling the position of a tool tip in free space. Unless motion is completely constrained, there will always be a direction in

which no force needs to be applied and only positional control is necessary. Futhermore, An and Hollerbach [13] demonstrated that force control was unstable in contact with a rigid surface, Whitney [12] observed instability caused by digital sampling and other researchers, such as Raibert and Craig [3], observed the destabilizing effects of unmodeled nonlinearities such as friction, backlash and cogging in geared manipulators.
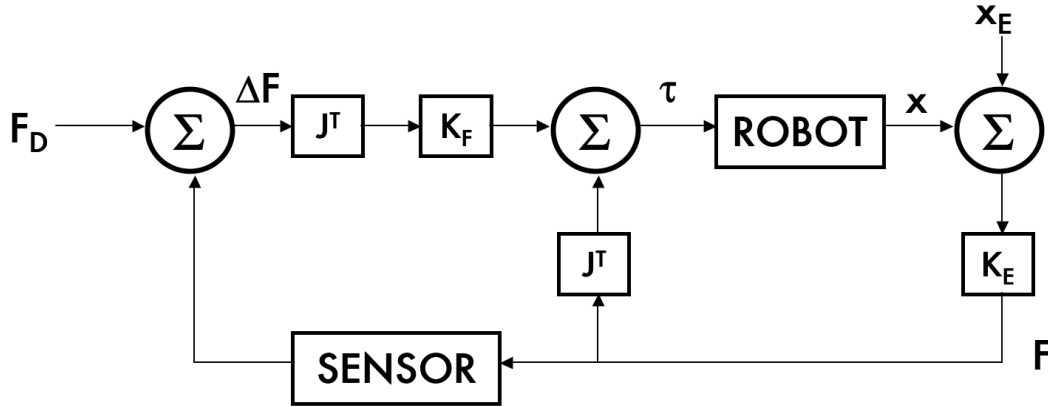
Figure 2.3: Explicit Force Control

2.1.4 Hybrid Position/Force Control

To render force control more useful, Raibert and Craig developed a hybrid controller that couples force control with position control. The controller is organized according to the artificial constraints of the system, such that some DOFs are force-controlled and the remaining ones are position-controlled. The two categories are distinguished using a task-dependant selection matrix, S, which is a diagonal matrix of ones and zeros, used as depicted in Figure 2.4.

Figure 2.4: Hybrid Position/Force Control (modified from [12])

While this method is an improvement over explicit force control, it relies on a presupposition of the robot's path of motion. This method may be perfectly acceptable for a structured, repetitive assembly task. However, for a general-purpose manipulator that can encounter constraints in any direction at any time, it is not nearly versatile enough. Autonomous mode switching could improve performance with unknown environments, although this could be difficult to implement and delays in switching could introduce instabilities. Using a more robust position controller in conjunction with a more compliant controller (explained below) instead of the explicit force controller could also enhance performance.

2.1.5 Stiffness Control

The major pitfall of the previous scheme is that switching between strict position and force control can be problematic from a stability standpoint. One

solution is to control the relationship between force and position. The simplest such

relationship is Hooke's law:

$$F = kx \qquad\qquad (2.2)$$

$$K_p\left[J^{-1}\left(\underline{x}_D - \underline{x} - K_{F1}\underline{F}_{env}\right)\right] - J^T\underline{F}_{env} = \underline{\tau} \qquad\qquad (2.3)$$

Essentially this allows the manipulator endpoint to behave like a mass-spring

system. Unlike Salisbury stiffness control, which makes no force measurements, this

method uses force/torque readings as means of modifying the desired trajectory such

that the arm's overall stiffness is corrected. Thus, it could be said that stiffness control

is equivalent to a proportional-gain force-feedback loop, as shown in Figure 2.5. This

controller does nothing to control (dampen) high velocities that may arise from a high

choice of stiffness.
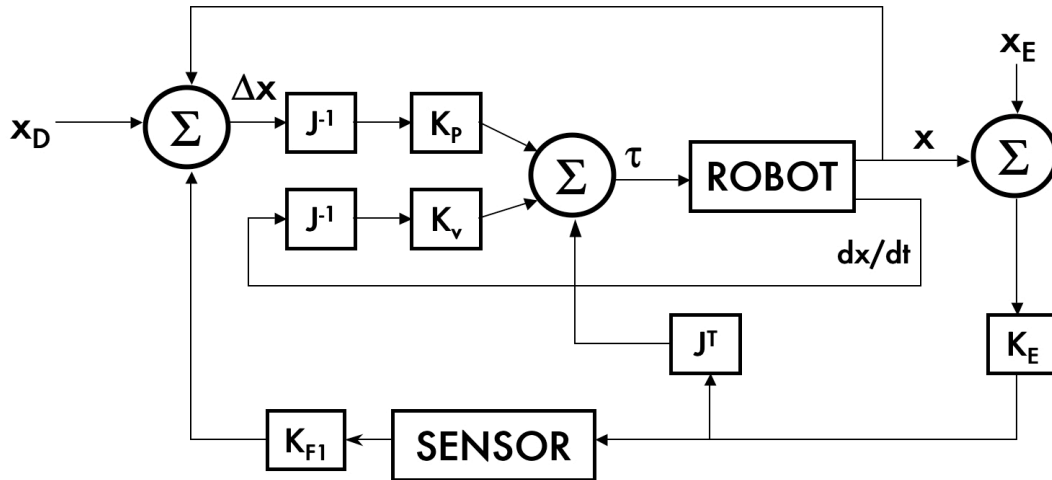
Figure 2.5 Stiffness Control (modified from [12])

2.1.6 Damping Control

Damping control is identical in concept and implementation to stiffness control, except that velocity is tracked instead of position and the resulting gain on the force feedback has the units of velocity/force (i.e. admittance). Hence, instead of enforcing Hooke's law between input and output, the following admittance relationship is used:

$$F = b\dot{x} \tag{2.4}$$

$$K_p\left[J^{-1}\left(\dot{\underline{x}}_D - \dot{\underline{x}} - B_{F1}\underline{F}_{env}\right)\right] - J^T\underline{F}_{env} = \underline{\tau} \tag{2.5}$$

Alternatively, this can be thought of as a derivative force-feedback loop, as shown in Figure 2.6. The drawback to pure damping control is the inability of the manipulator to return to its desired position.
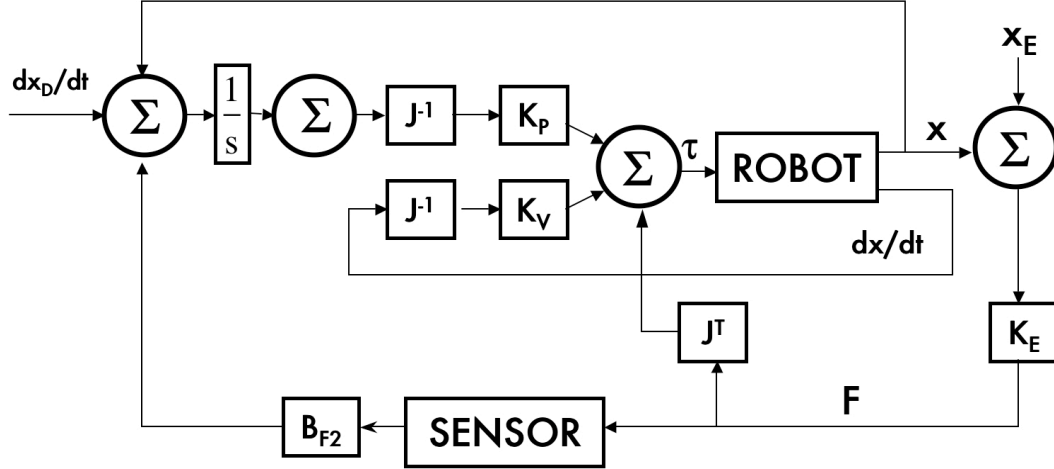
Figure 2.6: Damping Control (modified from [11])

21

2.1.7 Impedance/Admittance Control

Expanding on Salisbury's idea of controlling the force/position relationship, in 1985 Hogan proposed using mechanical impedance as a reference model [4]. The result was a combination of the Stiffness and Damping controllers described previously. Impedance control as illustrated below could also be described as a PD force feedback loop.
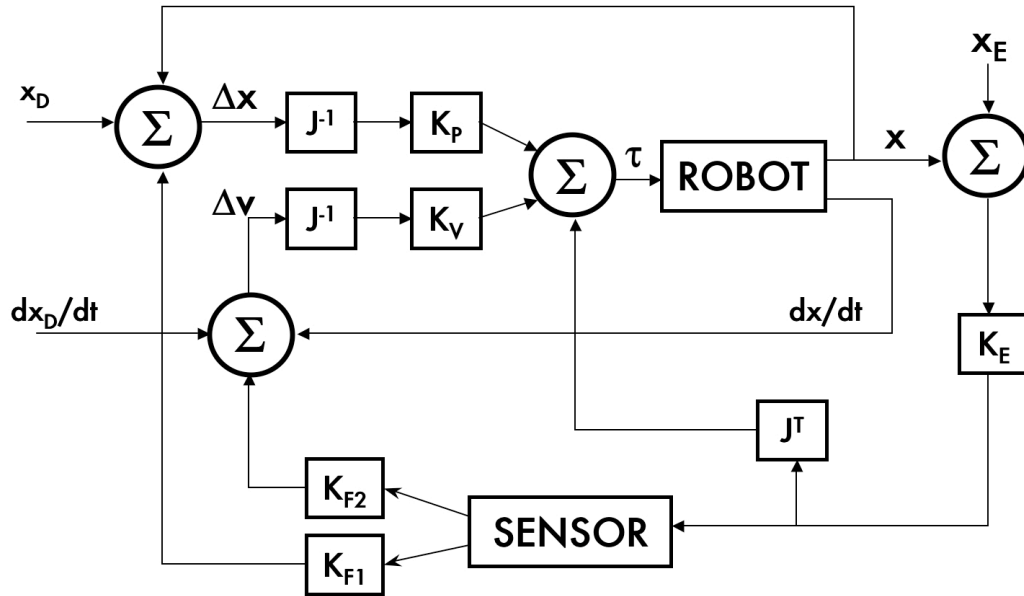
Figure 2.7: Impedance Control (modified from [11])

The combination of systems can be more simply regarded as a relationship between effort and flow. The impedance, Z, relates the force, F, and velocity, V, via:

$$F(s) = Z(s)V(s) \qquad (2.6)$$

An inverse relationship can also be defined as:

$$V(s) = Z^{-1}(s)F(s) \qquad (2.7)$$

The term Z^1 is termed the *admittance* of the system, and as the equation suggests, is simply the inverse impedance.

The impedance can be any kind of function, although for control implementation where environmental contact is made, it is most common to impose a mass-spring-dashpot relationship such that the environment force solicits a position response of the form:

$$M\underline{\ddot{x}} + B\underline{\dot{x}} + K\underline{x} = \underline{F} \qquad (2.8)$$

Converting to the Laplace domain:

$$Z(s) = \frac{F(s)}{V(s)} = Ms + B + \frac{K}{s} \qquad (2.9)$$

To ensure good control performance during interaction with the environment, it is essential that the target impedance be chosen appropriately. In order to help determine which type of impedance operator is better suited for a given environment, Spong classified these impedances based on their behavior at low frequencies [14]. The system's DC gain is given by:

$$k_{DC} = \lim_{s \to 0} Z(s) = Z(0) \qquad (2.10)$$

By definition, an impedance is:

a) *Inertial*, if and only if $|Z(0)| = 0$

b) *Resistive*, if and only if $|Z(0)| = B$, for some constant $0 < B < \infty$, and

c) *Capacitive*, if and only if $|Z(0)| = \infty$

We can draw the mechanical analogies for these classifications. An inertial system transfers all force into motion and thus can be modeled as a mass moving

23

along a frictionless surface. Similarly, a capacitive system stores energy and is analogous to a spring; whereas a resistive system dissipates energy with loses, which is indicative of viscous damping.

Environment types. (a) Inertial. (b) Resistive. (c) Capacitive.
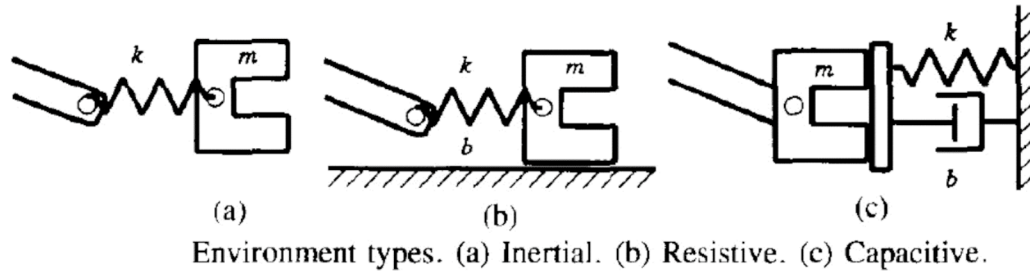
Figure 2.8: Environmental impedance types (from [14])

Spong also determined an important condition when modeling systems as impedances. For optimal behavior during interaction, it is ideal if the manipulator is the *dual* of the environment. This duality principle states:

1. Capacitive environments are to be force-controlled with non-capacitive manipulator impedances.

2. Inertial environments are to be position-controlled with non-inertial manipulator impedances.

3. Resistive environments are to be force-controlled with inertial manipulator impedances *or* position-controlled with capacitive manipulator impedances.

Thus, if the manipulator makes contact with a highly capacitive environment (a rigid wall, for example) the manipulation should ideally be force-controlled with inertial and/or resistive impedance. Conversely, a manipulator moving in free space (highly inertial) should be position-controlled with capacitive and/or resistive impedance.

24

The impedance compensator replaces the position controller, and the position is modified in order to achieve the target impedance. The equation of the impedance compensator is:

$$M\left(\ddot{\underline{x}}\right) + B\left(\dot{\underline{x}} - \dot{\underline{x}}_0\right) + K\left(\underline{x} - \underline{x}_0\right) = \underline{F} \tag{2.11}$$

The nominal trajectory, $\underline{x}_0$ is thus altered, and the required joint accelerations, a, are then calculated from the inverse dynamics of $\ddot{\underline{x}}$ and fed to a computed-torque-like controller of the form:

$$\tau = M\left(\underline{q}\right)\left(\ddot{\underline{q}}_d - a\right) + N \tag{2.12}$$

Where M is an inertia matrix and N is the nonlinear model compensation. One drawback of this setup is that it only modifies commanded joint torques. Since it does nothing more to track position, it is prone to steady-state position errors. Of course there are many other sources of error that make the force control problem more complicated and difficult. Actuator/sensor non-collocation is a stability problem arising when a control loop is closed using a sensor and actuator placed at different points on a manipulator, which is commonly the case. On Ranger, the force sensor is placed at the tool tip, while position control is done at the joint level. This is currently an unavoidable problem that the controller must attempt to minimize.

2.1.8 Position-Based Impedance Control

Within impedance/admittance control there are many variations with subtle differences that could be discussed at great length [15][16]. Among them, there have been attempts to improve the poor position tracking of the above controller as well as

addressing the non-collocation problem. One solution, proposed by Maples and Becker [17] was to wrap a compliance controller around an existing position controller, shown below.
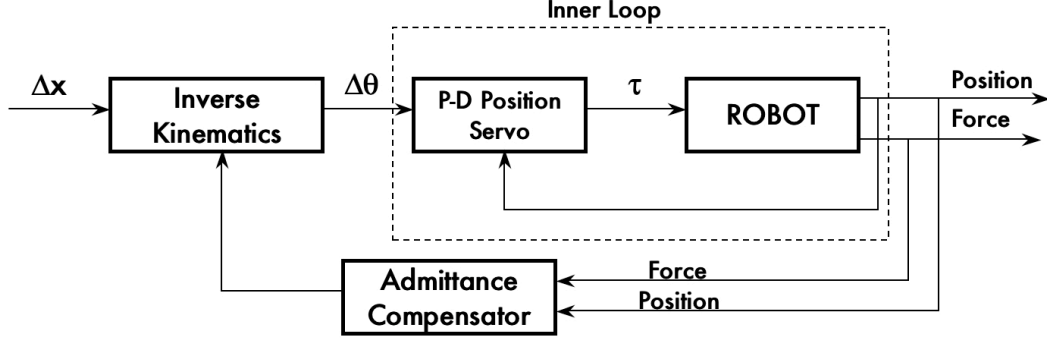
Figure 2.9: Force servo with inner position loop

It was only 2 years later that Lawrence more formally defined this type of position-based controller [18]. Using both commanded position and force readings, and the compensator then modifies the desired position to match an impedance goal.

$$M\,\underline{\ddot{x}}_{des} + B\left(\underline{\dot{x}}_{des} - \underline{\dot{x}}_{com}\right) + K\left(\underline{x}_{des} - \underline{x}_{com}\right) = \underline{F}_{ext} \tag{2.13}$$

The modified desired position x_{des} is then fed to the previously existing position controller, which ensures decent position tracking of the modified signal.

One advantage of this arrangement is that is doesn't require modifications to the existing controller, the impedance compensator is simply added on.

A favorable side effect is made visible by rearranging this admittance model in the Laplace domain. Force is transformed into position via

$$\frac{X_{des}(s)}{F_{ext}(s)} = \frac{1}{Ms^2 + Bs + K} \tag{2.14}$$

26

This can be seen as a second-order low-pass filter on force and is a helpful property since the force signals from sensors are typically ridden with high-frequency noise [19].

Of course there are many other sources of error that need to be addressed when choosing a proper compensator for a manipulator, including, but not limited to: filtering, work piece dynamics, environment stiffness, actuator bandwidth, sensor dynamics, arm flexibility, impact forces, and the always-present drive-train backlash and friction. This is precisely why controller robustness is essential achieving optimal performance. The impedance controller selected for Ranger addresses some of these issues, but is not without problems, as is shown in subsequent chapters.

2.1.9 Natural Admittance Control

As an alternative to position-based impedance control, Wyatt Newman developed Natural Admittance Control (NAC) as a force control strategy [20][21][22]. NAC is based on the concept of passivity from nonlinear control theory: A passive system is stable as well as two interconnected passive systems. A robot in contact with the environment is an interconnected system. Typically, the environment is passive, thus if a robot can be controlled to behave passively, the combined system will behave in a stable fashion. Making a robot behave passively is no easy task. A prime requirement is a high-fidelity model of the robot dynamics because essentially, they must be nullified.

In addition, the robot's passive response to force and position input need to be identified. This is done by exciting each joint of the robot and characterizing its

27

response in position (velocity) and force. Their ratio $V/F = Z^{-1}$ is then used to define an admittance for each joint. These admittances are then used in the calculation of the overall admittance of the robot that is required to make the system passive and thus ensure stability. A benefit of this method is good friction rejection because the passive motor response is calculated from the response with friction.

The method was used for existing industrial manipulators with promising results [23]. However, they also demonstrated that there was only a limited range of manipulator impedances that could be achieved passively and this was due to the implicit design of the manipulator. For example, the manipulator's link inertia was a limiting factor, which cannot be altered without a physical re-design of the manipulator. They also investigated the use of passively compliant end-effectors and sensors, which achieved stability goals, but at the expense of positional accuracy.

While results are good, this method requires a complete overhaul of the manipulator and its controller in order to determine the joint impedances. Nevertheless, if other methods of impedance/admittance control do not result in favorable performance, and controller re-design is necessary, NAC might be a tempting option.

2.2 Compliance Control on Ranger

An admittance controller with position feedback [24] is well suited for Ranger because the implicit assumptions of high-gain position control and high gear ratios at the actuators are met [18]. In the current controller design, the admittance loop is wrapped around Ranger's pre-existing high-gain position servo. This conveniently

eliminates the need for a complete re-design of the entire controller. The manipulator responds to environmental contact at the tool tip, adapting its impact force with the surface by modifying its desired position in order to match an operator-specified admittance goal.

The controller used on Ranger is based on the one introduced in [17], seen in Figure 2.10.
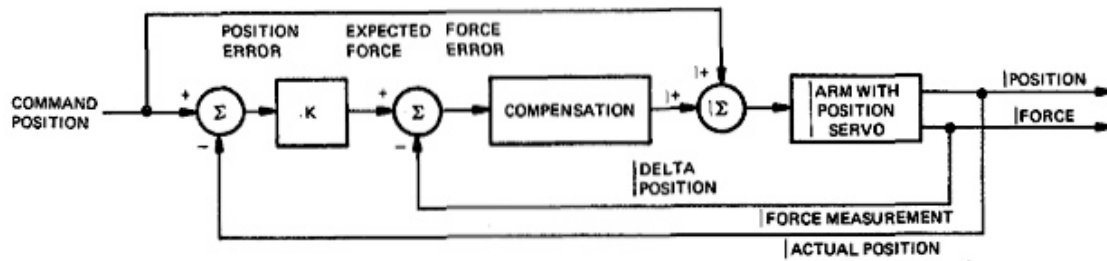
Figure 2.10: Compliance Control with inner position loop (from [17])

The implemented version of the admittance compensation is shown in figure 2.11. Position, *p*, and orientation, *q*, commands that are normally sent to the position controller are instead first modified by the admittance loop. The actual tool position and orientation is subtracted to create a position error in the base frame (denoted as *'0'* in the figure. This error is then converted to the sensor, or compliance frame (denoted *'C'* below), via a coordinate transformation. The compliance frame is situated at the base of the force/torque sensor (shown later) and for simplicity will have the same orientation as the tool frame. The position error is then multiplied by the desired stiffness, **K**, of the manipulator, producing a force/torque error term ($\Delta f/\Delta \tau$). The measured force is also added to this error. The force error signal is then passed through the admittance compensator, **C(s)**, which is composed of the desired

inertial and damping terms. This admittance converts the signal back to a position/orientation error, which is then transformed back to the base frame, as the *adjusted* tool position. This adjustment is then added to the commanded position to form the desired tool position. It is then converted to joint space via inverse kinematics and sent to the position control loop.
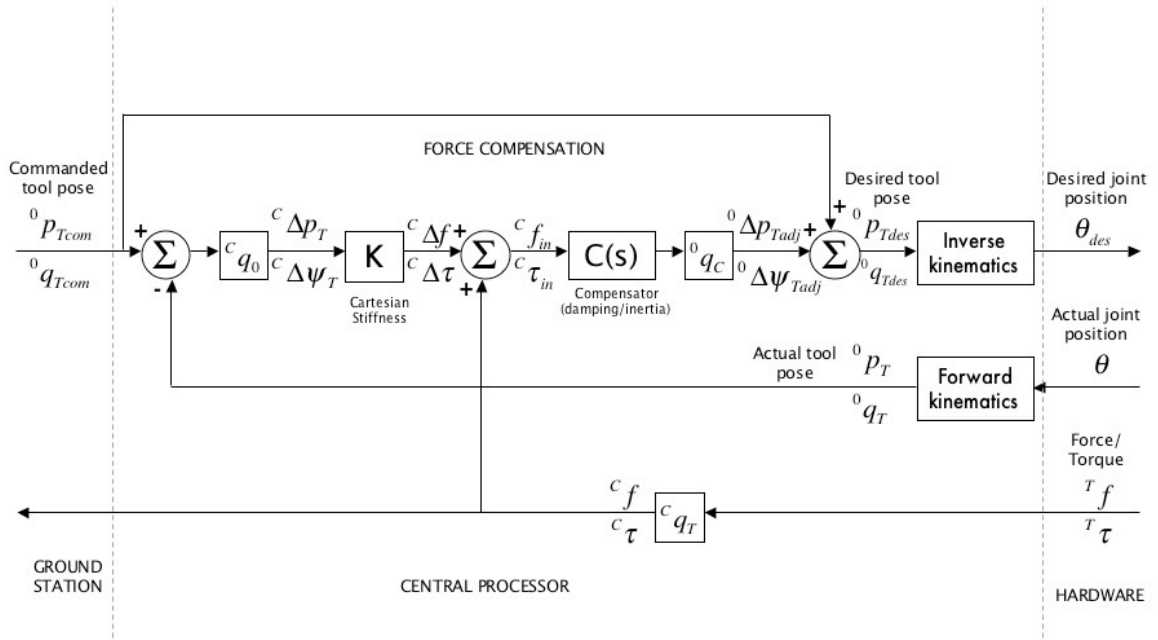
Figure 2.11: Block Diagram of Ranger Admittance Controller

Smith and Carignan (1994) showed that for a high inner loop bandwidth, the controller's impedance can be approximated as:

$$Z(s) \approx \frac{C^{-1}(s)}{s} + \frac{K}{s} \qquad (2.15)$$

The desired impedance is given by:

$$Z_d(s) = M_d s + B_d + \frac{K_d}{s} \qquad (2.16)$$

By equating equations 2.15 and 2.16:

$$K = K_d \qquad (2.17)$$

$$C(s) = \frac{1}{M_d s + B_d} \frac{1}{s} \qquad (2.18)$$

Since Ranger uses resolved rates as inputs, the $\frac{1}{s}$ integrator term disappears,

and the admittance compensator is simply:

$$C(s) = \frac{1}{M_d s + B_d} \qquad (2.19)$$

Equation 2.19 is effectively termed the *second-order*, or *inertial* compensator,

and is one of Ranger's impedance "modes". It is useful for manual positioning of the

manipulator endpoint, or if the damping term is removed, to simulate a free-floating

mass. The discrete equivalent of (2.19) was found to be:

$$C(z) = \frac{1}{b_d} \frac{1 - e^{-aT}}{z - e^{-aT}} \qquad (2.20)$$

$$a = \frac{b_d}{m_d} \qquad (2.21)$$

Where 'T' is the sample period (in seconds).

In a case like the free-floating mass simulator where pure inertia is desired

(i.e. $b_d = 0$) the $1/b_d$ term of (2.20) is problematic. In order to remedy this, (2.20) is

expanded in a Taylor series and only order T terms are kept, resulting in:

$$C(z) = \frac{1}{m_d} \frac{1}{z - e^{-aT}} \qquad (2.22)$$

The difference equation employed in the controller code is thus:

$$ {}^C f_{out}[i+1] = e^{-aT} \, {}^C f_{out}[i] + \frac{T}{m_d} \, {}^C f_{in}[i] \tag{2.23} $$

For positioning applications, the inertial term may be undesirable as it makes the manipulator more difficult to stop, resulting in position errors. For such a case, the inertial term is removed and the result is a *first-order* or *spring-dashpot* compensator:

$$ C(s) = \frac{1}{B_d} \tag{2.24} $$

The digital equivalent used in the controller algorithm is simply:

$$ C(z) = \frac{1}{B_d} \tag{2.25} $$

The outputted adjustments from the compensator are then transformed back into the base frame:

$$ \begin{aligned} {}^0 \Delta \dot{p}_{Tadj} &= {}^0 q_C \, {}^C f_{out} \\ {}^0 \Delta \dot{\psi}_{Tadj} &= {}^0 q_C \, {}^C \tau_{out} \end{aligned} \tag{2.26} $$

These velocity adjustments are then multiplied by the sample period and added to the integrated hand controlled commanded input

$$ \begin{aligned} {}^0 p_{Tdes} &= {}^0 p_{Tcom} + {}^0 \Delta \dot{p}_{Tadj} T \\ {}^0 \psi_{Tdes} &= {}^0 \psi_{Tcom} + {}^0 \Delta \dot{\psi}_{Tadj} T \end{aligned} \tag{2.27} $$

The new desired position and orientation are then finally sent to the position controller.

Within the same framework, it is also possible to introduce a remote center of compliance that is not located at the base of the compliance frame, as in Figure 2.12. It can be specified anywhere relative to the tool frame and used to change the

magnitude and direction of the compliance.
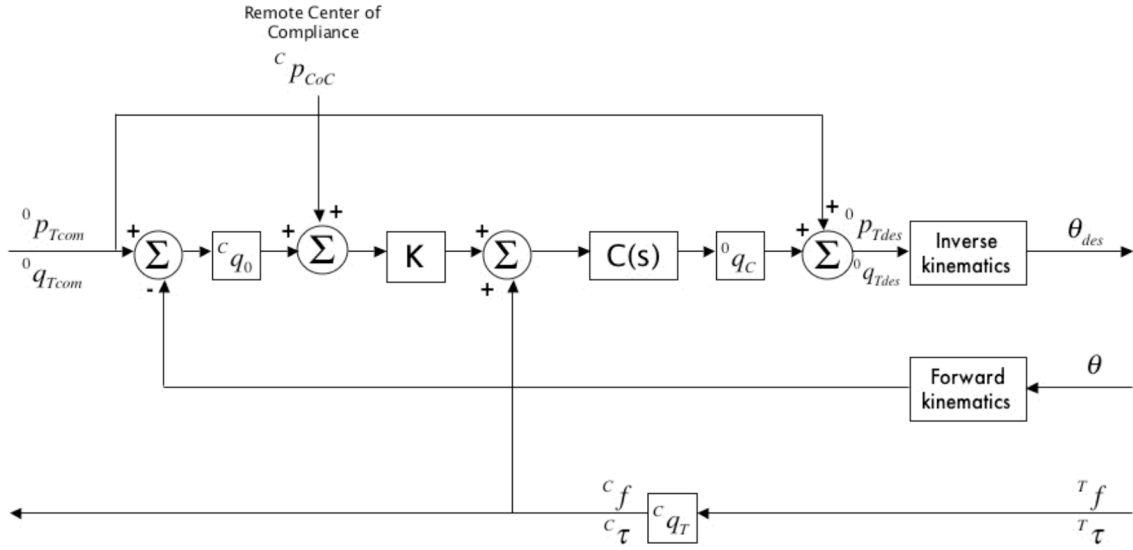
Figure 2.12: Controller with remote center of compliance

Corrective factors introduced by Pelletier and Doyon [15] may be used to improve the performance of the controller. The corrective factor compensates for the lack of feedback for a particular term and its implementation is shown in Figure 2.13. In Ranger's case the missing term is the velocity (acceleration feedback is not used on Ranger) and the corrective factor is c_v, which ranges from 0 to 1. The difference between desired and actual velocity is multiplied by c_v and added to the desired velocity. This reduces the error in not using velocity feedback for the calculation of the force error by a factor of $(1 - c_v)$. Theoretically, a corrective factor of 1 would eliminate the error. However, this introduces an infinite gain, which would corrupt a digital implementation of this controller. The general equation in Laplace domain for the first order admittance controller with the corrective factor is:

$$X_{adj} = \left(F_e + k_d X \right) \frac{1}{b_d s} + c_v \left(X_{adj} - X \right) \tag{2.28}$$

33

Re-arranging:

$$X_{adj} = \frac{(F_e + k_d X)}{b_d s} + c_v X_{adj} - c_v X \qquad (2.29)$$

$$X_{adj} - c_v X_{adj} = \frac{(F_e + k_d X)}{s b_d} - c_v X \qquad (2.30)$$

$$X_{adj}(1 - c_v) = \frac{F_e + k_d X - b_d c_v X s}{s b_d} \qquad (2.31)$$

Assuming the environment can be represented by a spring,

$$f_e = k_e x \qquad (2.32)$$

$$X_{adj} = \frac{X(k_e + k_d - b_d c_v s)}{s b_d (1 - c_v)} \qquad (2.33)$$

Thus, we see that the corrective factor of 1 can lead to an infinite gain situation.

$$\frac{X_{adj}}{X} = \frac{k_{eq} - b_d c_v s}{s b_d (1 - c_v)} \qquad (2.34)$$

Where:

$$k_{eq} = k_d + k_e \qquad (2.35)$$

In their research, Pelletier and Doyon opt for a corrective factor of 0.75. However, even for a lower corrective factor, the increased gain could drive the system to instability. The effect on stability will be investigated in Chapter 4.
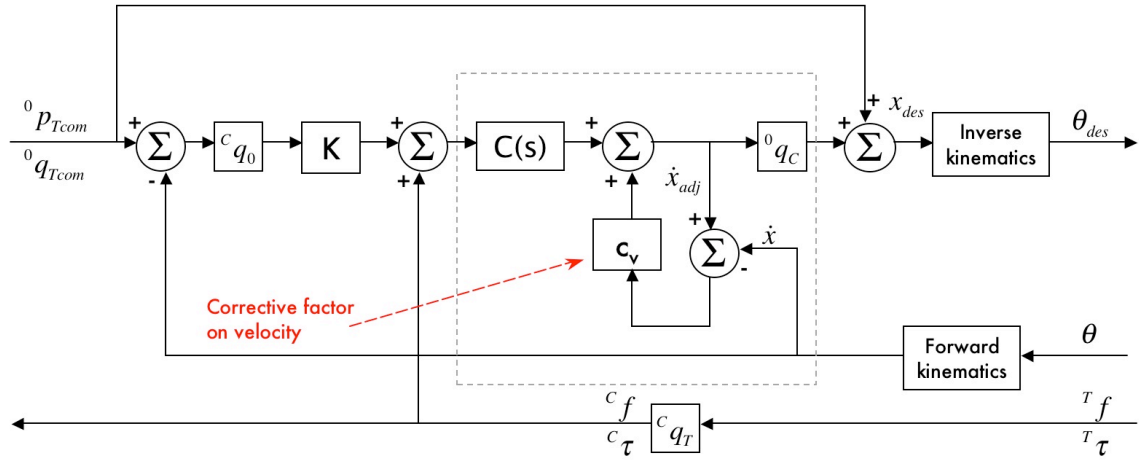
Figure 2.13 Controller with corrective factor

2.3 Impedance Selection

It was mentioned in Section 2.1.7 that for stable impedance control in contact, the choice of robot impedance parameters is vital. Furthermore, the impedance gain selection depends on the environment it comes into contact with. Love and Book were the first to successfully demonstrate that contact stability is improved if estimates of the environment impedance are known [25]. The estimation algorithm they devised attempts to fit the measured force, F, and penetration depth, x, to the relation:

$$F = M\ddot{x} + B\dot{x} + Kx \qquad (2.36)$$

A recursive least squares (RLS) regression is then used to determine the mass, stiffness and damping terms online. From these experiments, they also determined that it was essential to factor in the environment stiffness for finding suitable target impedance. "Suitable" natural frequency and damping gains were found to be: (for a critically damped system)

35

$$\omega_n = \sqrt{\frac{K_t + K_e}{M_t}} \qquad (2.37)$$

$$B_t = 2\zeta\omega_n = 2\zeta\sqrt{\frac{K_t + K_e}{M_t}} \qquad (2.38)$$

Melchiorri reinforced these findings by using other models that included coefficient of restitution and energy methods [26].

By conducting a robust stability analysis, Surdilovic [27] determined a lower bound for the damping ratio of a Position-Based Impedance Controller:

$$\zeta_t \geq 0.5\left(\sqrt{1 + 2\kappa} - 1\right) \qquad (2.39)$$

Where κ is the ratio of environment stiffness to target stiffness.

$$\kappa = \frac{K_e}{K_t} \qquad (2.40)$$

It is important to note that these methods only provide a good starting point for gain estimation. Since a number of factors may influence performance, narrowing down the best gains involves tradeoffs.

2.3.1 Impedance Error

Once the desired impedances are known, the next question is whether the controller accurately delivers the desired impedance values. Smith characterized the impedance error in magnitude and phase and determined the effect of several factors on the error, plotting the percent error versus frequency [7].

The impedance error was defined as the following, where Z_{des} is the desired impedance:

$$Z_e = \frac{|Z_{des} - Z_a|}{|Z_{des}|}$$ (2.41)

$$Z_{des} = K_{des} + B_{des}s$$ (2.42)

$$Z_a = K + C^{-1}$$ (2.43)

Desired stiffness, inner loop bandwidth, sample rates of the inner and outer loops, computational delays, and force feed-forward compensation were the factors Smith considered. In general, increasing the desired stiffness and damping had the effect of increasing the impedance error while increasing bandwidth and sample rate reduced the impedance error. Force feed-forward was also shown to minimize the error. While results varied for each factor, the trend that appeared throughout was that the impedance error increased with frequency, which is typical of a controller that is designed to work at steady state.

2.3.2 Stability Analysis

While determining gains that result in good performance is important, ensuring that these gains provide stable contact is essential. Lawrence analyzed stability for the DTF position-based impedance controller [18]. He noted that while admittance controllers are generally unable to provide very low impedances (high gains), they are still desirable when stiff joint position is required, as in Ranger's case. He went on to analyze the effects of computational delays, discrete implementation and manipulator dynamics on the system's performance. Stability boundaries were plotted for in terms of desired stiffness and damping for various manipulator bandwidths. As an extension of this work, Smith defined stability bounds

for the ADEPT controller (used on Ranger) for a single joint [7]. Time delays and the effect of increased bandwidth and increasing environment stiffness were considered. It was determined that force feed-forward, while beneficial to impedance error, requires higher damping for stability. Furthermore, for higher environment stiffness, higher damping is required for stability and likewise for increased time delay. Additionally, it was determined that increasing controller bandwidth reduced the stable region. Since her analysis was only performed for a single joint, the effect of arm configuration, inertia, on stability was not considered. In Chapter 4, the analysis is extended to the two-joint case. The regions of stability will be useful for limiting the gain selection.

2.3.3 Impedance Switching and Impact Control

There are three main phases to tool contact with the environment: Approach, impact and sustained contact. Each of these phases has drastically different dynamic requirements. Having identical impedances for all three is inadequate, but nonetheless characteristic of most impedance controllers. Tradeoffs are thus made at each phase, possibly sacrificing positional accuracy for robust stability. A controller that continuously alters the robot's impedance to meet these different needs would be ideal. However implementing an adaptive strategy based on position error and robot force telemetry, as proposed by Seraji and Colbaugh [28], would involve controller redesign. Guion [29] implemented an adaptive controller that compensated for frictional effects on a 2-link manipulator at the Space Systems Lab. While this manipulator used Ranger's joints, the controller was designed independently to

incorporate adaptive control. A simpler, albeit less robust, approach is to break up the impact into distinct phases and determine suitable gains for each one. A state machine would then select the gains appropriate for the phase. This approach uses the existing impedance control framework, only retrofitting a switch statement.

A sensible way to differentiate phases is through the measured impact force, as proposed by Gershon and Baruch [30] in their gain-switching methodology. If the measured force were zero (or very small) then the robot would be in a "free space" or "approach" mode. If the measured force were suddenly nonzero, or if the robot had knowledge of an imminent impact, it would switch to an "impact" or "transition" mode. Finally, if the contact force were sustained (for more than three sampling periods in the literature), it would convert to "contact" mode. Selecting only one set of gains for all three modes compromises the performance of the other two. For example, high damping makes for sluggish performance in free space, whereas large stiffness can be disastrous in rigid contact.

Research [31] has shown that for free-space motion, high stiffness, low damping and practically zero inertia are recommended. In the transition mode, damping and inertia need be set just high enough to ensure no loss of contact (i.e. to not bounce). For contact with a rigid environment, low stiffness and high damping are required to minimize oscillation, and nonzero inertia can help maintain contact.

Gershon and Baruch also recommended that in free-space mode, all (small) inertial force readings due to end-effector inertia be rejected until contact is made. This amounts to suggesting that the robot be position-controlled alone, which makes intuitive sense.

This approach has been claimed to be beneficial in the literature. However, the authors only present an outline of this method, and no formal experiments were ever conducted. Furthermore, the researchers also exposed the risk of instability during the abrupt gain transitions. The literature has dealt with this by ensuring that the damping remains above a certain stable threshold.

Now that the various compliance control strategies have been introduced, the following chapter will describe the hardware that they are implemented on, and the strategies for testing the controller.

Chapter 3

Implementation and Methodology

3.1 The Ranger Manipulator System

As was mentioned earlier, the impedance controller tests in this research were conducted on the Ranger serial link manipulator, shown in Figure 3.1. When all its driven motions are taken into account, Ranger can be referred to as a 10 DOF manipulator: The first eight degrees of freedom stem from 8 revolute joints (R-P-R-P-R-P-Y-R) while the remaining two are (fast and slow) torque-driven tool drives, for a total of ten. However, for this research the tool drives are not operational when the force/torque sensor is mounted at the tool tip, hence Ranger is considered an 8-DOF manipulator.
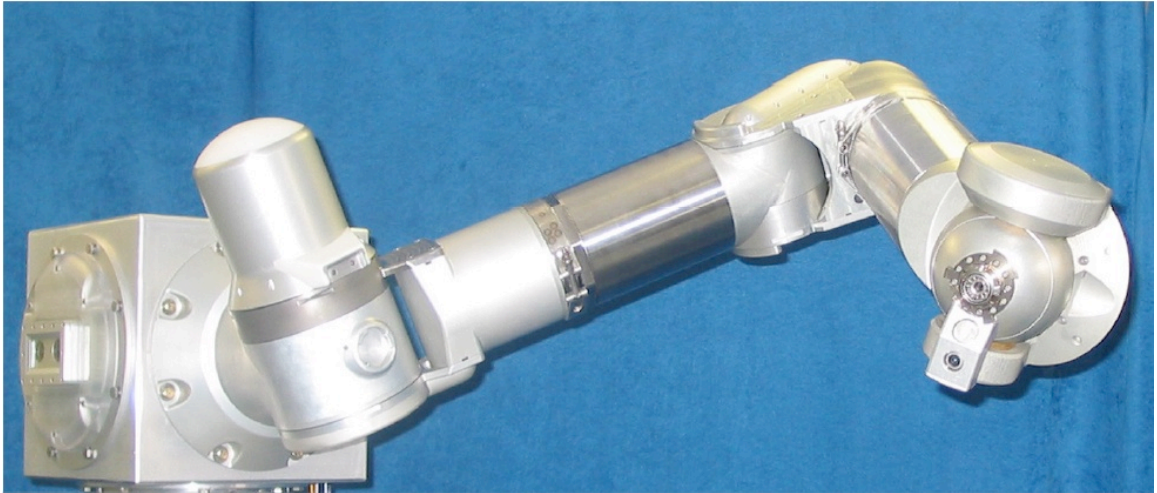
Figure 3.1: Ranger Dexterous Manipulator

3.1.1 Manipulator Configuration

Many "conventional" industrial manipulators limit themselves to 6 degree-of-freedom arms. Despite the advantages of having additional degrees of freedom (namely, singularity and obstacle avoidance) redundant arms are seen predominantly in the research environment due to their added kinematic complexity. The effects and benefits of redundancy on the Ranger manipulator have been studied and strategies for resolving the associated mathematical complications have been implemented [32]. On Ranger, the extra degrees of freedom expand the manipulator's dexterous workspace, allowing it to theoretically assume an infinite number of configurations for a given tool pose, improving obstacle avoidance capability. In turn, this permits the manipulator to move while the tool position remains fixed, referred to as a "self motion". Redundancy also enables smooth planar motions in any direction within the dexterous workspace. This is beneficial for impedance control as is allows the manipulator to be compliant in directions tangent to its current path.

Kinematics*:*

To simplify redundancy management, Ranger is kinematically partitioned into a 4-DOF upper arm and a 4 axis-intersecting wrist. Ranger's redundancy is resolved using the roll angle of the shoulder-elbow-wrist (SEW) plane, illustrated in Figure 3.2. By introducing the SEW angle, the upper arm joint angles and consequently the wrist position can be calculated independently of the wrist joint angles. Furthermore, the self-motion of the SEW rotation is used to avoid the wrist singularity.
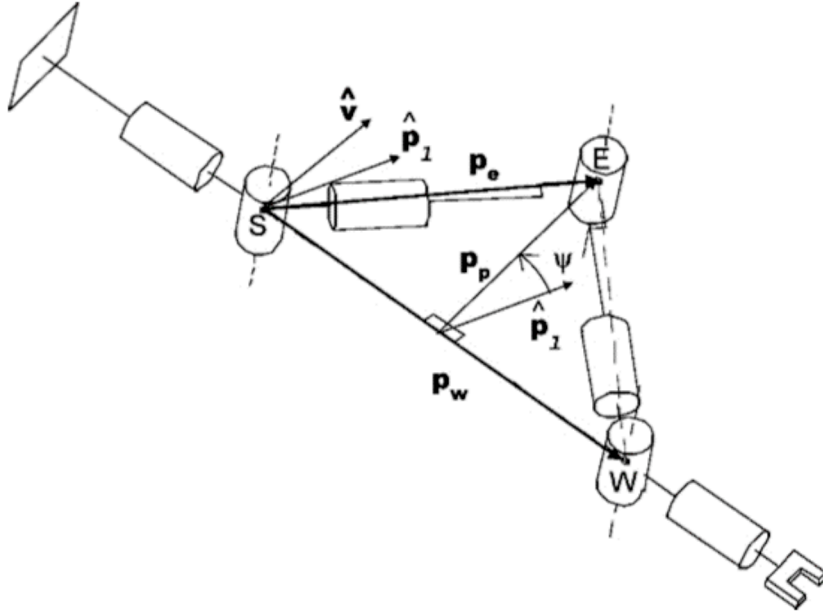
Figure 3.2: SEW roll angle for a 7-DOF manipulator (from [32])

Forward kinematics were straightforward to obtain, and based on previous research of SEW kinematics with a 7-DOF manipulator [33]. Using modified Denavit-Hartenberg (DH) notation and link frame assignments seen in Figure 3.3, Ranger's forward kinematics are derived in [32]. Ranger's D-H parameters are shown in Table 3.1.

i	α_{i-1}	a_{i-1} (rad)	d_i (m)	θ_i
1	0	0	0.1524	θ_1
2	$\pi/2$	0	0	θ_2
3	$-\pi/2$	0	0.5389	θ_3
4	$\pi/2$	0	0	θ_4
5	$-\pi/2$	0.1524	0.5117	θ_5
6	$\pi/4$	0	0	θ_6
7	$\pi/2$	0	0	θ_7
8	$-\pi/2$	0	0	θ_8

Table 3.1: Ranger D-H Parameters
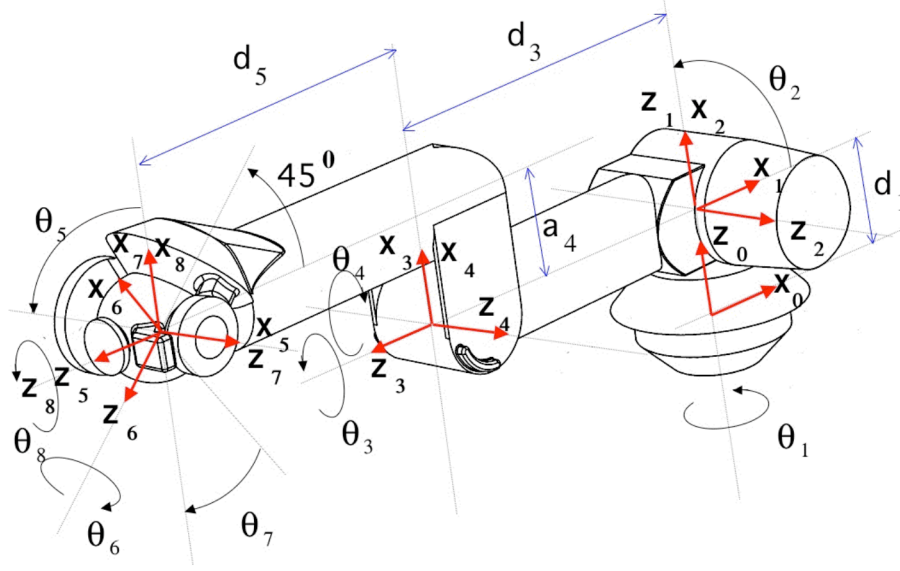
Figure 3.3: Link Frame Assignments for the Ranger 8 DOF Manipulator [34]

Given the arm's redundancy, Ranger's inverse kinematics posed a much greater computational difficulty. Multiple, and sometimes infinite, solutions of joint angles exist for a given tool position. The problem was simplified in [32] by dividing the manipulator into 2 segments: the upper arm, consisting of joints 1-4, and the wrist joints 5-8. Different solving algorithms are employed for each. The upper arm solution uses the Extended Jacobian Method, where the Jacobian matrix is augmented by adding an additional controllable DOF, namely the SEW angle. The wrist solution involves the General Inverse Method, which finds a locally optimal solution based on joint velocities and constraints on specific wrist, tool and forearm orientations. Extra singularities introduced by the skew-axis design of the wrist prevent the use of the Extended Jacobian method. A flow chart of the inverse kinematic solution is illustrated in Figure 3.4.
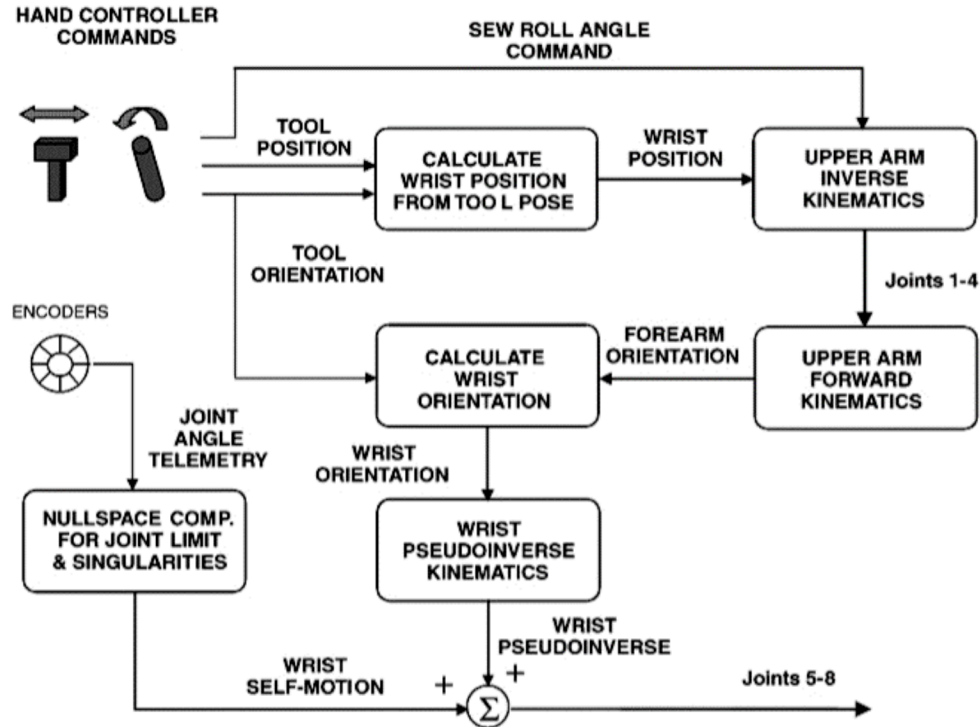
Figure 3.4: Inverse kinematics flowchart for Ranger (from [32])

Workspace and Singularities:

Ranger has a reach of 135 cm when fully extended. As in all serial manipulators, boundary singularities exist in this configuration. Moreover, precariously large joint torques are required to hold the arm in an outstretched position, further limiting the manipulator's workspace. However, Ranger's dual-redundancy ensures that the dexterous workspace is almost as large as reachable workspace. By properly choosing the SEW angle and using the skew axis wrist design, Ranger can effectively avoid most singularities in its reachable workspace. A more detailed workspace description is currently not available because Ranger's dexterous workspace has yet to be fully characterized.

Singularities are present in both the upper arm and wrist segments. By avoiding motion to the workspace boundary, external singularities can be circumvented. Conversely, internal singularities (i.e. singularities occurring within the useable workspace) are more difficult to analyze, and can be detrimental to the inverse kinematics computations by causing a loss of rank and invertibility in the Jacobian matrices [35][36]. It should be noted that by augmenting the degrees of freedom, more singularities are introduced. However, due to the supplementary configurations that are made possible, some singularities are also more easily avoided.

Fortunately, upper arm singularities happen to lie outside the usual workspace. One such occurs when the arm is extended straight to the side, a configuration that is not commanded during normal operation. The only other singularity occurs when the shoulder pitch angle is zero, but this can be avoided by holding the shoulder roll angle fixed.

Singularities in the wrist generally cause a loss of one degree of freedom, reducing the wrist's redundancy. A special case exists where two degrees of freedom are lost and can only be recognized by uncharacteristically large commanded joint velocities. Ranger is designed to deal with these more severe singularities by halting once the joint velocities are above a specified threshold. At this point the operator would need to reverse and re-plan the motion to avoid the singularity.

Achieving compliance near a singularity is especially difficult because the higher joint velocities or joint torques in those configurations cannot be stabilized. Thus, for the compliance tests to follow, we will choose configurations that lie within

the dexterous workspace, far from the reachable workspace boundary and its associated singularities.

3.1.2 Technical Specifications

Ranger is capable of operating in 1-G, underwater and in vacuum. In the interest of safety and time, the experiments carried out in this research were all conducted in an ambient 1-G laboratory environment. The SSL possesses a waterproof force/torque sensor but there is presently no means to attach it in a sealed manner. Designing a proper housing was outside the scope of this research, yet it is an important future consideration.

Velocity and Force*:*

Ranger is capable of a maximum linear tool tip velocity of 1 m/s (40 in/s). In 1-G it can exert a maximum lift of 133 N at full extension and 267 N in a "working" configuration. In terms of compliance control, this establishes a limit at which the manipulator motor torques will saturate and no longer be able to push against a surface. However, to prevent arm and actuator damage, this scenario will be avoided.

Accuracy:

Static and dynamic tests (conducted in compliance with ANSI/RIA R15.05-1-1990 and ANSI/RIA R15.05-2-1990 standards, respectively) have been previously conducted to determine the positional performance of the manipulator [37][38]. Results indicate a static accuracy of approximately 20 mm, static repeatability of about 0.5 mm and a static compliance of at worst 0.4 mm/kg applied load at maximum reach. In terms of control, the static compliance above corresponds to a

manipulator stiffness of roughly 25000 N/m. However, it is worth mentioning that 25000 N/m is a lower bound and valid only in the outstretched position, at which the manipulator is most flexible. In dynamic path-following tests, Ranger demonstrated an average Cartesian accuracy of 1 mm with a repeatability of 1 mm, and a Cartesian cornering radius of 10 mm.

Controller:

The LPU controls the inner loop servo, which runs at 750 Hz, while the impedance and overall control loop run in the DMU at 125 Hz. The inner loop position is P-D controlled and receives joint angle commands generated from the DMU directly (in joint-by-joint mode) or indirectly through the inverse kinematics of a Cartesian position (in resolved rate mode). The controller and manipulator model will be addressed further in Chapter 4.

3.1.3 Force/Torque Sensor Specifications

The force/torque sensor used is a JR3 100M40A, shown in Figure 3.5. It is rated for a maximum load of 800 N in the "z" direction (normal to the sensor face), and 400 N in the "x" and "y" directions. The maximum torque rating is 40 N-m in all directions. Force is digitized to 15 bits in each direction (14 bits magnitude and 1 for sign), producing a resolution of 24.4 mN laterally ("x/y") and 48.8 mN axially ("z"). Force amplification and conversion is done onboard the sensor. Output is then sent to a JR3 PCI driver card for signal processing. The sensor and card provide decoupled and digitally filtered data at 8kHz per channel.

Figure 3.5: JR3 Force/Torque Sensor

3.1.4 Force/Torque Sensor Mounting and Alignment

The sensor is attached to the wrist with an adapter plate and cone, as shown in Figure 3.6. This cone was originally bolted directly to the wrist, but an adapter was made so that it could be fitted with the interchangeable end-effector mechanism (IEEM), and more easily switched out.

For the purposes of the controller, the sensor frame is assumed to be the same as the tool frame, only translated axially by the distance between the tool tip and the exposed end of the force sensor. However, while the outward (z) directions are aligned in both frames, the x and y direction might be arbitrarily offset. This occurs

because Ranger's hand roll frame (8) does not have an absolute reference position relative to the tool frame (S). Whenever Ranger's controller is re-started, the eighth joint, which controls the roll of the sensor, is automatically zeroed. There is no sensor to determine the tool offset. Thus, upon robot start-up, the sensor axes must be carefully aligned with the tool frame axes in joint-by-joint mode, and then zeroed so the sensor and tool frame are aligned. While this procedure is certainly inconvenient, it only need be done once, as long as the operator remembers to return the robots joints to the zero position before the control power is turned off.

The sensor is mounted external to the robot, so that forces are transmitted directly to it, by way of a faceplate, which may have a "finger"-like tool attached to it. Ideally, a useful tool (like a gripper or bolting tool) would be attached, but for the purposes of testing the controller, more expendable end-effectors are used. These are discussed in Section 3.3.1.
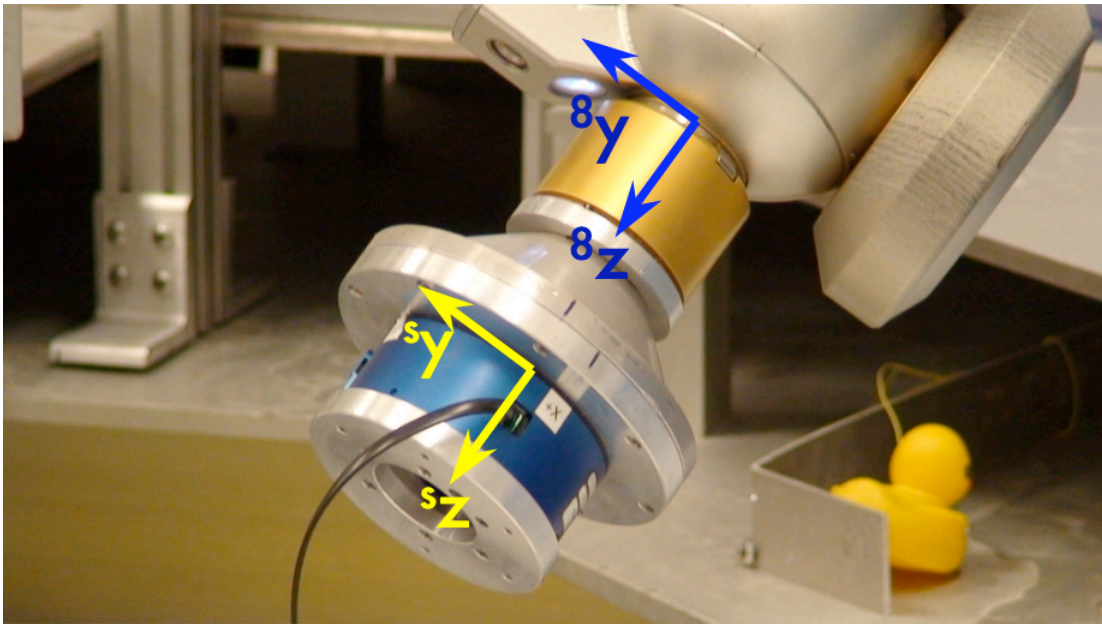
Figure 3.6: Force/Torque Sensor Mounted to Wrist via IEEM.

3.2 Gravity Compensation

Testing a force controller in 1-G carries with it the extra burden of gravity. The sensor is mounted to the attachment plate in such a manner that the forces are read at the end of the sensor that is closer to the wrist. Thus, under gravitational loading, the sensor records the force of its own weight, as well as the induced moment it causes. Additionally, it will also measure the weight/moment due to any attachment or end effector at the free end. This is illustrated in Figure 3.6. For an admittance controller that relies on external forces to adjust its position, these extra forces contaminate the readings and must be removed. If not, the arm will move in the direction in which gravity pulls the end effector. If the mass properties of the end-effector are known, and the orientation of the gravity vector can be found via frame transformations, the forces due to gravity can be calculated and removed. However, Ranger is a robot that uses multiple end effectors, some of which grasp payloads of potentially unknown mass characteristics, thus it is difficult to characterize what the compensating force should be. One remedy is to re-zero the force sensor whenever the end effector changes. This works as long as the arm maintains its orientation. If the orientation changes slightly, gravity forces will re-appear. In order to avoid this hassle, a procedure is used to automatically find the proper gravity compensation.
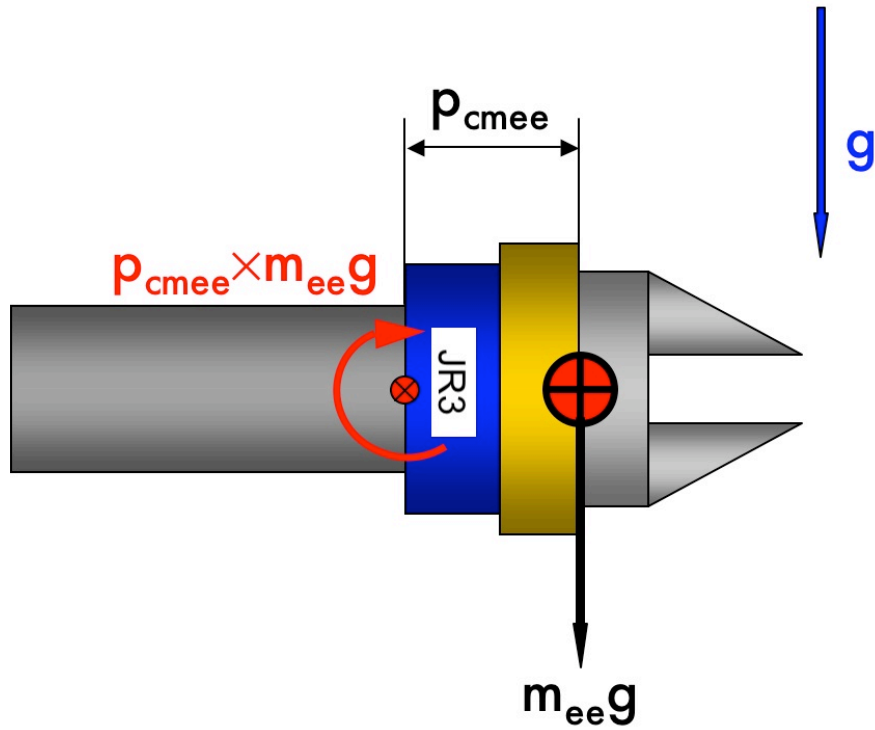
Figure 3.7: Gravity Forces Acting on End-Effector

The external location of the sensor facilitates the gravity compensation. As shown in Figure 3.6, if the mass and center of mass of the end effector are known, finding the compensating forces is straightforward. Assuming the sensor and tool frames are aligned, the compensating force, F, in the sensor frame, s, is given as:

$$^{s}\mathbf{F}_{comp} = m_{ee}\,^{s}\mathbf{g} \tag{3.1}$$

Where $^{s}\mathbf{g}$ is the force of gravity expressed in the sensor frame. This can be obtained from the world frame (or in Ranger's case the Shuttle frame) by a matrix transformation.

$$^{s}\mathbf{g} = {}^{s}R_{8}\,{}^{8}R_{0}\,{}^{0}R_{shuttle}\,{}^{shuttle}\mathbf{g} \tag{3.2}$$

The world frame gravity vector is of course given by

$$^{shuttle}\mathbf{g} = \begin{bmatrix} 0 & 0 & -9.81 \end{bmatrix} \tag{3.3}$$

The matrix transformations are the standard ones used on Ranger obtained from the D-H parameters.

Once the gravity force is obtained, the compensating moment is simply calculated as:

$$^{s}\mathbf{M}_{comp} = \mathbf{p}_{cmee} \times m_{ee}\,{}^{s}\mathbf{g} \tag{3.4}$$

Where $\mathbf{p}_{cmee}$ is the vector from the origin of the sensor frame to the center of mass of the end-effector.

3.2.1 Mass Estimator Algorithm

Of course, in order to determine these compensating forces, the mass and center of mass of the end effector must be determined. These may be determined experimentally, or numerically with CAD software. However, it would be convenient if the robot could determine this automatically. By having a force sensor, the robot already possesses a way to determine mass, and by using arm telemetry, and moment readings it should be able to determine the center of mass as well. Consider the simple planar example, for a uniform symmetrical mass, shown in Figure 3.7 below.
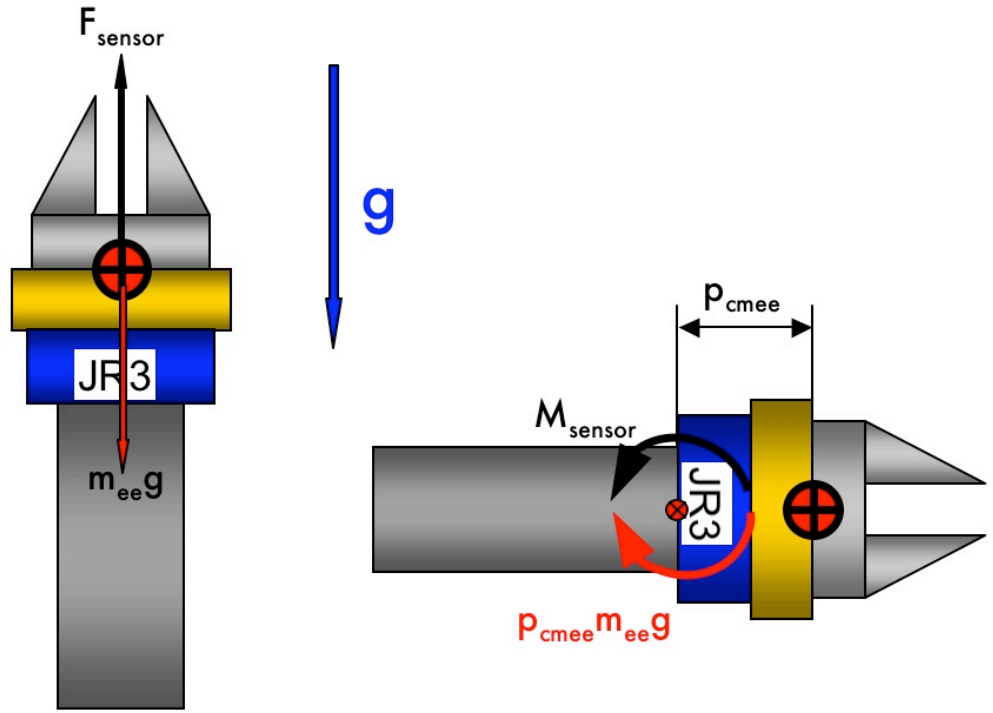
Figure 3.8: Planar Mass Estimation

If the manipulator is pointed upward, then the weight of the end-effector is recorded, and its mass can be extracted simply as:

$$m_{ee} = \frac{F_{sensor}}{g} \qquad (3.5)$$

If the manipulator is then rotated 90 degrees, and the gravitational torque is recorded, since the mass is now known, the center of mass can be calculated as:

$$p_{cmee} = \frac{M_{sensor}}{m_{ee}g} \qquad (3.6)$$

For an arbitrary, asymmetric mass, the procedure is analogous, but must be extended

to the third dimension. The values of m_{ee} and p_{cmee} can be determined as follows:

1. Move the arm to at least 2 different positions (in a different orientation)

2. Register and store readings of the force and torque at each position

3. Perform a least-squares computation on the readings to determine the minimum mass and center of mass.

1. Arm Motion:

The arm motion is accomplished by running a trajectory to a given set of joint angles. Multiple waypoints are necessary due to the method of solution, which will be discussed later. More waypoints increase the accuracy of the estimate. The algorithm run on Ranger uses 4 points because this seems to be the point of diminishing returns. Orthogonal positions are chosen to reduce the redundancy of the data. Namely, the orientations chosen are with the tool tip pointed up, pointed forward, pointed down and pointed at 45 degrees. These are shown below for Ranger.

2. Storing readings from the force/torque sensor:

At each arm position, the trajectory pauses for five seconds to read forces and torques. Measurements are stored in the matrices Y_F (forces) and Y_N (moments), and constructed as follows:

$$\mathbf{Y_F} = \begin{bmatrix} \mathbf{F_{S1}} \\ \mathbf{F_{S2}} \\ \vdots \\ \mathbf{F_{Sp}} \end{bmatrix} \text{ and } \mathbf{Y_N} = \begin{bmatrix} \mathbf{N_{S1}} \\ \mathbf{N_{S2}} \\ \vdots \\ \mathbf{N_{Sp}} \end{bmatrix}, \ \mathbf{F_{Sp}} = \begin{bmatrix} f_{Xp} \\ f_{Yp} \\ f_{Zp} \end{bmatrix} \text{ and } \mathbf{N_{Sp}} = \begin{bmatrix} n_{Xp} \\ n_{Yp} \\ n_{Zp} \end{bmatrix} \quad (3.7)$$

Where F_{Sp} is the force reading at position, p, and is the moment reading at position, p.

3. Calculation of m_{ee} and p_{cmee}:

We express the gravity vector in the tool frame, at a given pose p, as:

$$\mathbf{g_{Tp}} = \begin{bmatrix} g_{Tx} \\ g_{Ty} \\ g_{Tz} \end{bmatrix} \tag{3.8}$$

The force due to gravity is then expressed as:

$$\mathbf{F_{Sp}} = m\mathbf{g_{Tp}} \tag{3.9}$$

Similarly, the moment due to gravity can be expressed as:

$$\mathbf{N_{Sp}} = \mathbf{p_{cmee}} \times m\mathbf{g_{Tp}} = mG_{Tp}\mathbf{p_{CMEE}} \tag{3.10}$$

where G_{Tp} is the cross-product matrix for $\mathbf{g_{Tp}}$, given by:

$$G_{Tp} = \begin{bmatrix} 0 & g_{Tz} & -g_{Ty} \\ -g_{Tz} & 0 & g_{Tx} \\ g_{Ty} & g_{Tx} & 0 \end{bmatrix} \tag{3.11}$$

$\mathbf{p_{cmee}}$ is the position vector of the center of mass, given as: $\mathbf{p_{cmee}} = \begin{bmatrix} x_c \\ y_c \\ z_c \end{bmatrix}$
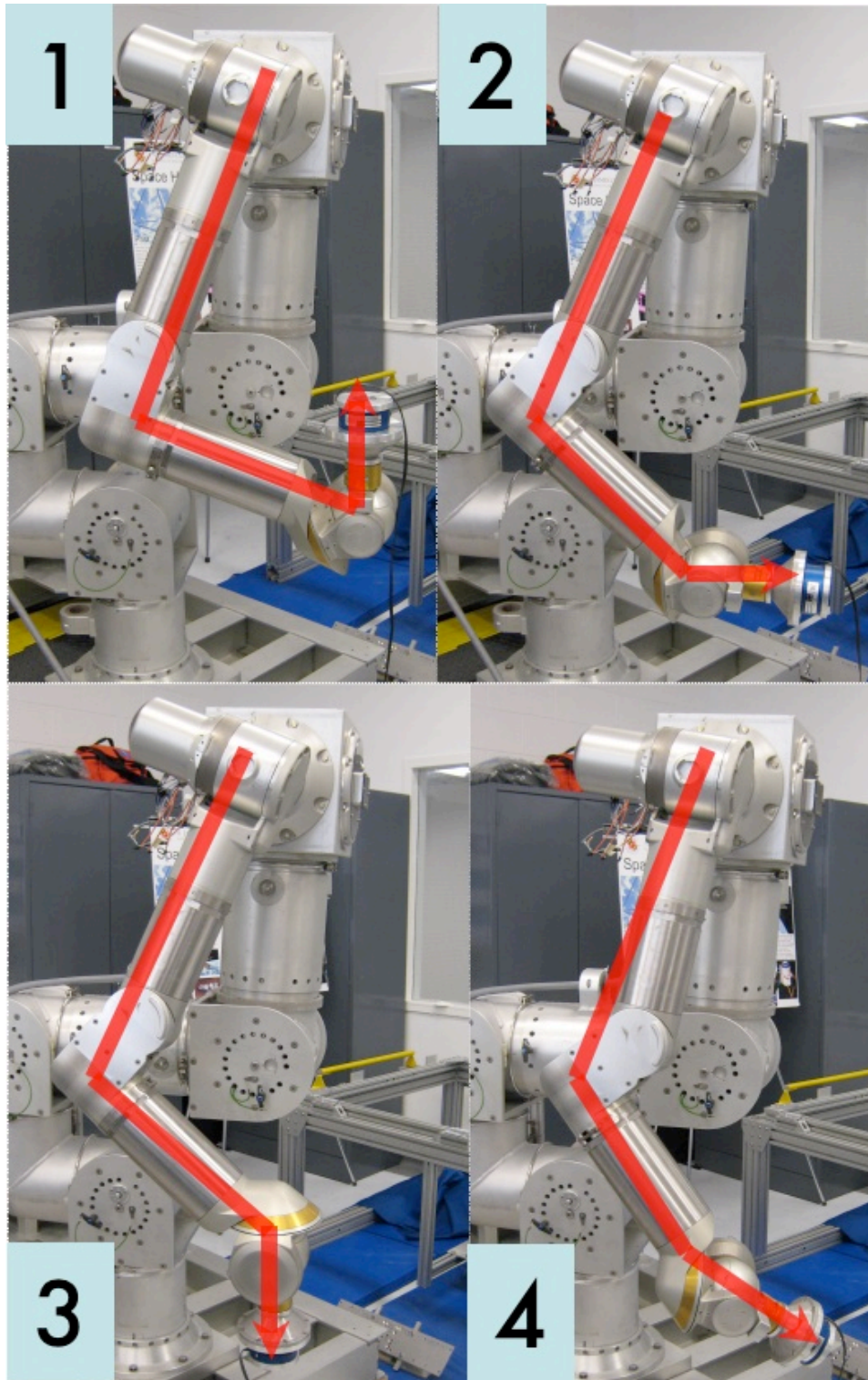
Figure 3.9: Arm Positions for Mass Estimation

Alternatively, this can be written as:

$$\mathbf{N_{Sp}} = m \begin{bmatrix} 0 & g_{Tpz} & -g_{Tpy} \\ -g_{Tpz} & 0 & g_{Tpx} \\ g_{Tpy} & -g_{Tpx} & 0 \end{bmatrix} \begin{bmatrix} x_c \\ y_c \\ z_c \end{bmatrix} \tag{3.12}$$

Note that at this juncture, it is impossible to solve for x_c, y_c and z_c. The solution to the matrix equation would be of the form $p_{CMEE} = \left(G_{Tp}^{-1} N_{Sp} \right) \dfrac{1}{m}$. However, G_{Tp} is a 3×3 skew-symmetric matrix, and therefore non-invertible because all skew-symmetric matrices of odd dimension are singular.

More than one set of readings must therefore be taken, and the approach to solution is slightly more intricate. As each subsequent reading is taken, the matrices are "stacked" to generate:

$$\mathbf{Y_F} = \begin{bmatrix} \mathbf{F_{S1}} \\ \mathbf{F_{S2}} \\ \vdots \\ \mathbf{F_{Sp}} \end{bmatrix} = m \begin{bmatrix} g_{T1x} \\ g_{T1y} \\ g_{T1z} \\ g_{T2x} \\ g_{T2y} \\ g_{T2z} \\ \vdots \\ g_{Tpx} \\ g_{Tpy} \\ g_{Tpz} \end{bmatrix} \tag{3.13}$$

$$\mathbf{Y_N} = \begin{bmatrix} \mathbf{N_{S1}} \\ \mathbf{N_{S2}} \\ \vdots \\ \mathbf{N_{Sp}} \end{bmatrix} = m \begin{bmatrix} 0 & g_{T1z} & -g_{T1y} \\ -g_{T1z} & 0 & g_{T1x} \\ g_{T1y} & g_{T1x} & 0 \\ 0 & g_{T2z} & -g_{T2y} \\ -g_{T2z} & 0 & g_{T2x} \\ g_{T2y} & -g_{T2x} & 0 \\ \vdots & \ddots & \vdots \\ 0 & g_{Tpz} & -g_{Tpy} \\ -g_{Tpz} & 0 & g_{Tpx} \\ g_{Tpy} & -g_{Tpx} & 0 \end{bmatrix} \begin{bmatrix} x_c \\ y_c \\ z_c \end{bmatrix} \tag{3.14}$$

Equation 3.12 can easily be solved for m using a *left* pseudo-inverse. The pseudo-inverse is used to obtain a least squares solution of a non-square matrix equation. When the set of equations to be solved is over-determined (i.e. has more equations than unknowns) the *left* pseudo-inverse is used.

For a general equation of the form:

$$Y = \psi \gamma \tag{3.15}$$

Where γ is a column vector of length n, ψ is a non-square matrix of dimension m $\times$ n and Y is a column vector of length m. γ is solved using:

$$\gamma = \left(\psi^T \psi \right)^{-1} \psi^T Y = \psi^\dagger Y \tag{3.16}$$

Where $\psi^\dagger = \left(\psi^T \psi \right)^{-1} \psi^T$ is the *left* pseudo-inverse of ψ. When solving for m, designate:

$$\mathbf{Y_F} = \begin{bmatrix} \mathbf{F_{S1}} \\ \mathbf{F_{S2}} \\ \vdots \\ \mathbf{F_{Sp}} \end{bmatrix}, \psi_F = \begin{bmatrix} g_{T1x} \\ g_{T1y} \\ g_{T1z} \\ g_{T2x} \\ g_{T2y} \\ g_{T2z} \\ \vdots \\ g_{Tpx} \\ g_{Tpy} \\ g_{Tpz} \end{bmatrix}, \gamma_F = m \tag{3.17}$$

In the case of $\mathbf{p}_{cmee}$ these become:

$$\mathbf{Y_N} = \begin{bmatrix} \mathbf{N_{S1}} \\ \mathbf{N_{S2}} \\ \vdots \\ \mathbf{N_{Sp}} \end{bmatrix}, \psi_N = \begin{bmatrix} 0 & mg_{T1z} & -mg_{T1y} \\ -mg_{T1z} & 0 & mg_{T1x} \\ mg_{T1y} & mg_{T1x} & 0 \\ 0 & mg_{T2z} & -mg_{T2y} \\ -mg_{T2z} & 0 & mg_{T2x} \\ mg_{T2y} & -mg_{T2x} & 0 \\ \vdots & \ddots & \vdots \\ 0 & mg_{Tpz} & -mg_{Tpy} \\ -mg_{Tpz} & 0 & mg_{Tpx} \\ mg_{Tpy} & -mg_{Tpx} & 0 \end{bmatrix}, \gamma_N = \begin{bmatrix} x_c \\ y_c \\ z_c \end{bmatrix} \tag{3.18}$$

The force psudo-inverse equation is solved first, consequently determining m. Substituting m into ψ_N, γ_N is solved, and $\mathbf{p}_{cmee}$ is obtained.

3.2.2 Testing Gravity compensation

The gravity compensation was tested to determine if the force of gravity was effectively being removed by verifying that the net sensed force at several arm configurations was zero. The end-effector then moved to 4 distinct positions, similar to those shown in Figure 3.9: Pointing up, pointing down, pointing sideways, pointing

45 degrees. The force/torque error was recorded as the deviation from zero. Forces and moments were recorded at each waypoint, for 10 runs.
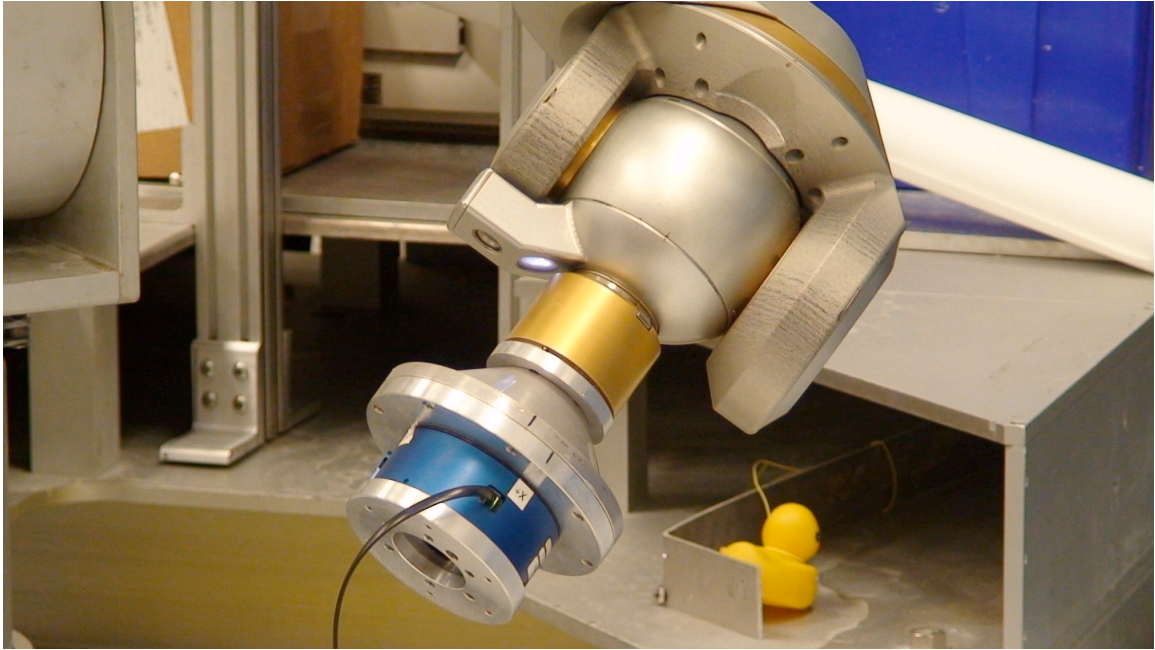
Figure 3.10: Force/Torque Sensor Attached to Wrist

Tests were run with 2 loads: The actual sensor, and a 1kg cylindrical load shown in Figure 3.11. Results are tabulated in Appendix A.

For both loads, with gravity compensation applied, the forces due to gravity were within the range of ±2 N. This corresponds to less than 23% of the expected force reading for the lighter load and less than 13% of the expected force reading for the heavier load. This residual force was due to small vibrations and sensor noise, as well as inaccuracies stemming from sensor preloading. Filtering this force reading with a deadband can eliminate the error, without much consequence on the controller, because contact forces in the 1-2 N range are relatively small.

Torque compensation for the lighter load was relatively accurate, as less than 8% of the gravity torque remained. The heavier load had less than 15% of the expected gravity load leftover. Although this procedure does not eliminate 100% of the gravitational forces, these results validate its use because the net forces that remained have negligible effect on the admittance controller.

Figure 3.11: 1 kg Cylindrical Mass Attached to FTS

3.3 Testing Impedance Control

Most structures that Ranger interacts with in assembly tasks are rigid. As proposed by Anderson and Spong, for minimal interaction force, the manipulator

stiffness will have to be specified as low as possible. The following experiments will determine how low the stiffness can be specified and how much damping is required for stable contact at that stiffness. Although the admittance controller will ultimately have to demonstrate stable behavior in rigid contact, the controller is initially tested in contact with a compliant surface, to ascertain whether the leap to rigid contact can be made safely.

3.3.1 Apparatus

Contact will be made against a flat, vertical surface such that the motion of the manipulator is in the horizontal plane. The flat surface will consist of a metal plate for rigid contact, and a plastic springboard for compliant contact. Both the plate and springboard are affixed to an 80/20 aluminum frame that is clamped down to the manipulator pallet floor support structure (PFSS).

Springboard Design

The springboard consists of two rectangular plastic boards sandwiching two springs. The board's travel is kept linear by means of concentric cylinders around which the springs are placed. The principle is similar to an automotive shock absorber, minus the damper, although there is dry friction between the cylinders that acts as a mild damper.
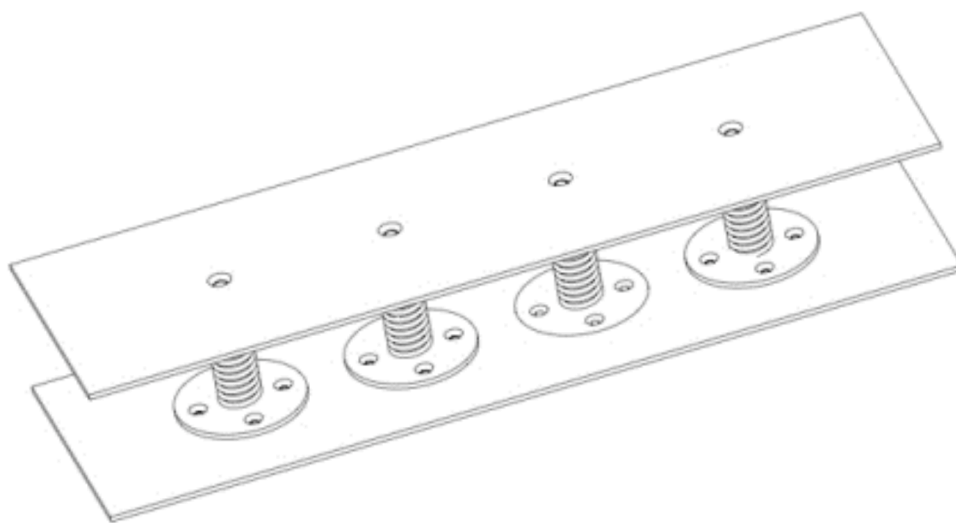
Figure 3.12: Springboard Design Drawing
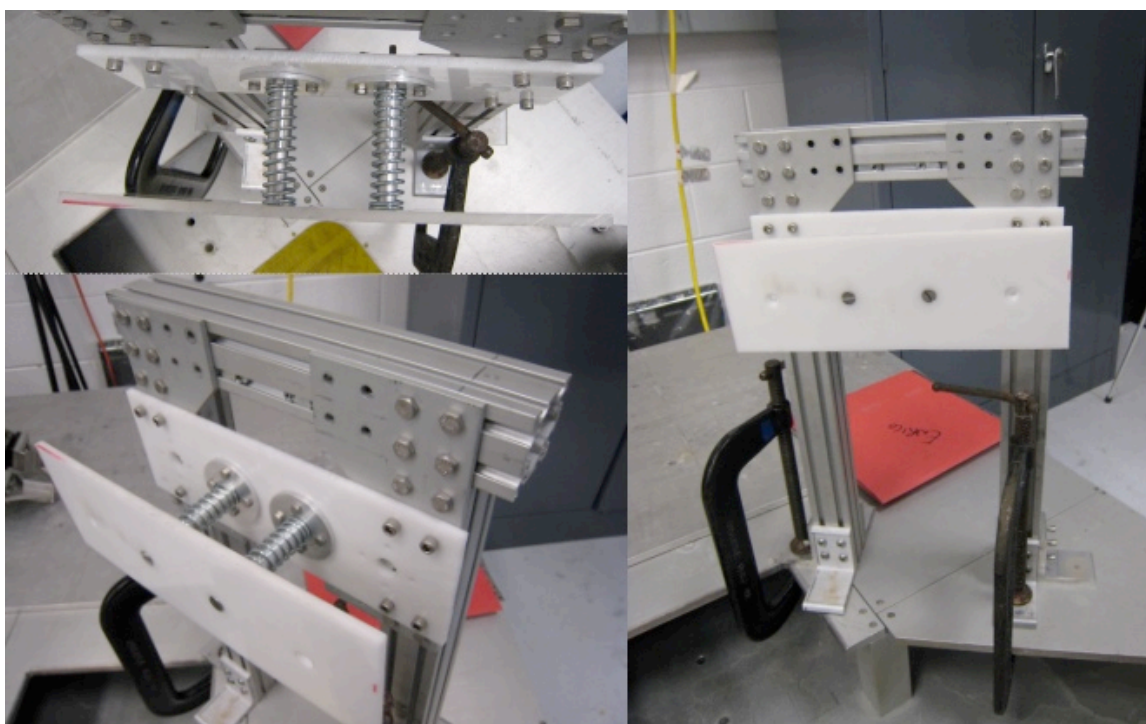
Figure 3.13: Springboard Mounted on 80/20 Frame Clamped to PFSS

The springs used have a stiffness of 3.26 kN/m. Combining two in parallel doubles the stiffness, yielding a spring constant of 7.52 kN/m.

End Effectors for Contact Tests

Ranger will make contact with the surfaces using three different attachments. The first is the plate attached to the end of the force sensor, shown in all figures to this point. The second is an aluminum finger/poker with a plastic tip. The third is a finger with roller bearing tip, to reduce the effect of friction in a sliding motion. The last two are bolted to the first through an adapter plate, as illustrated in Figure 3.14.
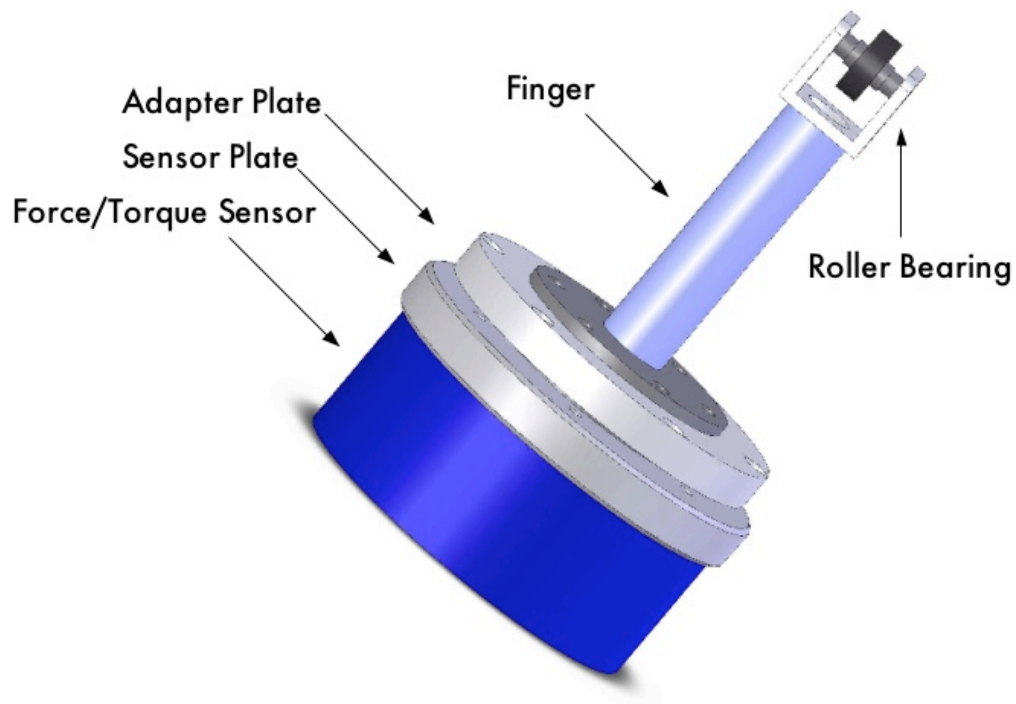
Figure 3.14: End Effector Assembly Drawing

3.3.2 Procedure

As mentioned earlier, the contact motion takes place in a horizontal plane. Two types of contact will be made. The first consists of a single linear motion perpendicular to the contact plane. This will be denoted as the "1-DOF" experiment. The next experiment adds motion parallel to the contact plane, and is denoted as "2-DOF". The rates of the motions can be selected in the Ranger control GUI.
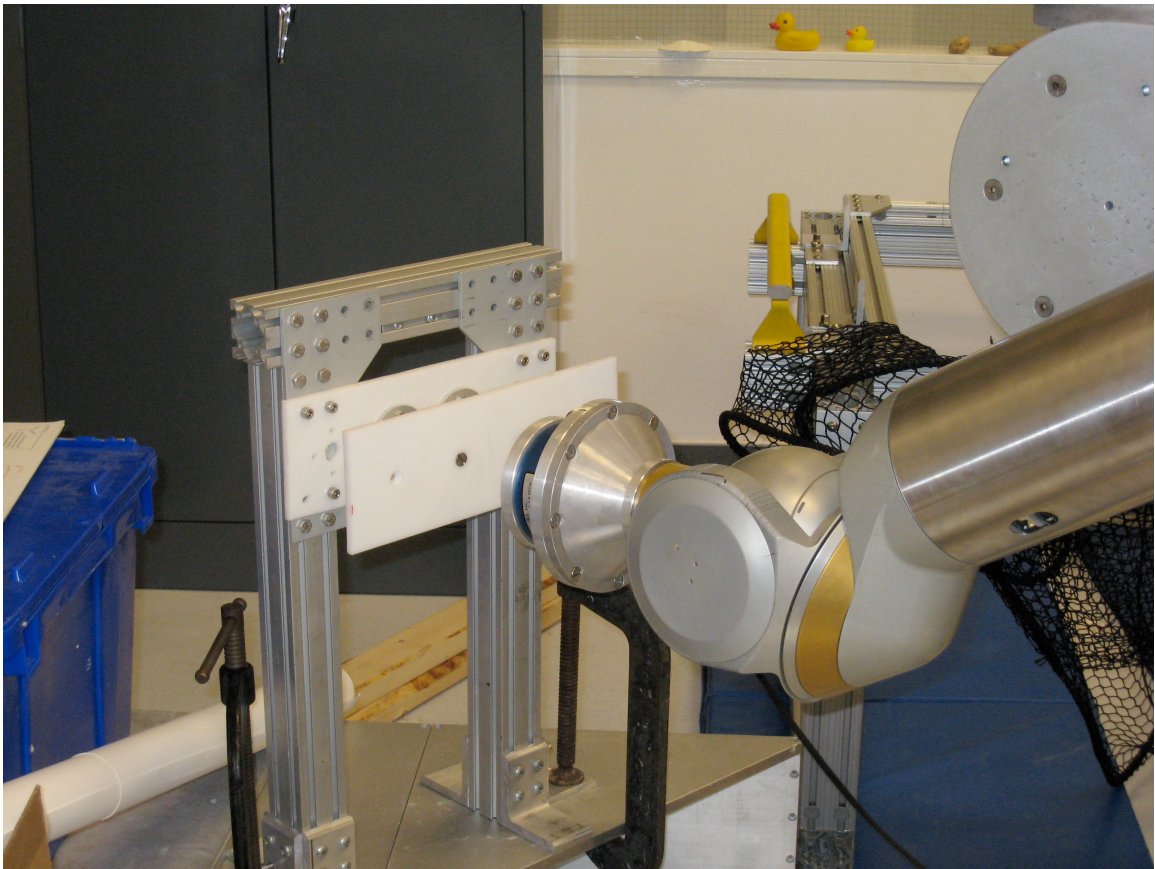
Figure 3.15 Ranger Approaching Springboard

1-DOF Experiment

The 1-DOF experiment is first conducted with the springboard. The lowest stiffness is used, namely 7.5 kN/m, which requires 75 N to compress 1 cm. The

manipulator is positioned to that the force sensor is parallel to the springboard. A Cartesian rate is specified in the z-direction of the tool frame (axially outward) until the manipulator contacts the springboard. A rate is then specified in the opposite direction to withdraw from contact. High stiffness (1000 N/m) and damping (1000 Ns/m) are specified in the lateral and rotational directions, as compliance is not tested in these directions. High stiffness and damping are also initially set in the axial direction. The stiffness is then decreased until instability occurs. The damping is then raised by 100 Ns/m and the stiffness again decreased until instability. The process is continued until no amount of damping will stabilize the chosen stiffness, or the chosen stiffness is zero. The process is then repeated for rigid contact.
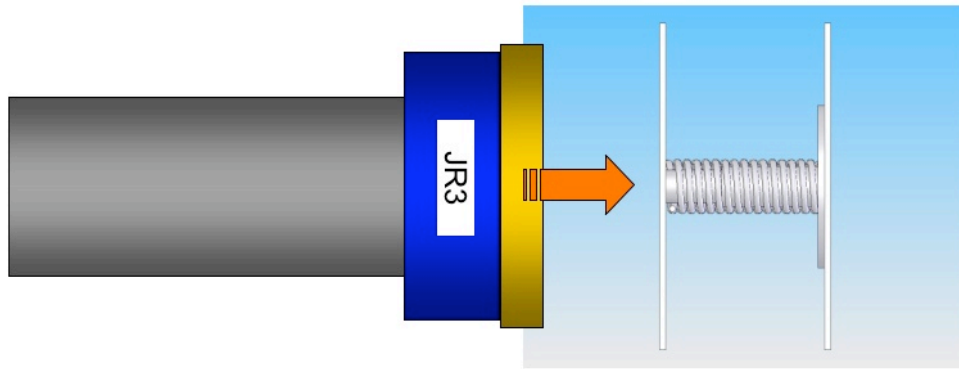
Figure 3.16: Illustration of 1-DOF Experiment

2-DOF Experiment

The 2-DOF test adds motion in the lateral direction. For this experiment the "finger" end-effector is used. The axial stiffness will be set to the lowest, stable

stiffness determined from the 1-DOF experiments. Once contact is made, the manipulator will be commanded to move to the right at a given rate. Lateral stiffness will then be adjusted using the same procedure outlined for the 1-DOF case, and checked for stability. The process will be repeated with both the plastic tipped and roller-bearing-tipped end-effector to determine the influence of friction on stability.
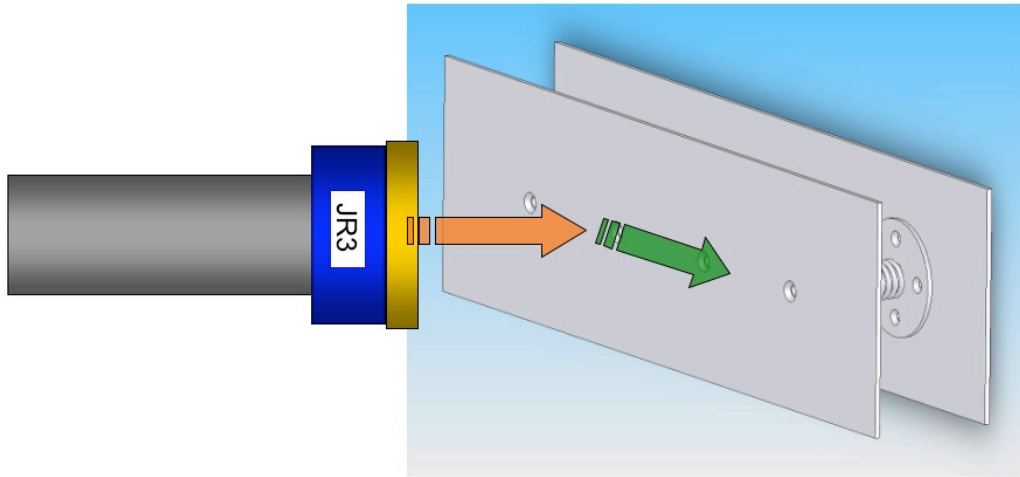
Figure 3.17: Illustration of 2-DOF Experiment

Peg-in-Hole Experiment

After the 2-DOF experiments are complete, the range of stiffness and damping will be well characterized for moving contact. The most compliant of those is then selected for an attempted peg-in-hole insertion. The motion will be identical to the 2-DOF case, except there will be a hole interrupting the motion, through which the finger should pass. Rotational compliance will then be added and compared to the case without.
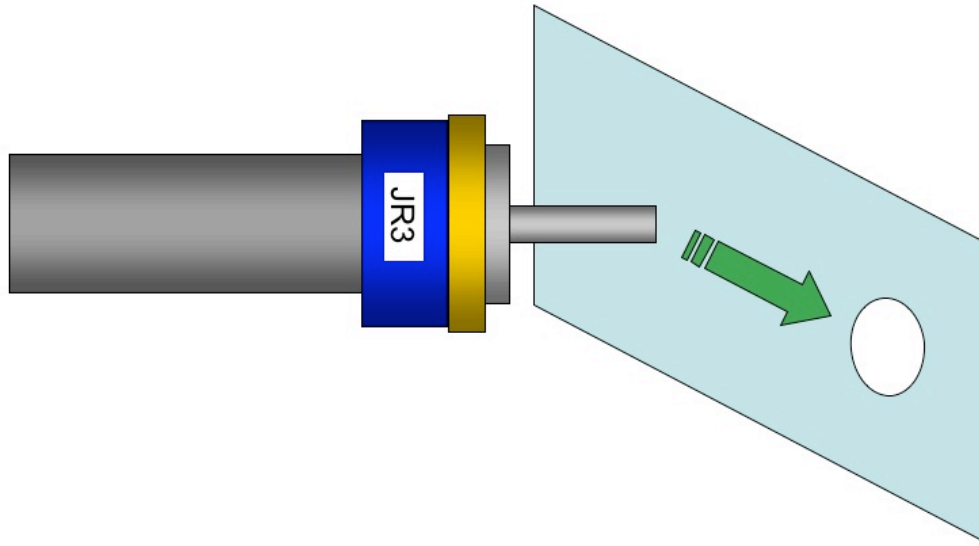
Figure 3.18: Illustration of Peg-in-Hole Experiment

3.3.3   Switching Control

Preliminary tests into a switching controller can be done by repeating the 1-DOF compliant test, but manually switching the gains when contact is made. High manipulator stiffness is selected first, and when contact is made, the gains are switched to a low axial stiffness. It will be determined whether this abrupt change destabilizes the controller. A rigid manipulator should compress the springboard and maintain position, but when the stiffness is reduced, the manipulator should spring back in response.

Before compliance testing can begin, it would be helpful if the controller could be assessed for stability analytically. This could narrow down the search for stable gains by providing theoretical bounds on the stable region.

Chapter 4

Stability Analysis

Smith investigated the stability of the ADEPT controller for a single joint and determined relations between stiffness and damping that resulted in a stable impedance controller. While this analysis certainly gives useful insight into the range of stable gains for this controller, it was performed for an arbitrary link attached to the shoulder motor. Hence, it was unrepresentative of Ranger's actual configuration and factors such as the length and mass of its actual links were not considered.

In the interest of making the analysis more applicable, this chapter extends the stability analysis initiated by Smith to the 2-link case. Although this remains a simplified version of the 8-DOF arm, it captures the major inertial changes in the arm as viewed from the end-effector due to changes in arm configuration. The effect of changing inertia due to arm configuration will be studied.

4.1 Controller Block Diagram

The block diagram for the arm's controller was shown in Chapter 2. The one considered for the stability analysis is slightly different. It has been linearized to allow tools from linear control theory to be applied. This construction, shown in Figure 4.1, was the same generalized diagram used by Smith in her research. However, while Smith chose to further simplify it to the SISO model for 1 joint (Figure 4.2), the analysis presented in this chapter expands the SISO model further and ultimately examines a MIMO implementation.
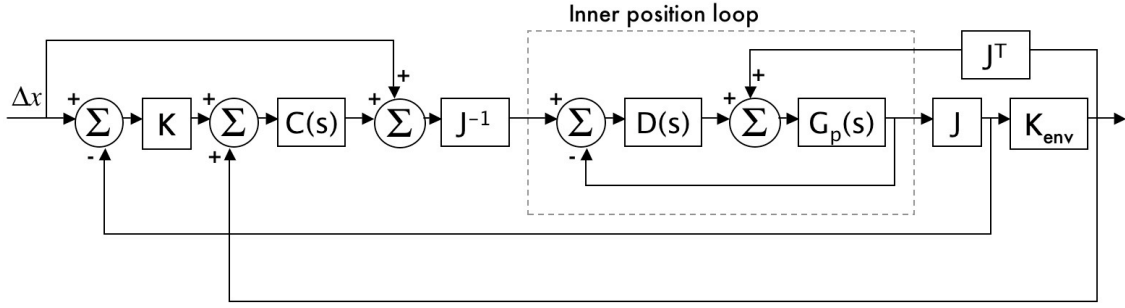
Figure 4.1: Generalized Controller with Simplified Inner Position Servo Loop
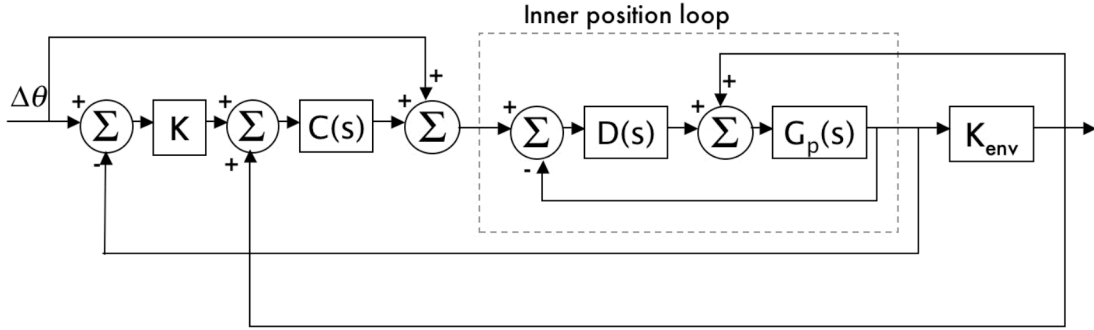
Figure 4.2: Simplified One-DOF Controller

The main difference between the SISO and MIMO implementations is the conversion from joint space to Cartesian space and vice-versa. This is accomplished via the Jacobian, J, or its inverse. Cartesian forces are also translated to joint torques using the Jacobian transpose. In all other aspects, the controllers are identical apart from the SISO model using scalar transfer functions while the MIMO version employs their matrix analogues. The following section explains how their elements are modeled.

4.2 Modeling elements of the controller

As discussed in Chapter 2, both controllers contain the outer admittance loop wrapped around the inner joint position loop. As discussed in Chapter 2, the outer loop feeds back the external torque due to the environment stiffness, K_{env}, and is where the manipulator stiffness, K, is defined. The admittance compensator, C(s) regulates the manipulator inertia and damping. All of these parameters will be examined for their impact on stability. The inner loop is governs the joint motors, represented by the plant model, $G_p(s)$, using a proportional-derivative (P-D) controller, D(s). In order to avoid redundancy in the following sections, the controller components will be described in their MIMO configuration, where the SISO model is merely a subset of this.

4.2.1   2-DOF Arm Model

The MIMO model considered is a 2-link manipulator model based on the dimensions of the upper and lower arm of Ranger, shown in Figures 4.3 and 4.4. The upper arm consists of the shoulder roll joint and upper arm link, while the lower arm is comprised of the elbow pitch joint, the forearm link and the wrist. For the purposes of the stability analysis, the arm dimensions as well as arm component masses and center of masses were obtained from the Arm Dimension and Weight Measures Test Report [39]. The underlying assumption behind this simplified analysis is that the arm is comprised of uniform links with a lumped mass at the center of gravity of each link, as dictated by the test report. Furthermore, the arm motion is restrained to the planar motion illustrated in Figure 4.4. This assumption is not without justification, as

the bulk positioning motion of the arm is generally accomplished though rotation of the shoulder roll and elbow pitch joints.
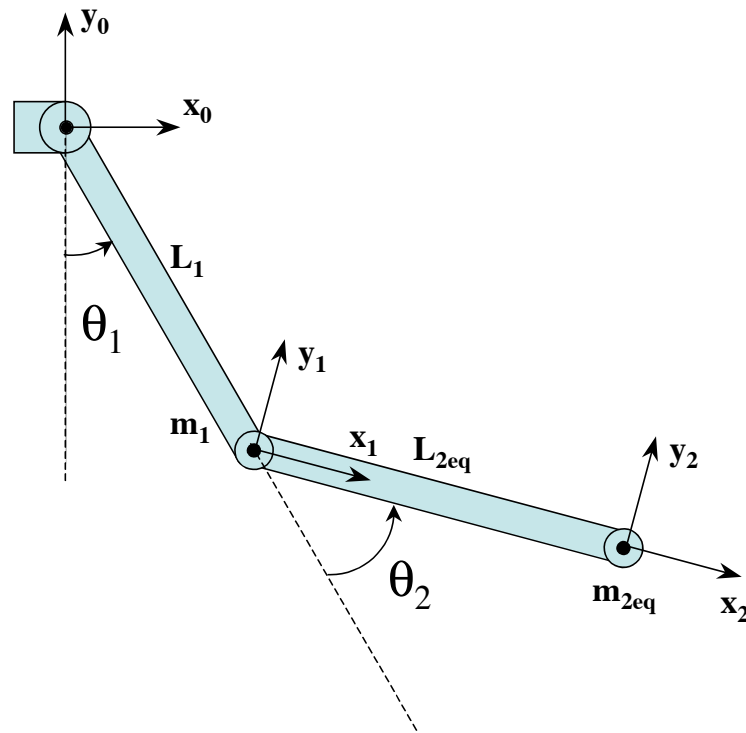
Figure 4.3 Ranger Simple 2-DOF Model
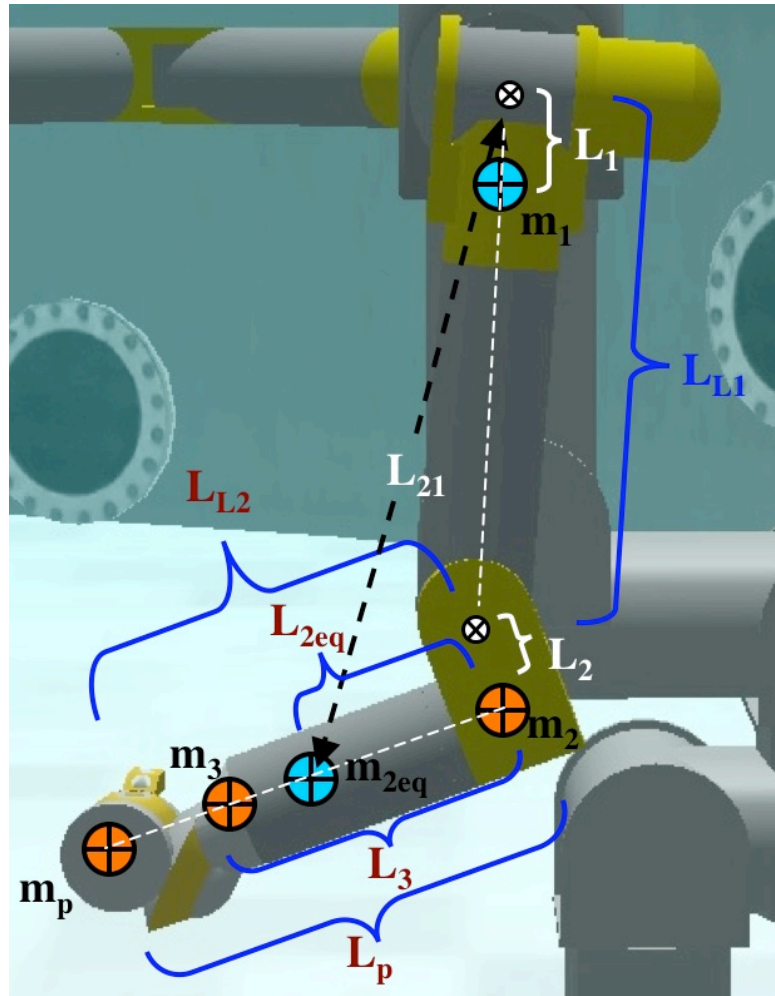
Figure 4.4 Ranger 2-DOF Dimensions (photo from graphical simulation)

4.2.2 Link Inertia

To calculate the link moment of inertia, the links are modeled as pendulums. A simple lumped mass model is used:

$$J_L = mL^2 \qquad (4.1)$$

Where L is the effective length from the joint rotation center to the location of the lumped mass center. Referring to the 2-link manipulator model shown in Figure 4.4, L_1 is denoted as the distance from the shoulder to the mass center of the first link. L_{L1}

is the length of the first link, from shoulder to elbow. L_2 is the distance from the elbow joint to the mass center of the second link. L_{2eq} is the distance to the equivalent mass center of the second link that includes the mass of the wrist and payload. This is determined as a mass-weighted equivalent length:

$$L_{2eq} = \frac{m_2 L_2 + m_3 L_3 + m_p L_p}{m_2 + m_3 + m_p}$$

(4.2)

Where m_3 is the mass of the third link (i.e. the wrist) L_3 is the distance between the elbow joint and the wrist mass center, m_p is the payload mass and L_p is the distance between the elbow joint and the tool tip (where the payload is assumed to be located). The known values from the aforementioned test report are presented in table 4.1.

Link Length	Value (m)	Link Masses	Value (kg)
L_1	0.057	m_1	22.68
L_{L1}	0.54	m_2	21.90
L_2	0.076	m_3	21.90
L_{L2}	0.677	m_p	0-15
L_3	0.446		
L_p	0.677		

Table 4.1 Link Length and Mass Parameters

L_{21} is then denoted as the effective distance between the shoulder joint and the equivalent mass center of the second link. An expression is found using the law of cosines:

$$L_{21} = \sqrt{L_{L1}^2 + L_{2eq}^2 + 2L_{L1}L_{2eq}\cos\theta_2}$$

(4.3)

Those are determined as follows:

$$J_{L1} = m_1 L_1^{\,2} + m_{2eq} L_{21}^{\,2} \tag{4.4}$$

$$J_{L2} = m_{2eq} L_{2eq}^{\,2} \tag{4.5}$$

Where:

$$m_{2eq} = m_2 + m_3 + m_p \tag{4.6}$$

Thus, the moment of inertia at the first joint thus depends on both the first and second link, while the moment of inertia at the second joint only depends of the second link. Effectively, the mass of the shoulder roll joint and the elbow roll joint are lumped into the upper arm link mass. The mass of the forearm link is lumped from the mass of the elbow pitch joint and the wrist mass, as well as any payload that is attached to the wrist.

It is important to note here that the inertia of the arm varies with two parameters: The payload mass, m_p, and the arm configuration, dictated by θ_2. Since the arm inertia is a predominant factor in the plant model, the effect of variable inertia due to configuration and payload mass on arm stability will be analyzed. Increasing the mass of the payload will move the center of mass of the second link away from joint 2. Increasing θ_2 brings the second link mass center closer to the shoulder and thus reduces the effective inertia at that joint, possibly having a stabilizing effect.

4.2.3 Plant Model

Since Ranger's inner loop position servo is an independent joint controller, the plant is modeled as two individual joints, G_{p1} and G_{p2}, each with their own model

parameters. The motor model is the same simple inertial model used by Smith.

$$G_p = \begin{bmatrix} G_{p1} & 0 \\ 0 & G_{p2} \end{bmatrix} = \begin{bmatrix} \dfrac{1}{J_{p1}s^2 + B_{p1}s} & 0 \\ 0 & \dfrac{1}{J_{p2}s^2 + B_{p2}s} \end{bmatrix} \tag{4.7}$$

Where J_{pi} is the effective output inertia and B_{pi} is the effective output damping at the joint of the motor-link system. The effective inertia combines the link inertia with the output motor inertia, which is simply the motor inertia multiplied by the harmonic gear ratio, η, obtained from [40].

$$J_{pi} = J_{Li} + \eta^2 J_{mi} \tag{4.8}$$

For Ranger, $J_{mi} = 4.8 \times 10^{-4}$ N-m/kg, and J_{Li} is obtained as in section 4.2.2. Similarly, for the joint damping:

$$B_{pi} = B_{Li} + \eta^2 B_{mi} \tag{4.9}$$

For damping, it was assumed that the links had no damping, and the motor damping is given as $B_{mi} = 2.3 \times 10^{-5}$ Nms/rad. For both joints, the gear ratio is 101. Thus, the effective damping is $(2.3 \times 10^{-5}) \times 101^2 = 0.235$ Nms/rad, and can be set to zero since the plant model will be dominated by the inertial term.

4.2.4 P-D Controller

A simple proportional-derivative controller is used for joint position tracking. On Ranger, gains can be set differently for each joint, although in practice they are currently all equal.

The input-output motor model is adjusted to reflect how the actual motor

control is accomplished, shown in Figure 4.5. For instance, the P-D controller in the

LPU accepts positions/velocities in incremental encoder counts and outputs digital

torque counts, while the model accepts radians for input and outputs the torque in

Newton-meters. Several conversions were needed to obtain the correct units [41]. The

conversion factor for radians to counts is $\kappa_s = 43726$ at the shoulder and $\kappa_e = 33114$ at

the elbow joint. The conversion from raw torque counts to amperes is $K_T = 20/4096$

and the motor constant, K_a, is 0.159 N-m/ampere. To obtain the output torque, the

motor torque must then be multiplied by the harmonic gear ratio, which for Ranger is

$\eta=101$. Given that the LPU gains on Ranger are set to $K_p = 5$ and $K_v = 25/64$, the

effective gains are then found to be:

$$K_{eff} = \eta \kappa K_T K_a K \tag{4.10}$$

For the shoulder, these work out to: $K_{ps} \approx 17000$ Nm/rad and $K_{vs} \approx 1300$

Nms/rad, while for the elbow these values are: $K_{pe} \approx 12900$ Nm/rad and $K_{ve} \approx 1000$

Nms/rad. In the block diagram, the implementation is then:

$$D(s) = \begin{bmatrix} D_1(s) & 0 \\ 0 & D_2(s) \end{bmatrix} = \begin{bmatrix} K_{vs}s + K_{ps} & 0 \\ 0 & K_{ve}s + K_{pe} \end{bmatrix} \tag{4.11}$$
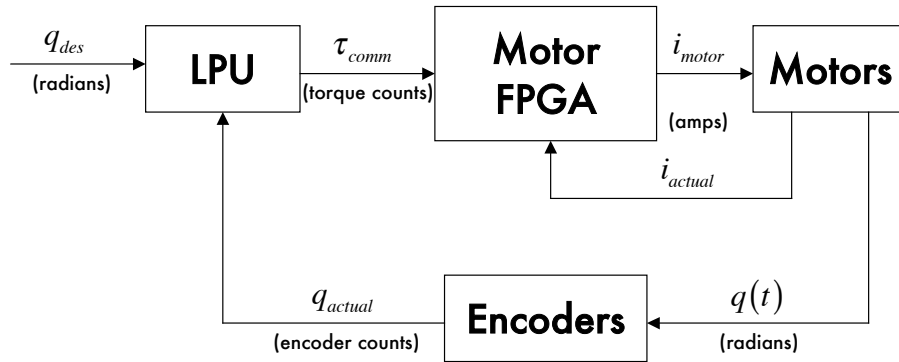
Figure 4.5: Ranger Inner Position Loop

4.2.5 Unmodeled Elements from Ranger Inner Loop

Since the LPU joint controller is implemented in discrete time, some elements were ignored in the continuous implementation to follow. For instance, discrete position measurements are differenced numerically to obtain velocities and filtered digitally to reduce noise. In the analysis, the unfiltered actual velocity is used. The LPU controller also employs thresholding on raw velocities and torques in order to prevent register rollover. This nonlinearity is unmodeled in the analysis. In addition, gravity is unmodeled on Ranger. It is treated as a disturbance to the inner loop, and assumed to be rejected by the P-D controller, since it has been demonstrated that Ranger's static and dynamic accuracy is not severely affected in 1-G [37].

4.2.6 Manipulator Stiffness/Environment Stiffness

There are two stiffnesses associated with the outer control loop: the manipulator, which can specified by the user in any direction, and the environment. The necessary manipulator stiffness and damping required for stable contact with given environment stiffness are evaluated. For the 2-DOF model, these are represented by:

$$K_e = \begin{bmatrix} K_{env,x} & 0 \\ 0 & K_{env,y} \end{bmatrix} \tag{4.12}$$

$$K = \begin{bmatrix} k_x & 0 \\ 0 & k_y \end{bmatrix} \tag{4.13}$$

For simplicity, we will assume that the motion is in the x-direction and that the environment is compliant in the direction of motion only. Hence, we set $K_{env,y} = 0$.

Furthermore, the arm stiffness is assumed to be the same in both directions, such that $k_x = k_y$.

4.2.7 Admittance Compensator

The compensator used is the one described in chapter 2, expanded to two dimensions, in, x and y. Namely,

$$C(s) = \begin{bmatrix} \dfrac{1}{m_x s^2 + b_x s} & 0 \\ 0 & \dfrac{1}{m_y s^2 + b_y s} \end{bmatrix} \tag{4.14}$$

In contact mode, which is first-order, the inertial terms are set to $m_x = m_y = 0$.

4.2.8 Jacobian

The Jacobian used is the standard tool tip Jacobian for a 2-link manipulator [35]. It converts joint rates into Cartesian velocities in the tool frame. Notice that the Jacobian is greatly influenced by the value of θ_2.

$$^3J = \begin{bmatrix} L_{L1} \sin(\theta_2) & 0 \\ L_{L1} \cos(\theta_2) + L_{L2} & L_{L2} \end{bmatrix} \tag{4.15}$$

4.3 SISO Transfer Function Analysis

From Figure 4.2, the inner loop transfer function is found as:

$$G_\theta = G_p D \left(1 + G_p \left(D + K_e\right)\right)^{-1} \tag{4.16}$$

Adding the outer loop elements, the overall SISO transfer function is then:

$$G_{CL} = G_\theta \left(1 + CK\right)\left(1 + G_\theta CK_{eq}\right)^{-1} \tag{4.17}$$

Where:

$$K_{eq} = K + K_e \qquad (4.18)$$

The 1-DOF model essentially borrows the (1,1) elements from the 2-DOF model described in the previous section. Thus, for the SISO equations below, 'k' will represent the (1,1) element of the matrix 'K', namely, k_x. Likewise, 'b' represents b_x. The other elements are also written in lower case to signify that they are scalar values. This section explains how the shoulder joint input-output stability is analyzed for varying payloads, arm configurations, and environment stiffness. It is an extension of the work done by Smith, who previously characterized the effect of time delay, environment stiffness and bandwidth in the frequency domain.

4.3.1   Procedure for Evaluating 1-DOF Stability

The analysis assumes that the shoulder joint is in a fixed position, at $\theta_1 = 0$. Thus the relative angle between joints depends only on the elbow joint, θ_2.

Using MATLAB, the transfer function is constructed and the polynomial denominator is extracted. Setting the denominator equals to zero yields the characteristic equation, from which the Routh array can be built. The first column of the array is then checked to satisfy the Routh-Hurwitz stability criterion [41]. This criterion states that each sign change of the elements of the first column signifies an unstable pole that lies in the right half of the complex plane. Thus, for all poles to be stable, all elements of the first column of the Routh array must have the same sign.

Expanding the transfer function obtained above:

$$\frac{\left(K_{vs}s + K_{ps}\right)\left(bs + k\right)}{bJ_p s^3 + \left(B_m b + K_{vs}b\right)s^2 + \left[\left(K_{ps} + K_{env,x}\right)B + K_{vs}\left(k + K_{env,x}\right)\right]s + K_{ps}\left(K_{env,x} + k\right)} \quad (4.19)$$

The following Routh table can then be obtained:

$$
\begin{array}{c|cc}
s^3 & bJ_m & b\left(K_{env,x} + K_{ps}\right) + K_{vs}K_{eq} \\[2mm]
s^2 & b\left(B_m + K_{vs}\right) & K_{ps}K_{eq} \\[2mm]
s^1 & b\left(K_{env,x} + K_{ps}\right) + K_{vs}K_{eq} - \dfrac{J_m K_{ps}K_{eq}}{\left(B_m + K_{vs}\right)} & \\[4mm]
s^0 & K_{ps}K_{eq} &
\end{array}
\quad (4.20)
$$

The Routh stability method is convenient for this analysis because it does not require that individual poles actually be calculated. The variable, k, b are kept unknown, while the environment stiffness, K_e, payload mass, m_p, and elbow angle, θ_2, are substituted. Looking at the Routh table above, it is obvious that any choice of positive k, b will make the first, second and fourth elements of the first row positive. Thus, only the third element must be solved to ensure that it is positive. Solving for the third elements yields the following linear relations in k and b:

$$k < \frac{\left(B_m + K_{vs}\right)\left(K_{ps} + K_{env,x}\right)}{J_p K_{ps} - \left(B_m + K_{vs}\right)K_{vs}}b - K_{env,x}, \text{ for } J_p K_{ps} - \left(B_m + K_{vs}\right)K_{vs} > 0$$

$$(4.21)$$

$$k > \frac{\left(B_m + K_{vs}\right)\left(K_{ps} + K_{env,x}\right)}{J_p K_{ps} - \left(B_m + K_{vs}\right)K_{vs}}b - K_{env,x}, \text{ for } J_p K_{ps} - \left(B_m + K_{vs}\right)K_{vs} < 0$$

It is clear that this relation directly or indirectly involves all the variables mentioned earlier, namely K_{env} and J_m. If the first line is plotted, the area beneath it will represent the stiffness and damping required to maintain stability. If the second line is plotted, it is the area above that defines the stable range. The denominator dictates whether the line will slope upward or downward.

for $J_p K_p - (B_m + K_v) K_v > 0$ for $J_p K_p - (B_m + K_v) K_v < 0$
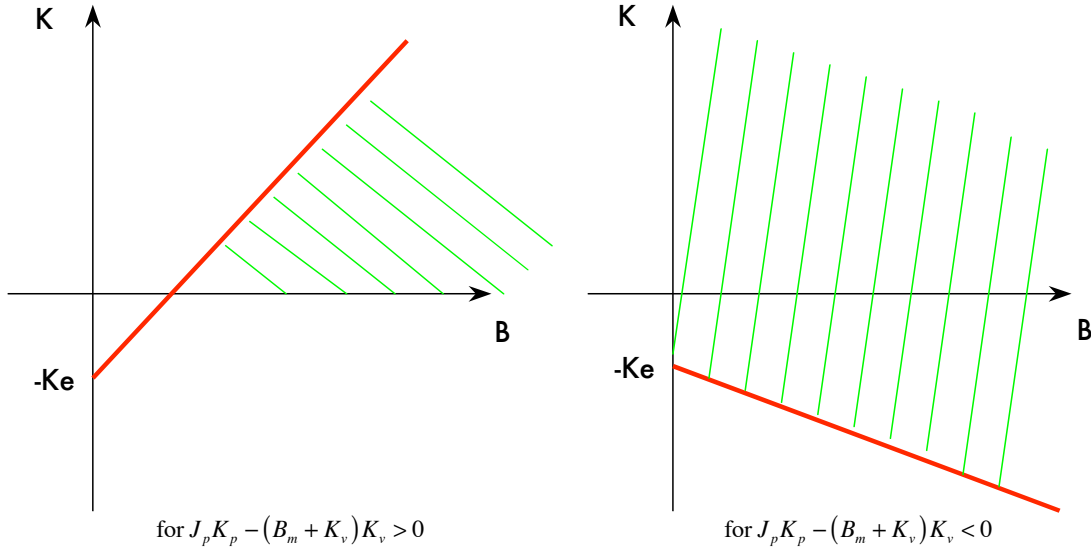
Figure 4.6: Stability Margins for both cases

Evaluating the denominator with the values found earlier, it is determined that the necessary inertia to make the line slope upward is approximately K_v^2/K_p, and for Ranger this is approximately 99 kgm^2. This inertia is would result in a payload that Ranger could not support. Since Ranger's inertia will always be lower than the critical value, the second scenario will always be present. This scenario does not seem very intuitive since it indicates that the manipulator is stable for *any* positive choice of stiffness and damping. However, as experiments would indicate, there is a minimum amount of damping required to stabilize a commanded stiffness.

While this analysis shows very optimistic results, it is important to realize that these assume a quasi-static linear behavior, which is not the case for the general manipulator, as will be shown in testing. It assumes that contact is *always* maintained and that displacements are small. There are also many elements absent from this simplified analysis that could lead to instability in the actual controller. One such

element is time delay. Smith analyzed the effect of time delay on the controller and showed that it increased the necessary target damping for stability. It is assumed that this holds true, and as such this analysis is done with no time delay.

Another important unmodeled parameter is gravity. In general it is assumed that the joint P-D control rejects the added disturbance of gravity. It may be worth noting that if the arm is neutrally buoyant, the effect of gravity is also significantly reduced.

An additional unmodeled nonlinearity is force and saturation. The actuators have a maximum force they are capable of outputting and have certain frequencies that they cannot exceed. The stability analysis assumes that any amount of force can be supplied, infinitesimally fast. However, this is untrue in reality, and can lead to limit cycling. There are extra bands put on allowable torque and velocity within the software that can limit the response of the system. Velocities are computed and filtered digitally, and the force sensor can be noisy, especially due to inertia at the end effector. Above all this, there are unmodeled flexibilities in the drive train and in the links that can prompt instability, especially in an outstretched position. If the natural frequency of the drivetrain is excited, unwanted vibrations can be perpetuated. Lastly, nonlinear friction can play a major role in destabilizing this controller. Most the positions adjustments cross in and out of low velocity, a regime in which it is very difficult to characterize friction and stiction in the harmonic drives, as demonstrated by Guion [29] and Aksman [42].

Despite the host of unmodeled nonlinear effects, it could still be worthwhile to conduct a parametric analysis of the stability, given that the link inertia was high

enough to produce unstable behavior for certain choices of K and B. This is accomplished in the following cases by increasing the payload mass to a sufficient value. In that case, the trends identified in the following section could still be pertinent.

4.3.2 1-DOF Stability for Varying Elbow Angle

The elbow angle plays a role in changing the inertia of the arm. Increasing the elbow angle brings forearm mass closer to the shoulder, thus reducing the inertia and increasing the stability. In Figure 4.7 the elbow angle increases from the outstretched position at $\theta_2 = 15^0$ to a more retracted position at $\theta_2 = 60^0$.
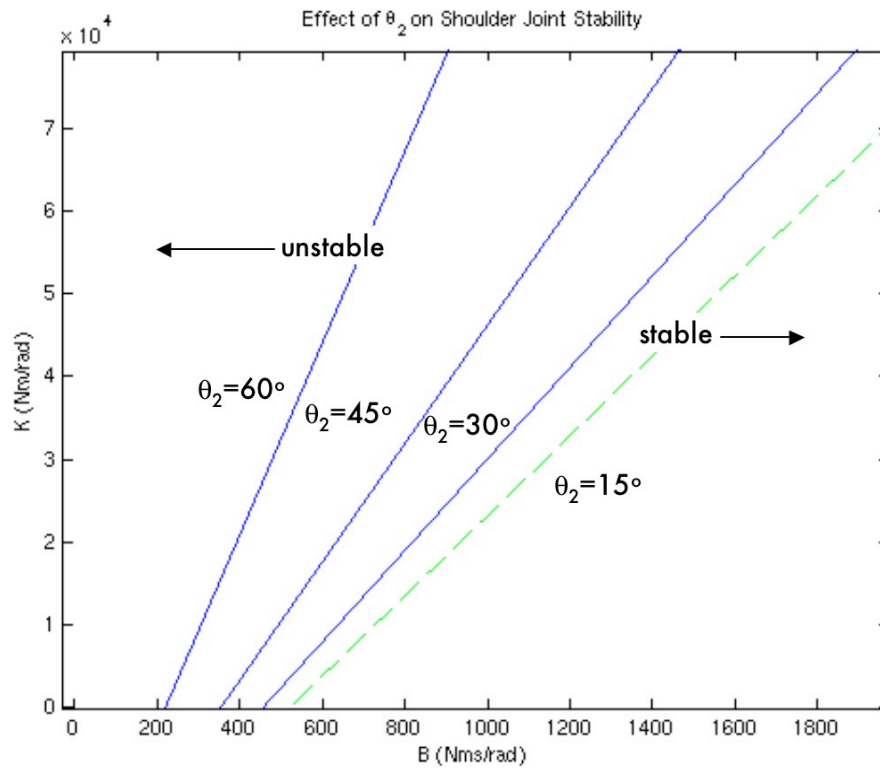
Figure 4.7: Effect of Elbow Angle on Stability. K_{env} = 25000 Nm/rad, m_p = 100 kg

4.3.3 1-DOF Stability for Varying Payload

The added payload also affects the inertia. As shown in equations (4.4) to (4.6), inertia increases with payload. The added inertia requires more damping to stabilize and drives the resonance frequency closer to the control bandwidth.
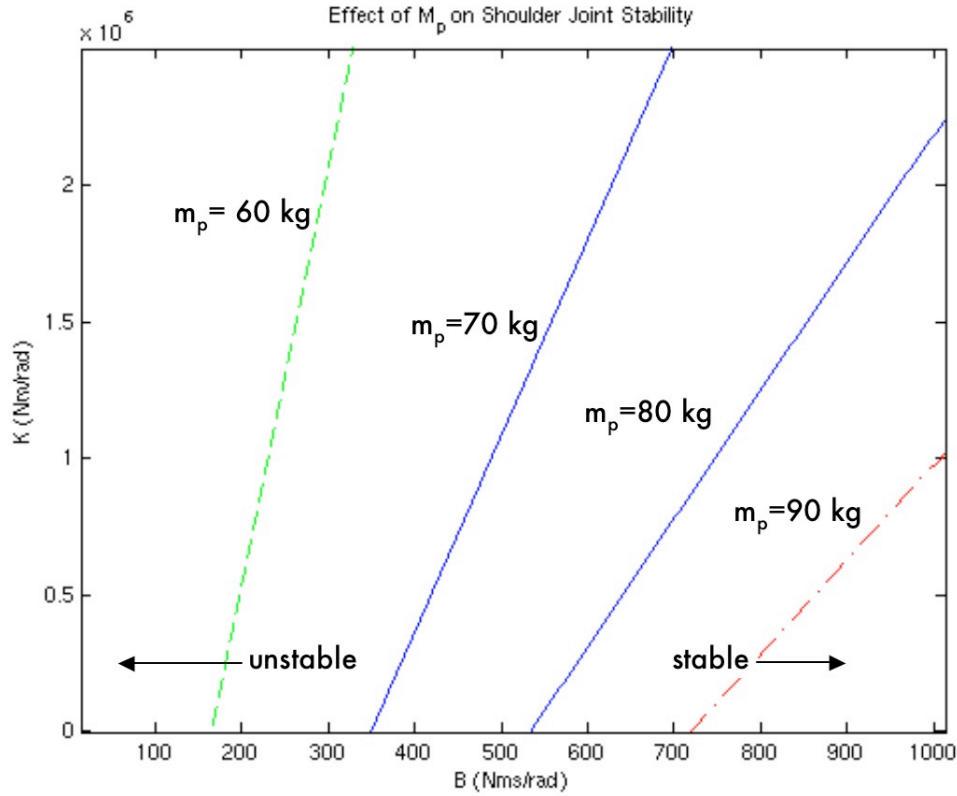
Figure 4.8: Effect of Payload on Shoulder Joint Stability. $K_{env} = 25000$ Nm/rad, $\theta_2 = 60^0$

4.3.4 1-DOF Stability for Varying Environment Stiffness

Analyzing (4.21), we see the slope of the line that separates the region of stability depends heavily on the environment stiffness, as (K_p+K_e) is generally much larger than (B_m+K_v). For all lines of stability, $-K_e$ is also the y-intercept. By increasing the environment stiffness, more damping is required to stabilize the

motion, but also allows high a manipulator stiffness to be specified. This is not necessarily beneficial, as a higher manipulator stiffness will increase the forces with which the manipulator impacts the environment.
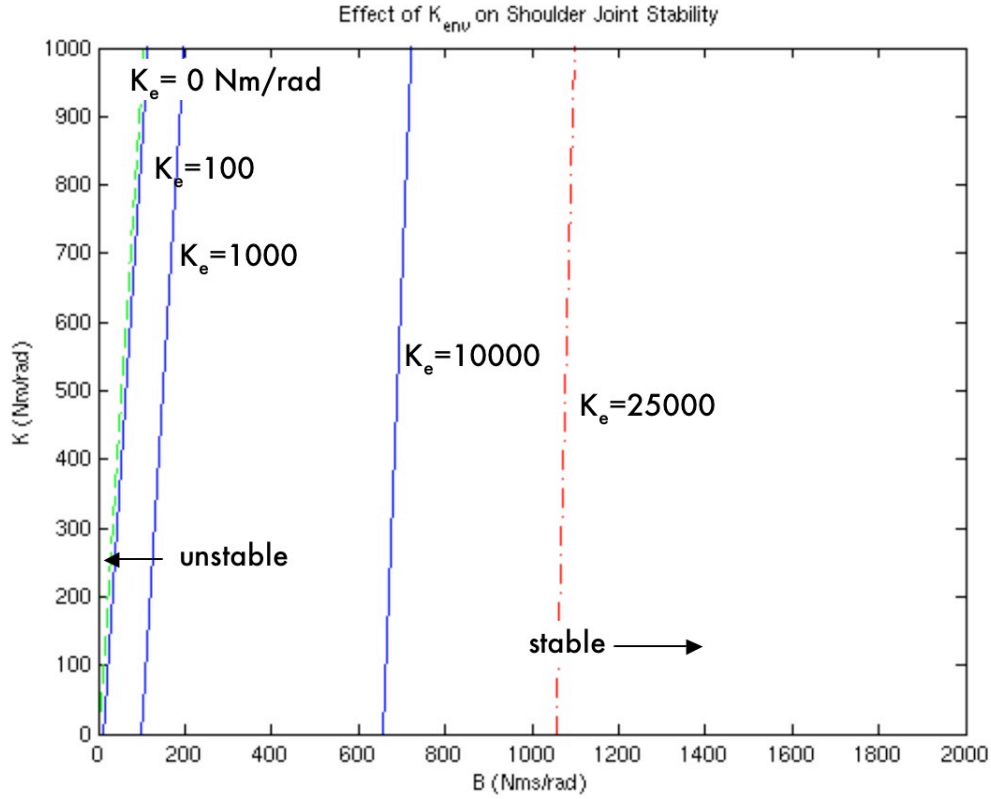
Figure 4.9: Effect of Environment Stiffness on Shoulder Stability. $\theta_2 = 60^0$, $m_p = 200$ kg

4.3.5 1-DOF Stability with Corrective Factor

Adding the corrective factor seen in chapter 2 changes the overall admittance compensator. From (2.34), we can find the equivalent compensator, $C_{cf}(s)$

$$C_{cf}(s) = \frac{C(s) - \frac{c_v}{K_{eq}}}{1 - c_v} = \frac{\frac{1}{b_d s} - \frac{c_v}{K_{eq}}}{1 - c_v} = \frac{K_{eq} - b_d c_v s}{b_d s K_{eq}(1 - c_v)} \qquad (4.22)$$

This once again demonstrates the possibility of an infinite gain, if c_v is chosen

close to 1. For rigid contact, $K_{eq} \gg 1$, and thus, we can approximate:

$$C_{cf}(s) = \frac{1}{b_d s(1-c_v)} - \frac{c_v}{K_{eq}(1-c_v)} \cong \frac{1}{b_d s(1-c_v)} = \frac{C(s)}{(1-c_v)} \qquad (4.23)$$

Hence, the net effect of the corrective factor is a scalar multiplication, which will effectively reduce the damping by a factor of $(1-c_v)^{-1}$. This will further increase the damping required for stability. It appears that the effect of the corrective factor is akin to decreasing the system damping. Implementing this modification to the controller to improve performance is not worthwhile if it compromises stability.
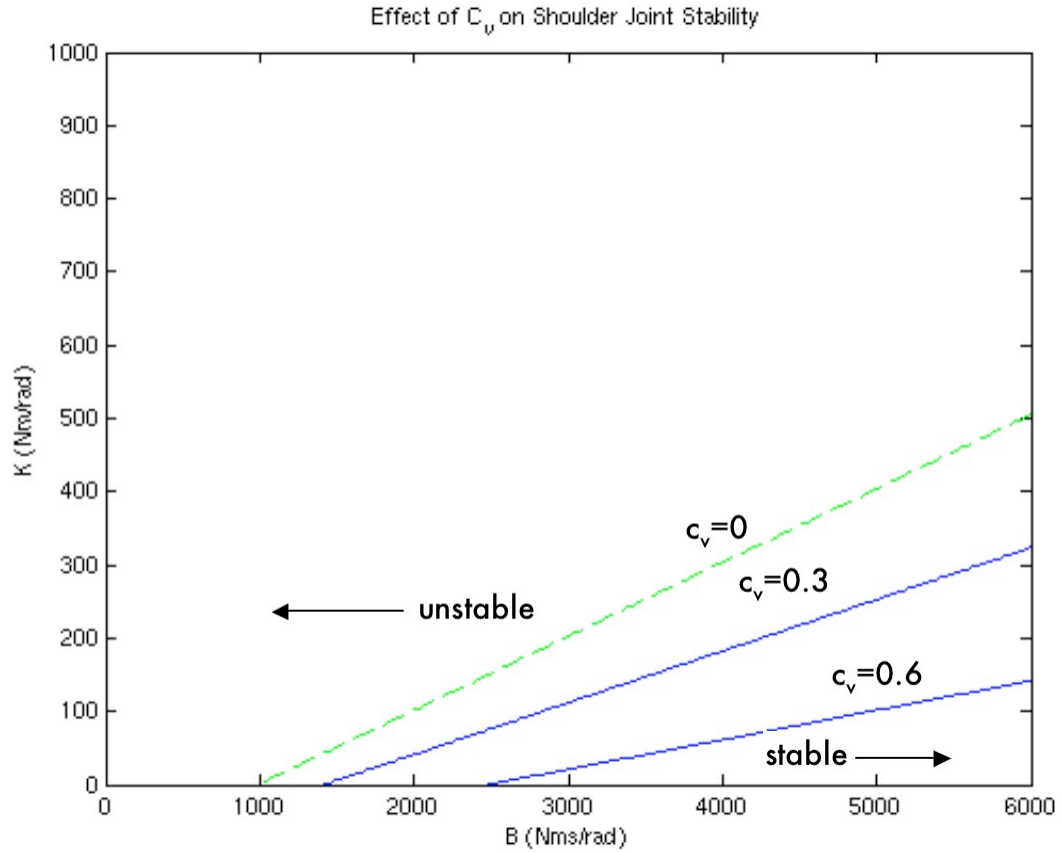
Figure 4.10: Effect of Corrective Factor. K_{env} = 100 Nm/rad , $\theta_2 = 60^0$, m_p = 100 kg

88

4.4 MIMO Generalized Transfer Function Analysis

The transfer function for the MIMO realization differs only by the inclusion of the Jacobian. This simple addition complicates the overall closed loop transfer function, by coupling the force and position conversions. Nevertheless, despite the inclusion of the Jacobian, results indicate that again, the manipulator is stable for all chosen values of K and B. For the sake of continuity from the 1-DOF case, the analysis is carried out for the case where the link inertia is higher than it should be, with the hopes of identifying relevant trends.

In the MIMO case, the inner loop transfer function becomes:

$$G_\theta = G_p D \left(I + G_p \left(D + J^T K_e J \right) \right)^{-1}$$

(4.24)

The overall closed-loop transfer function is then:

$$G_{CL} = J G_\theta J^{-1} \left(I + CK \right) \left(I + J G_\theta J^{-1} C K_{eq} \right)^{-1}$$

(4.25)

Where I is the 2×2 identity matrix.

4.4.1 Procedure for Evaluating 2-DOF Stability

For a completely decoupled system, the closed-loop transfer function of (4.25) would simply be a diagonal matrix, with the diagonal elements having the same transfer function determined in the SISO analysis. Unfortunately the robot's dynamics are coupled through the Jacobian defined in (4.15). It appears as a pre- and post-multiplication on the inner loop in (4.25). However, if we assume that the manipulator only contacts the environment axially (i.e. the x-direction, shown in Figure 4.3), then the analysis can be simplified, as:

$$K_e = \begin{bmatrix} K_{env,x} & 0 \\ 0 & 0 \end{bmatrix}$$ (4.26)

and the inner loop transfer function, G_θ, is diagonal. With this assumption, when G_θ is pre- and post-multiplied by the Jacobian, the (1,1) and (2,2) elements of the closed-loop transfer function matrix to retain the same form as the SISO case, the (1,2) element is zero and the only coupled term is the (2,1) transfer function. Thus, the only new analysis need be performed on the (2,1) element.

Analytical solutions for k vs. b are more difficult and cumbersome to handle in the MIMO implementation. For this reason, the 2-DOF analysis will employ a different technique: Contrary to using the Routh criterion, the poles for discrete combinations of k and b are individually computed numerically via MATLAB. Poles with negative real part are stable and unstable poles have positive real part. The system is considered stable if all the poles are stable. The plots show the stability boundary by separating the area with stable poles (green circles) from the unstable poles (red crosses).

Once the analysis is done however, it becomes clear that the situation is identical to the 1-DOF case, namely that all choices of stiffness and damping result in a stable system. For the sake of demonstrating the trends associated with this analysis, a different manipulator configuration is used, namely the extended Neutral Buoyancy Dexterous Robot (NBDR) version, used to Hubble servicing experiments. This configuration is shown below. Assuming the link extensions add negligible mass, and the only difference is that the links have been extended to be 47 inches (1.2 m) long each.
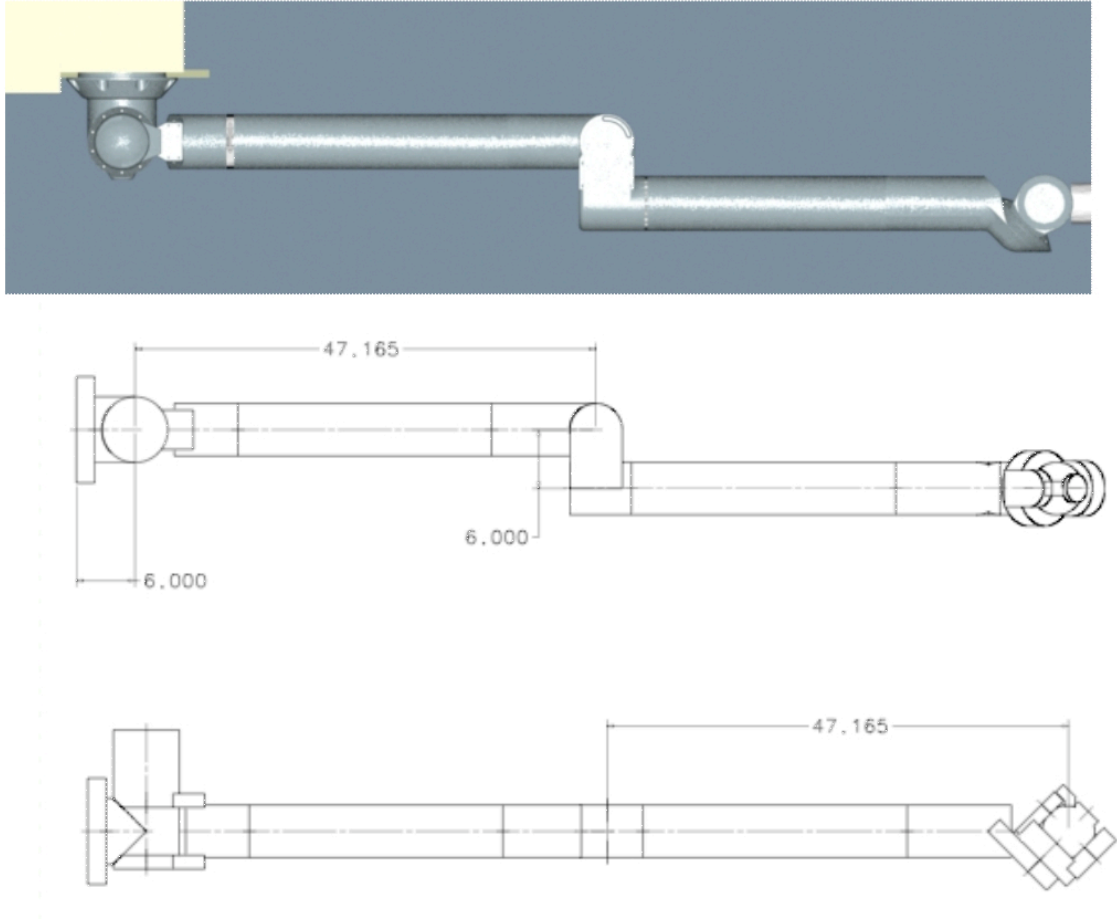
Figure 4.11: Ranger NBDR Configuration

4.4.2   2-DOF Stability for Varying Elbow Angle

As mentioned earlier, a larger elbow angle (in flexion) reduces the arm's inertia and increases the stability. It also helps to avoid the singularity at full extension. The arm becomes highly unstable near singularities because of the increased joint velocity. The inner loop controller already cannot keep up with the rapidly increasing velocities near singularities and the outer loop amplifies this disability, extending this unstable region. We can see how the stable region increases

91

with angle, away from the singularity at zero degrees, but then decreases again as the

angle approaches another singularity at 180 degrees.
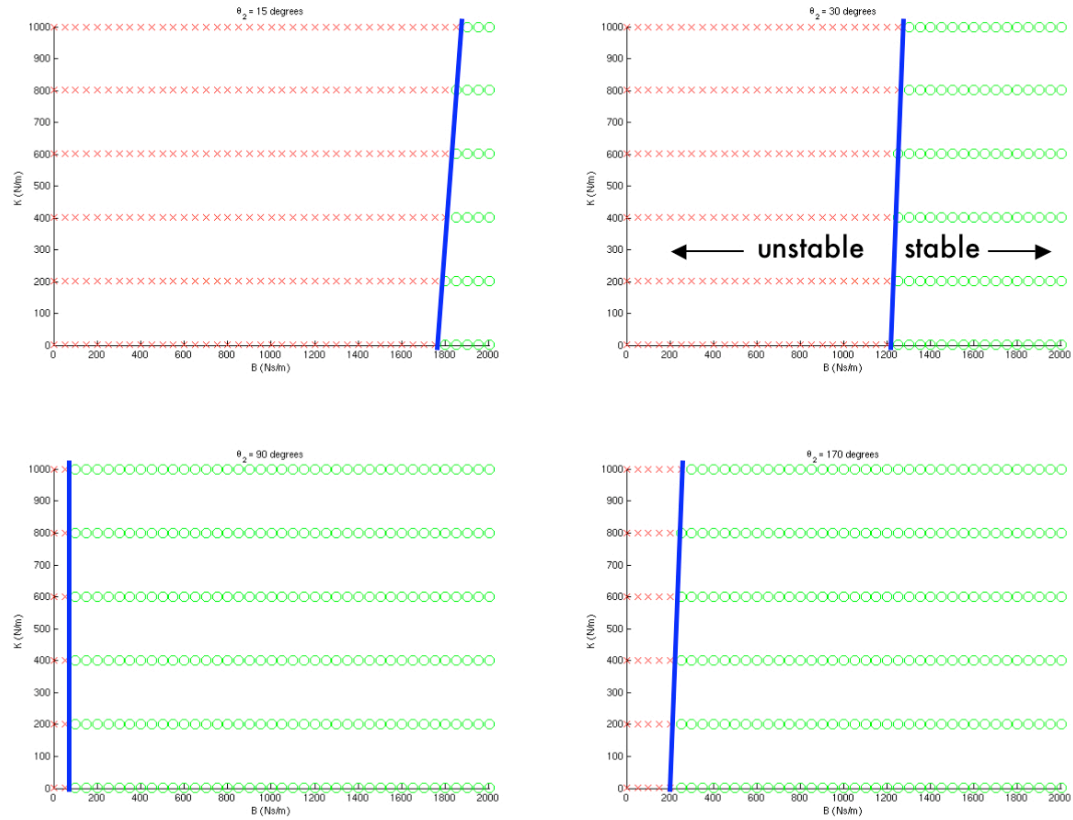
Figure 4.12: Effect of Elbow Angle on Axial Stability. K$_{env}$ = 25000 N/m, m$_p$ = 15 kg

4.4.3 2-DOF Stability for Varying Payload

The effect of increased payload is identical to the 1-DOF case, as shown in

Figure 4.13. Increasing the payload increases the inertia, thus requiring more damping

for stability. The figure illustrates payloads varying from 1 to 20 kg.
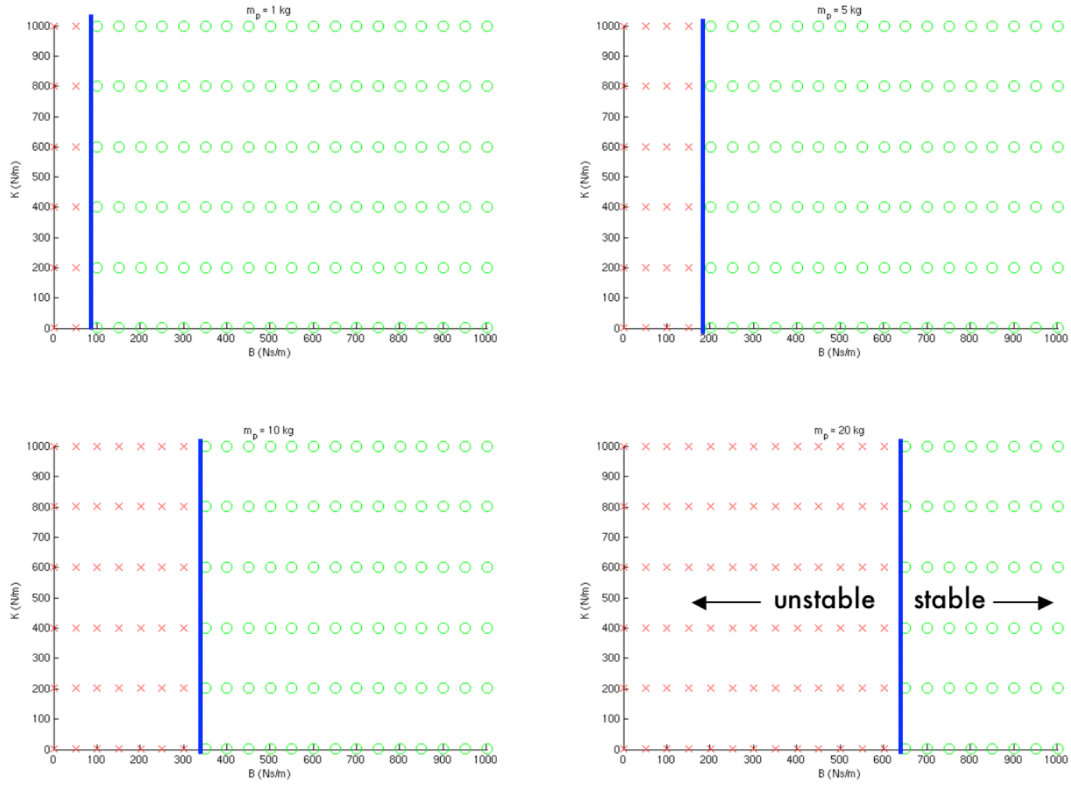
Figure 4.13: Effect of Payload Mass on Axial Stability. K_{env} = 25000 N/m, θ_2 = 60^0

4.4.4 2-DOF Stability for Varying Environment Stiffness

Again, the same behavior as the 1-DOF case is exhibited. High environment stiffness increases the damping necessary for stability with low desired stiffness. As for the 1-DOF case, the slope of the line defining the stability boundary is proportional to the environment stiffness. In the figure, the stiffness is varied from 0 to 25000 N/m.
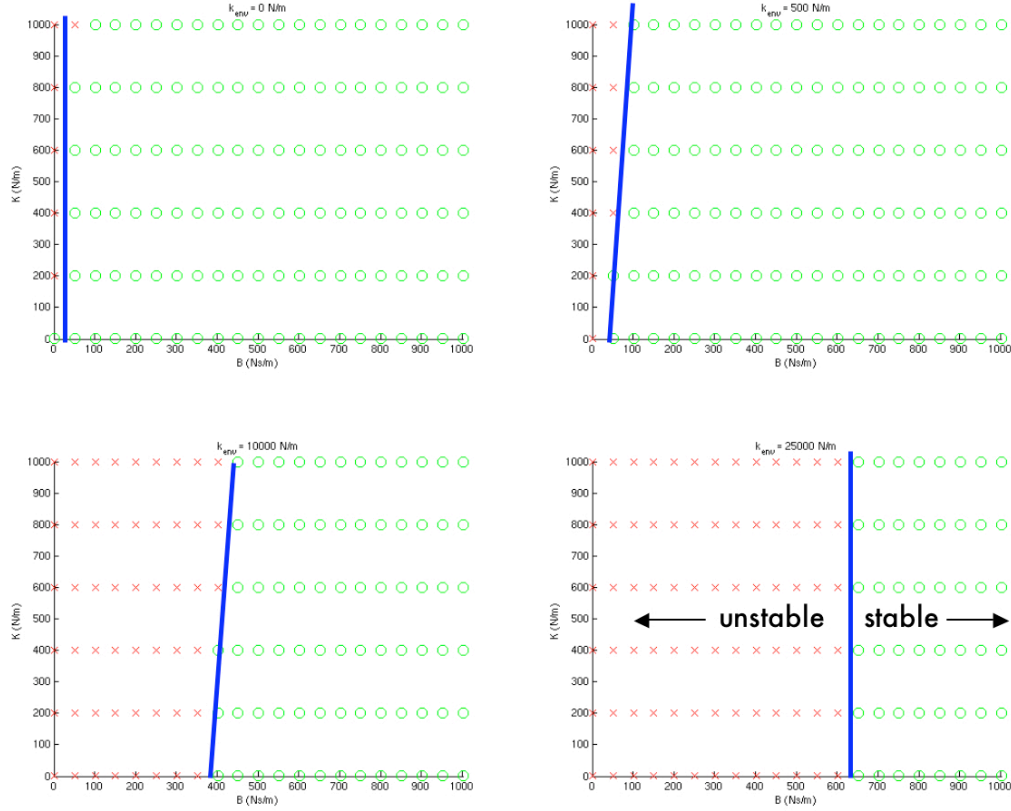
Figure 4.14: Effect of Environment Stiffness on Axial Stability. $\theta_2 = 60^0$, $m_p = 20$ kg

4.5 Bandwidth

The controller model presented in the previous section can be used to determine the bandwidth of the system. Monitoring the bandwidth is important because Smith and Carignan determined that for high link inertia (20 N-m^2), harmonic drive resonance occurred at frequencies on the order of 10 Hz. This low bandwidth is a limiting factor in the choice of gains, as a higher bandwidth controller could excite resonance frequencies, thus destabilizing the system. The effect of arm configuration, payload and environment stiffness can be investigated, just as in the previous stability analysis. In addition, the bandwidth can be contrasted for different

combinations of stiffness and damping.

In general, the larger the inertia, the lower the system bandwidth. This would suggest that increasing the elbow angle would result in a larger bandwidth and likewise for decreasing the payload mass. To verify this suggestion, the bandwidth of the controller is determined for fixed choice of stiffness and damping. The elbow angle/payload mass is then increased and using the closed-loop transfer function described in (4.19), the corresponding bode diagram can be plotted.

Choosing K = 500 Nm/rad, B = 1000 Nms/rad, with zero environment stiffness, zero payload and increasing the elbow angle, we can see that the Bode diagram is pushed right with increasing elbow angle.
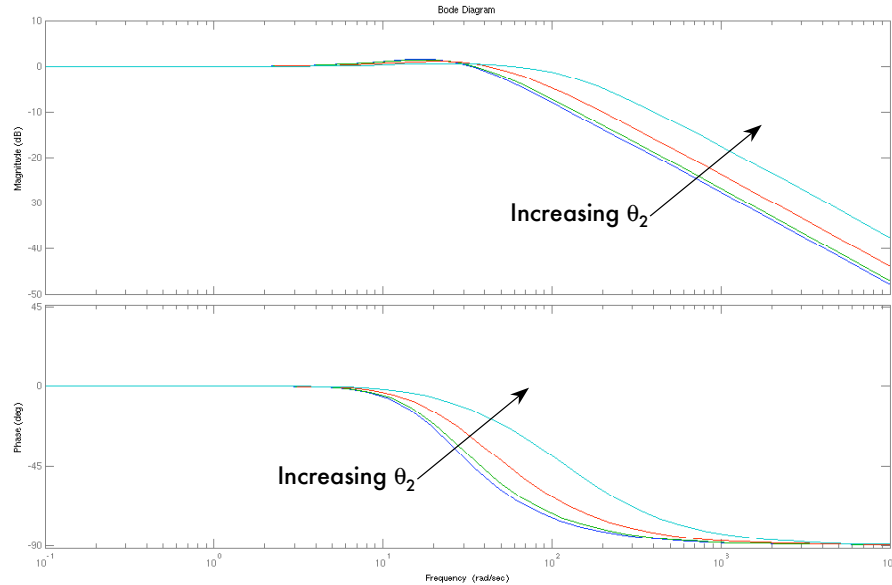
Figure 4.15: Bode Plot for Increasing θ_2

The corresponding bandwidths for the evaluated elbow angles are given in Table 4.2. The experiment can be repeated for increasing payload. Choosing a constant elbow

95

angle of 15 degrees, the resulting Bode plot is shown in Figure 4.16.

Elbow Angle, θ_2 (degrees)	Bandwidth (Hz)
15	8.512
45	9.234
90	12.312
150	23.296

Table 4.2: Bandwidth for Increasing Elbow Angle
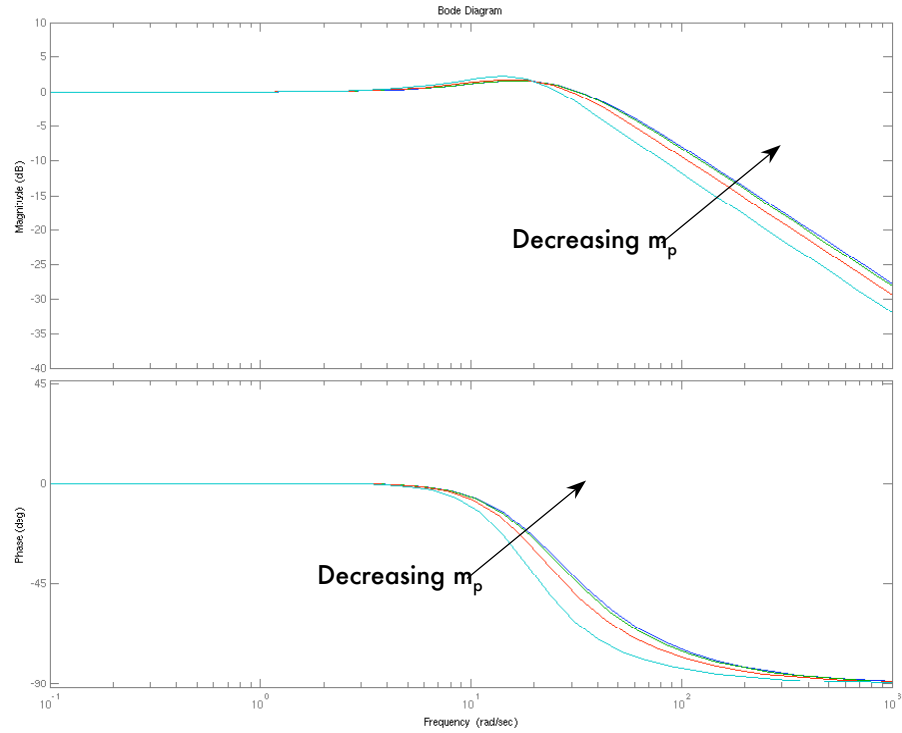
Figure 4.16: Bode Plot for Decreasing m_p

The corresponding bandwidths for the evaluated payload masses are given in Table 4.3.

Payload Mass, m_p (kg)	Bandwidth (Hz)
0	8.512
1	8.259
5	7.400
15	5.954

Table 4.3: Bandwidth for Increasing Payload

Finally the experiment is repeated for increasing environment stiffness. Choosing a constant elbow angle of 15 degrees and zero payload:
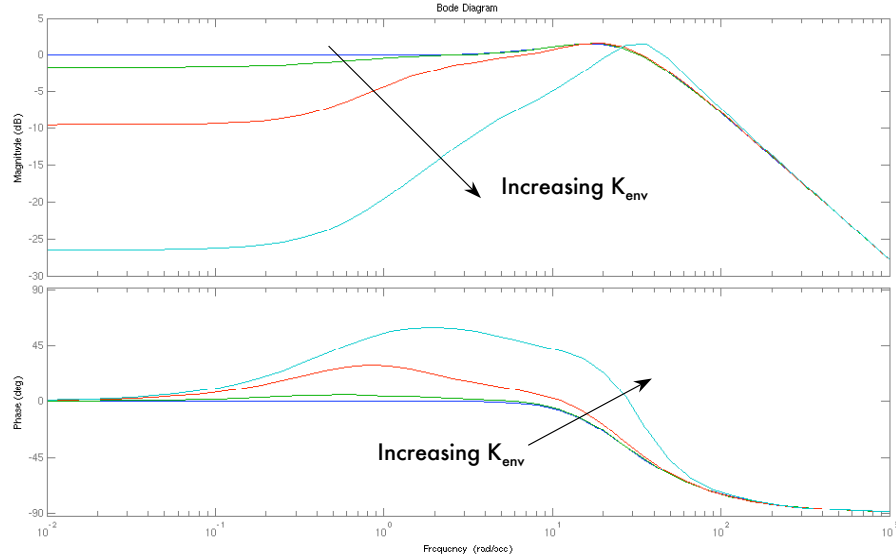
Figure 4.17: Bode Plot for Decreasing K$_{env}$

The corresponding bandwidths for the evaluated environment stiffness are shown in Table 4.4 and indicate that contact with a stiff environment can also push the bandwidth higher.

Environment Stiffness, K$_{env}$ (Nm/rad)	Bandwidth (Hz)
0	8.512
100	10.525
1000	27.524
10000	193.675

Table 4.4: Bandwidth for Increasing Payload

Next, the bandwidth can be found for choice of K and B. With a rigid environment (K$_{env}$ = 10000 Nm/rad), payload mass set to zero, and the elbow angle at 15 degrees, the bandwidth is evaluated for 4 combinations of K and B: Low stiffness/low damping, low stiffness/high damping, high stiffness/low damping, and

high stiffness/high damping. "Low" and "high" values of stiffness correspond to 1 Nm/rad and 500 Nm/rad respectively, while "low" and "high" damping correspond to values of 1 Nms/rad and 1000 Nms/rad respectively. The Bode plots are shown in Figure 4.18 and the corresponding bandwidths are given in Table 4.5.
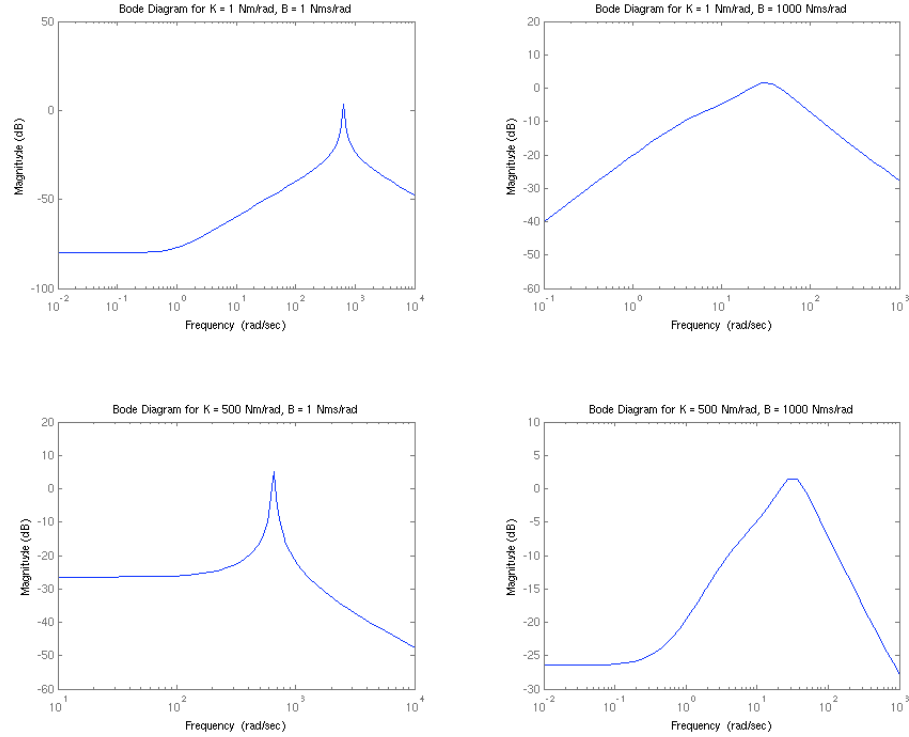
Figure 4.18: Bode Plots for Combinations of Stiffness and Damping (rigid environment)

Desired Stiffness, K (Nm/rad)	Desired Damping, B (Nms/rad)	Bandwidth (Hz)
1	1	92204
1	1000	92204
500	1	247
500	1000	194

Table 4.5: Bandwidth for Various Stiffness and Damping with Rigid Environment

The scenario for low environment stiffness can also be repeated. Here K_{env} is set to 1 Nm/rad, and results are shown in Figure 4.19 and Table 4.6.
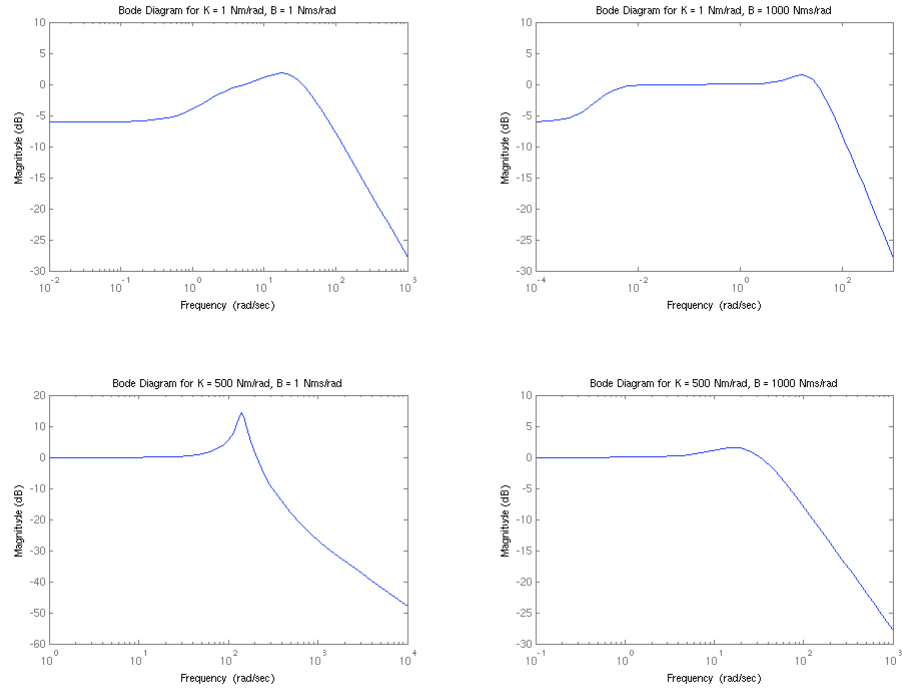
Figure 4.19: Bode Plots for Combinations of Stiffness and Damping (soft environment)

Desired Stiffness, K (Nm/rad)	Desired Damping, B (Nms/rad)	Bandwidth (Hz)
1	1	18.217
1	1000	18.103
500	1	36.275
500	1000	8.533

Table 4.6: Bandwidth for Various Stiffness and Damping with Rigid Environment

Thus, when in contact with a rigid environment, the controller is inherently limited by its inability to administer low desired stiffness without copious amounts of damping. Recalling that the admittance controller commands velocities from forces, and inverting equation (2.15) we see that:

$$Z^{-1}(s) \approx \left(\frac{C^{-1}(s)}{s} + \frac{K}{s} \right)^{-1} = \left(\frac{s}{B_d s + K_d} \right) \qquad (4.27)$$

Thus, for low values of stiffness/damping, the admittance gain is high,

99

increasing the controller bandwidth. If this bandwidth excites resonances in the robots links or drive trains, instability results. Thus, for this admittance controller, care must be taken to ensure that sufficient damping is specified when low stiffness is warranted.

4.6 Summary of Stability Boundaries

Similar trends were observed in both the single joint and multi-DOF case, which is to be expected. In general, it is not the stiffness that dictates stability, but the damping. While a higher stiffness would produce a more accurate response, it can be destabilizing without sufficient damping. While positional accuracy is important, it is essential that the manipulator behave smoothly in contact.

An arm configuration with larger elbow angle tends to provide more stability. This is due to decreased inertia, but also because it is located further from the singular configuration at $\theta_2 = 0^0$. However, if the elbow angle is increased too much, it approaches the singularity at $\theta_2 = 180^0$, also leading to instability. Notwithstanding, increasing elbow angle also increased the system bandwidth, which could potentially excite resonances. Increased payload was shown to negatively affect stability, while higher environment stiffness increased the amount of damping required to achieve low manipulator stiffness. The analysis has also shown that the possible advantages to using a corrective factor are negated by its inferior stability properties.

It may be interesting to investigate the ability of other perhaps more complex compensators to stabilize the controller for pertinent regions. The stiffness-damping model is an intuitive one, but a higher order compensator could conceivably achieve

better stability or performance. These other controllers could provide a better tradeoff. For instance, for small interaction forces in rigid contact, low manipulator stiffness is desired. Stability with higher manipulator stiffness would gladly be sacrificed if a lower stiffness could be achieved more stably. A controller that could schedule gains according to interaction forces could be very useful, or better yet, an adaptive controller.

An important consideration to remember is that this stability analysis is only loosely related to manipulator performance in contact, and provides no insight into what manipulator stiffness and damping gains are suitable for a given task. Specifically, there is no information regarding the magnitude of interaction force that is required for stable contact. Ideally, this force should be minimized. However, to determine the gains that will achieve this objective, actual contact testing is required.

Chapter 5

Results

5.1 Simulation

The stability analysis presented in Chapter 4 was limited due to the inability to model some of the plant nonlinearities. Two of those nonlinearities are force saturation and the intermittence of contact due to the manipulator being commanded away from the impact surface. The effect of these could be verified using a simulation of the plant, and setting up a model of the environment that it makes contact with. A 1-DOF simulation of the controller was thus implemented in Simulink™ to evaluate if the desired response would be achieved and validate the findings of the previous chapter. Since the results of the stability analysis were not entirely helpful for implementing the controller, a simulation could shed more insight into its behavior during contact.

A continuous-time simulation was set up with the identical model described in Chapter 4. The arm configuration, payload mass and environment stiffness could also be varied. The arm is made to follow a trajectory consisting of a very small rotation about the shoulder joint. It is commanded to a rotation angle of 0.1 radians, and a "wall" of prescribed stiffness interferes with its path at 0.05 radians.
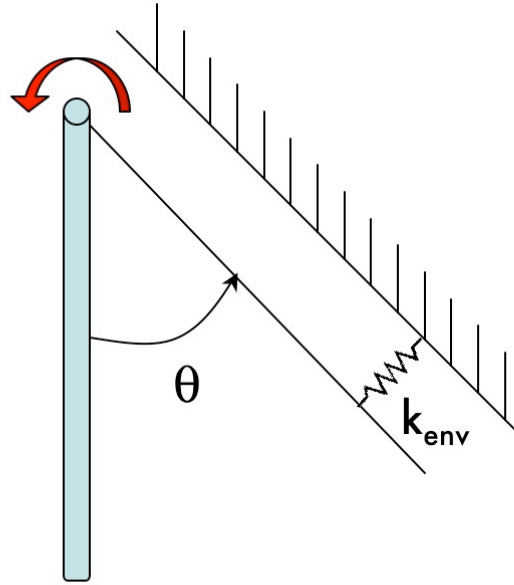
Figure 5.1: Simulated Environment
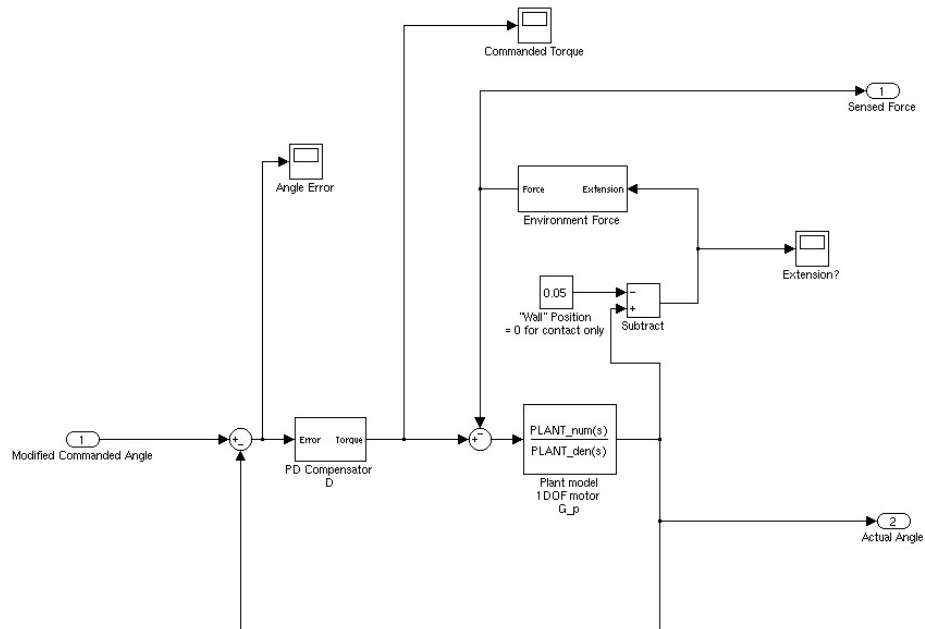
Figure 5.2: Simulink^{TM} Inner Loop Model
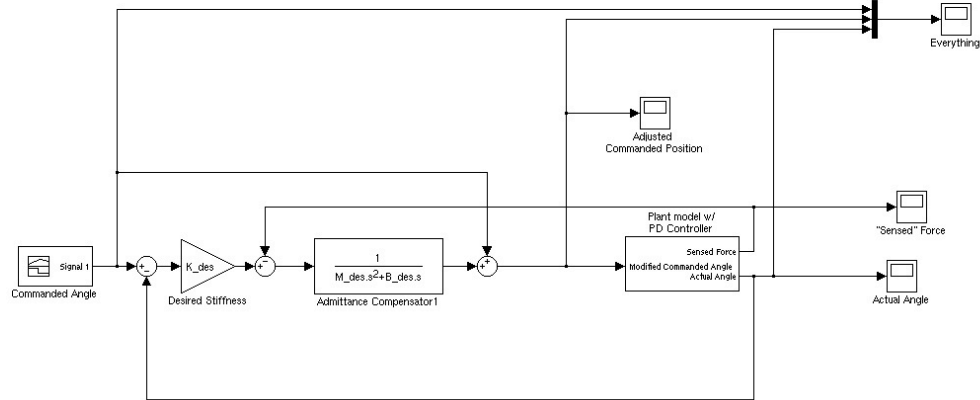
Figure 5.3: Simulink^{TM} Outer Loop Model

To determine how the manipulator would behave in contact with different surfaces, two values of environment stiffness are considered: compliant (250 Nm/rad), and rigid (25000 Nm/rad). For each of these environments, the controller response will be plotted for different combinations of desired manipulator stiffness and damping. The stiffnesses used are 5 Nm/rad, and 500 Nm/rad while the damping used are either 1 Nms/rad or 1000 Nms/rad. The simulation should illustrate the effects of choosing a damping value that is too high to too low for a given stiffness. For the simulation the manipulator configuration consists of the elbow angle at 60 degrees, with zero payload mass.

5.1.1 Compliant Environment

For a compliant environment, interaction forces should already be low because the contact is more forgiving. Specifying high manipulator stiffness and damping, the following response is obtained:

Figure 5.4: High K, High B Response with Compliant Environment (K_{env} = 250 Nm/rad)

Contact forces begin to increase as soon as contact is made. Since the surface is compliant, the manipulator continues to push into the wall, causing stiffness forces to increase. Damping forces are also produced due to the velocity being attenuated. These damping forces cease after the manipulator stops advancing, and equilibrium is reached at about 3 cm of compression. There are slight perturbations in the commanded force at the onset and offset of contact due to the abrupt transition. Regardless, the response is stable, although the compression is not necessarily desirable for more delicate tasks. Decreasing the desired stiffness can minimize this problem, as shown in Figure 5.5.

Figure 5.5: Low K, High B Response with Compliant Environment

105

With low manipulator stiffness, the equilibrium is achieved closer to the wall location. Contact forces are also significantly lower, as they are proportional to the position error, which is reduced. However, the contact forces due to the error velocity remain. In addition there position errors associated with using high damping and low stiffness because the manipulator takes too long to return to its commanded position. Low stiffness and high damping thus result in a sluggish response that can be detrimental when positional accuracy is essential.

Choosing a small stiffness and damping can reduce forces overall. This is illustrated in Figure 5.6.
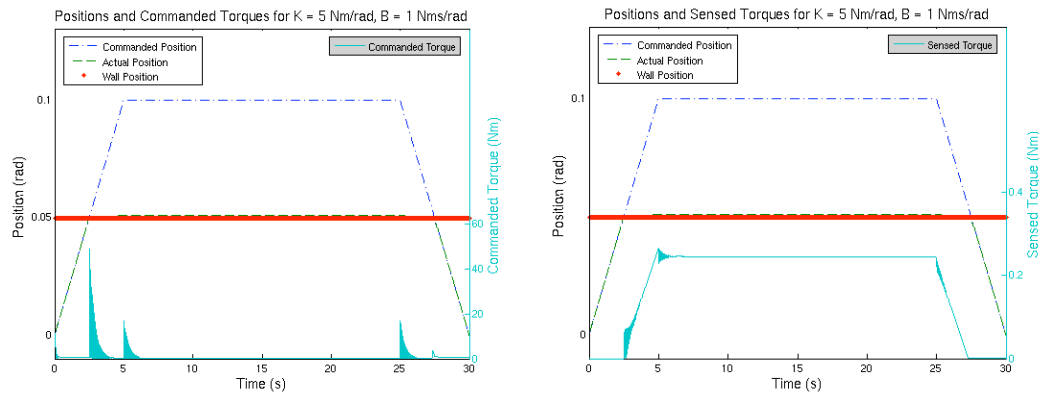
Figure 5.6: Low K, Low B Response with Compliant Environment

In this case, sensed contact forces are low, position tracking is good, but requires relatively high commanded torque with fast switching when contact is made and released. This high frequency switching might not be attainable by a real motor and could lead to instability. Using a higher value of damping could be beneficial as was illustrated in Figure 5.5. The tradeoff in this scenario is less force switching, but higher forces due to the velocity error, as well as positional inaccuracies. A compromise could be achieved by decreasing the damping to 20 Nms/rad, as in

106
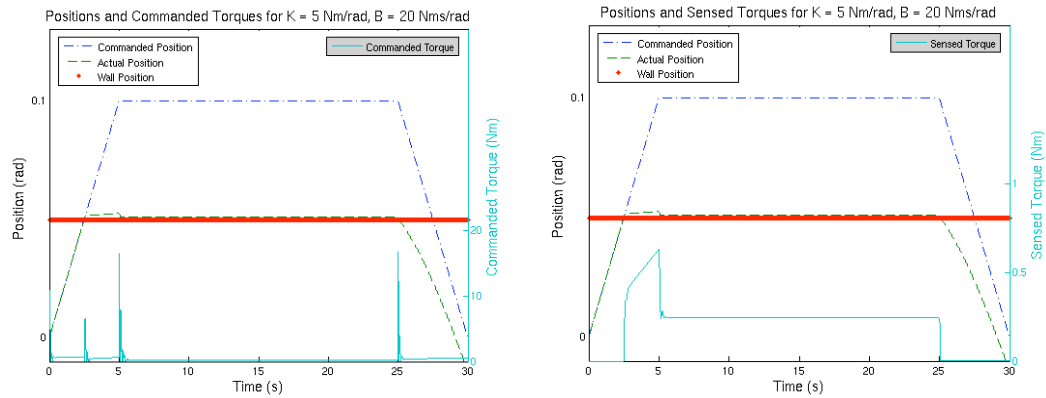
Figure 5.7.

Figure 5.7: Low K, Higher B Response with Compliant Environment

The plots illustrate lower sensed forces, lower commanded forces and satisfactory position tracking. It is important to decrease the magnitude and frequency of position adjustments, as these can lead to instability, especially with a rigid environment that is not very forgiving to contact.

5.1.2 Rigid Environment

Interaction forces with a rigid environment are expected to be higher. A high manipulator stiffness is thus undesirable, which is in accordance with Spong's duality principle from Chapter 2. The response with high stiffness and low damping is shown in Figure 5.8.
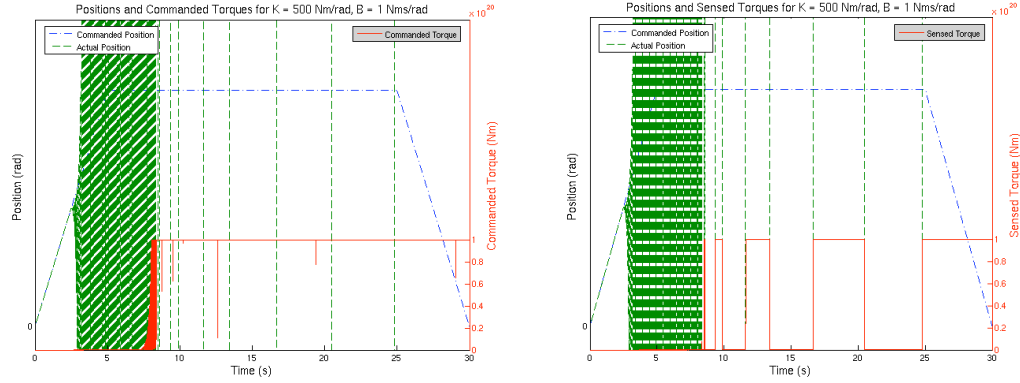
Figure 5.8: High K, Low B Response with Rigid Environment (K$_{env}$ = 25000Nm/rad)

Completely undesirable behavior occurs, where absurdly high joint torques are commanded and sensed, and the position response is extremely unstable. A real manipulator motor would not be capable of handling this load. More damping can be used to stabilize the response, as shown in Figure 5.9.
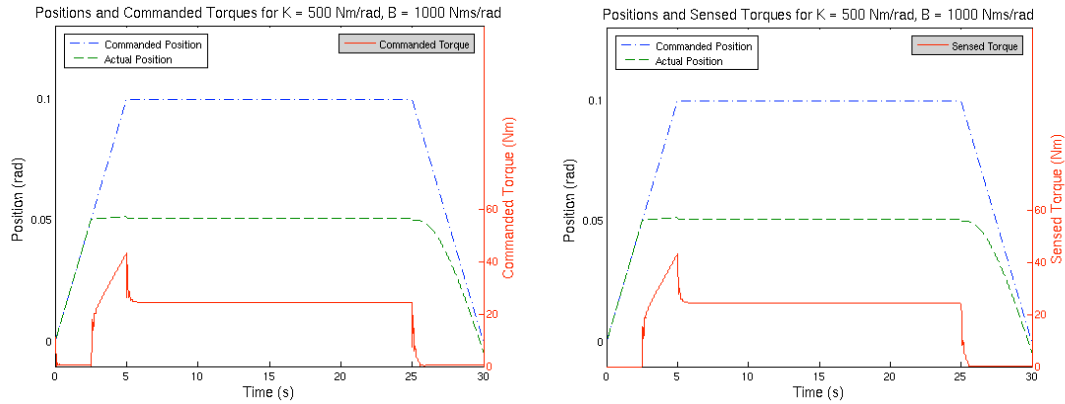
Figure 5.9: High K, High B Response with Rigid Environment

The behavior is much more acceptable, since it is stable. Observe that for the rigid environment, the wall is not compressed, and the output position cannot move past 0.05 rad. Otherwise, the behavior is similar to the compliant surface. There is a component of force due to damping which ceases with velocity, and a leftover component from the stiffness. The contact forces encountered are still relatively high

but can be reduced by decreasing the desired stiffness. The consequent response is shown in Figure 5.10.
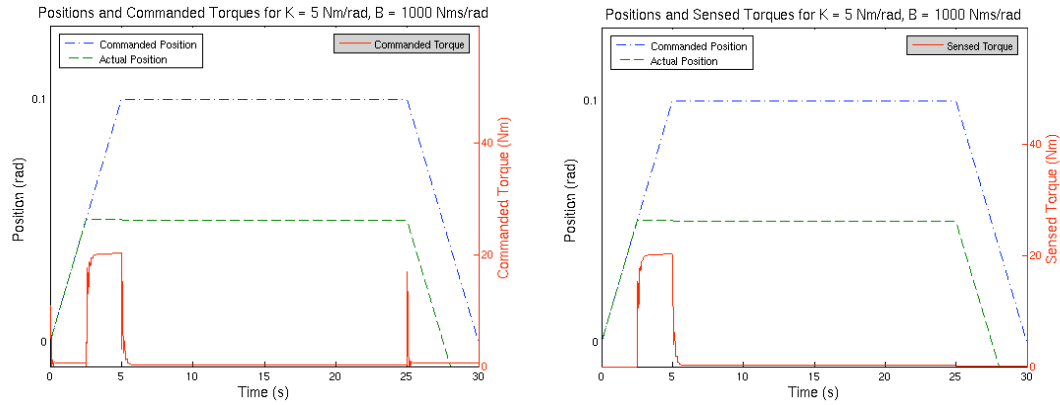
Figure 5.10: Low K, High B Response with Rigid Environment

Forces during sustained contact are significantly lower in this case. Damping forces during motion still remain, and the positional inaccuracy is apparent again. A better compromise could be achieved by reducing the damping, although Figure 5.11 depicts what could happen if the damping is too low with a rigid environment.
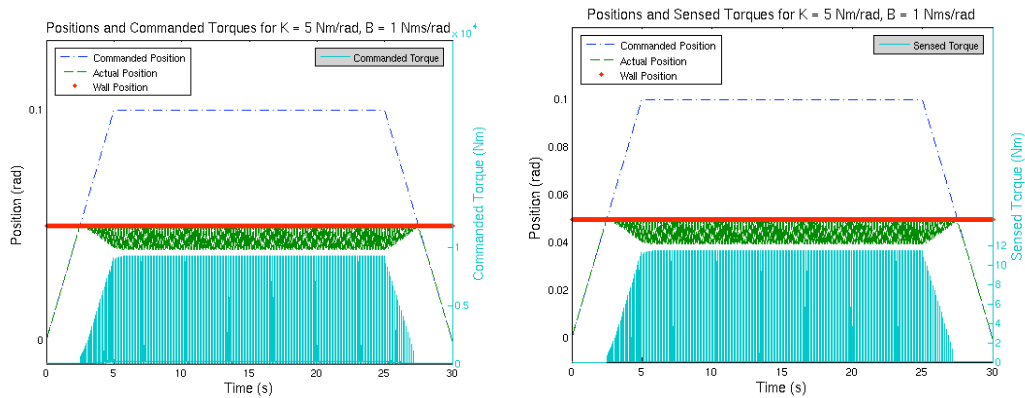
Figure 5.11: Low K, Low B Response with Rigid Environment

When damping is too low, the manipulator begins to oscillate about the contact point. Although the motion is bounded, a closer look at the forces necessary to maintain this motion reveals that joint torques are extremely elevated and would

109

likely saturate a real motor.

5.1.3   Time Delay

A time delay was added to the model to determine its effect. A delay of 10 ms was tested, as it was slightly more than one period of the control loop (which runs at 125 Hz). The time delay definitely affected the stability of the system with low damping, but hardly any difference is noticed when sufficient damping is used. This reconfirms Smith's results that increased time delay increases the damping required for stability.
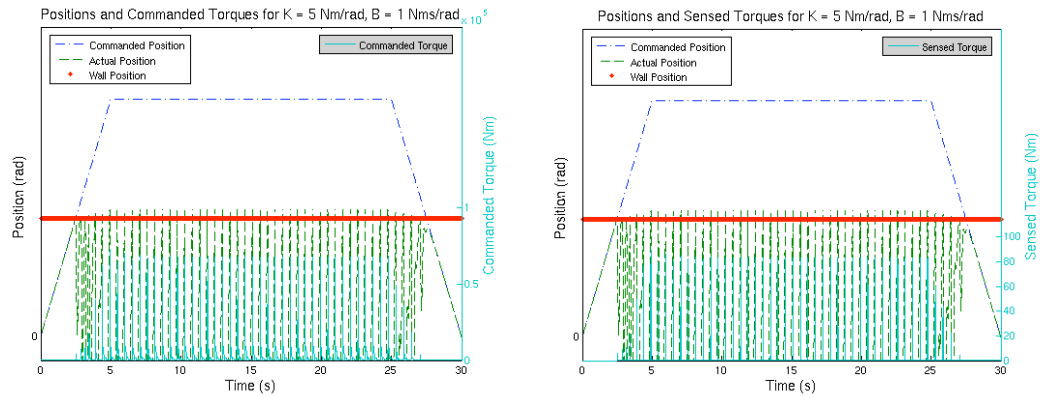
Figure 5.12: Response with Rigid Environment and Time Delay

5.1.4   Force Saturation

The simulation is useful because the effect of force saturation can be studied. Ranger's shoulder joint motor has a maximum torque of 163 Nm. Including this threshold in the simulation yields the following results, using the same parameters as those in Figure 5.11.
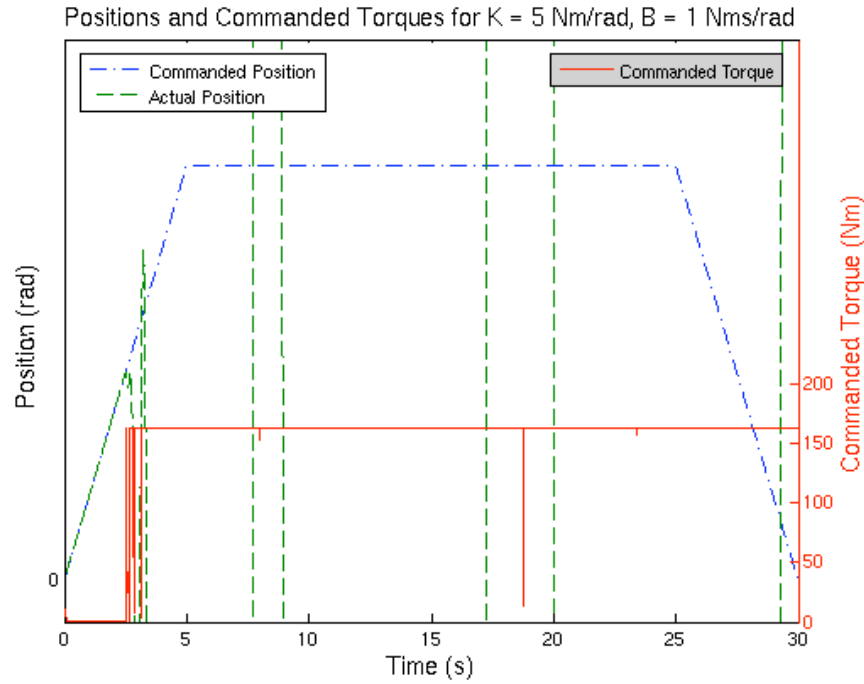
Figure 5.13: Response with Rigid Environment and Torque Saturation

The response becomes highly unstable because the motor cannot supply enough torque to quickly track the modified position command. The manipulator keeps bouncing off the environment at full force, which is another undesirable behavior.

It should be noted that rigid contact simulations are not easily solved and the output of the simulation depends heavily on the solution method used. In all the above simulations, the default variable-step Runge-Kutta integration method (ode45) was used. There are methods more adept at solving stiff problems and these were attempted, with some giving similar results (with variations in the magnitude/period of oscillation) and some giving wildly unintuitive results. Thus, it should be stated

that the results shown above merely identify behavioral trends one could expect from the system and should not be interpreted as being an accurate prediction of actual behavior in rigid contact. More detailed analysis into rigid contact simulation with this controller would certainly be of value.

Despite its limitations in rigid contact, the simulation has provides useful insight into the expected response of the manipulator in one direction of contact. It has shown the negative effects of choosing inappropriate manipulator admittance and that appropriate gains may vary for different environments. Proper gain selection is a matter of tuning for the given environment parameters. Similar behavior should be observed in actual contact testing with Ranger.

5.2 Ranger 1-D Test Results

Contact stability is investigated in one direction, as outlined in Chapter 3. The starting position for the manipulator has the shoulder roll (joint 1) at roughly 90 degrees and the elbow pitch (joint 4) at 90 degrees. The bulk forward motion of the manipulator involves small rotations at both of those joints, and only insignificant adjustments at the other positional joints (2 and 3, namely shoulder pitch and elbow roll respectively). At this stage, Ranger is only capable of running the admittance controller under resolved rate control, and not during a Cartesian trajectory. Thus, the "paths" are specified manually, with constant velocity motions along a Cartesian direction. These are specified in the Cartesian rate graphical user interface (GUI) window of Ranger's control station, shown in Figure 5.14. In 1-D, the manipulator is brought into contact with the environment at a constant forward velocity, which is

maintained for a short while after contact is made. The velocity is then reversed and

the manipulator pulls away. This is sufficient to demonstrate compliance because for

a constant forward velocity, response will be identical. Desired stiffness and damping

are set via the admittance control GUI on Ranger's control station. The admittance

parameters can be specified in any direction, as shown in Figure 5.14. To determine

the stable range, the manipulator stiffness is decreased until slight instability occurs.

It would be infinitely time consuming to experimentally determine the entire range of

stable gains and out of the scope of this research. It is more appropriate to identify

stable manipulator gains that satisfy a goal. For delicate manipulator tasks, this goal is

to minimize the interaction force between the manipulator and the environment. The

desired stiffness dictates the interaction force at steady-state, and thus the objective is

to determine which values of damping that allow stable contact with manipulator

stiffness set as close to zero as possible. The effect of different approach velocities is

investigated.
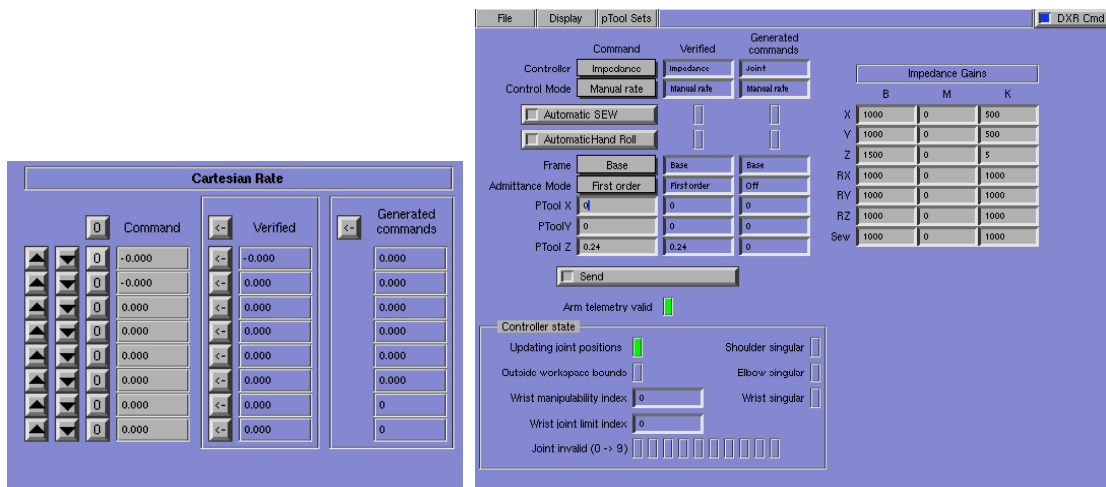
Figure 5.14: Cartesian Rate (left) and Admittance Control (right) GUI Window

5.2.1 Springboard

With a compliant surface, behavior should be similar to the simulated cases. According to Spong's duality principle this capacitive/resistive environment is best contacted with an inertial manipulator, but can accommodate capacitive/resistive impedances as well. Due to the compliance, lower values of damping should still produce stable behavior, and higher manipulator stiffness can also be specified, with less impact force on the surface. For the following cases the manipulator stiffness chosen to be less than the springboard stiffness (of 7.52 kN/m). This is done to minimize compression, since there are only 2 cm of travel until the springs bottom out. The first case shown in Figure 5.15 illustrates the response with a stiffness of 500 N/m can be stabilized with damping at or above 500 Ns/m. The plot indicates behavior similar to that seen in the simulation, with damping forces of approximately 5 N, proportional to velocity when moving at 0.01 m/s, and stiffness forces increasing at 5 N/cm, proportionally to the position error, as expected. The plot also demonstrates how noisy the force measurements can be, especially at the contact transition. Discontinuous variations when no load is applied come from the force deadbanding, which is set at 1 N.

The stiffness is then decreased to 100 N/m, and the damping was raised to 1000 Ns/m for stability. Approach velocities of 1 cm/s, and 2 cm/s were then investigated, with the results shown in Figures 5.16-5.17. These cases illustrate behavior inherent to being at the limit of stability. There is a small chatter at 1 cm/s, made apparent by the variations in force at 9 and 12 seconds. The chatter is much

more visible at 2 cm/s between 5 and 9 seconds where there is a very high variation in contact force.
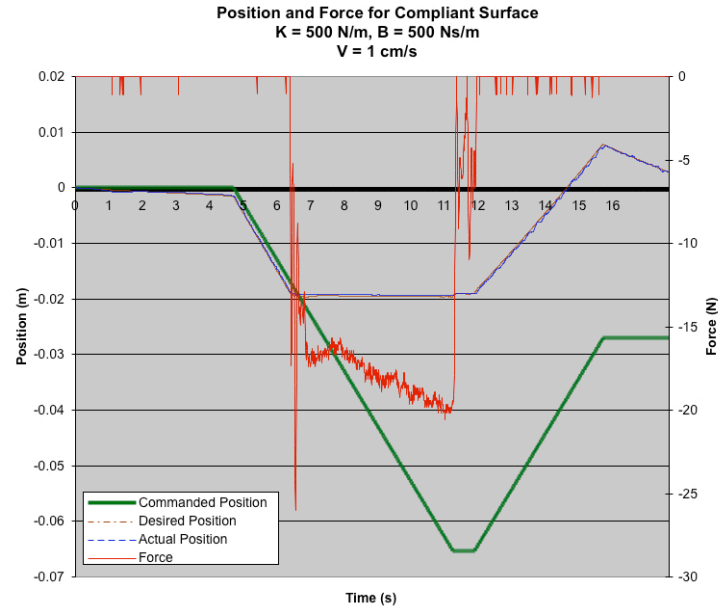
Figure 5.15: Response for K = 500 N/m, B = 500 Ns/m on Compliant Surface
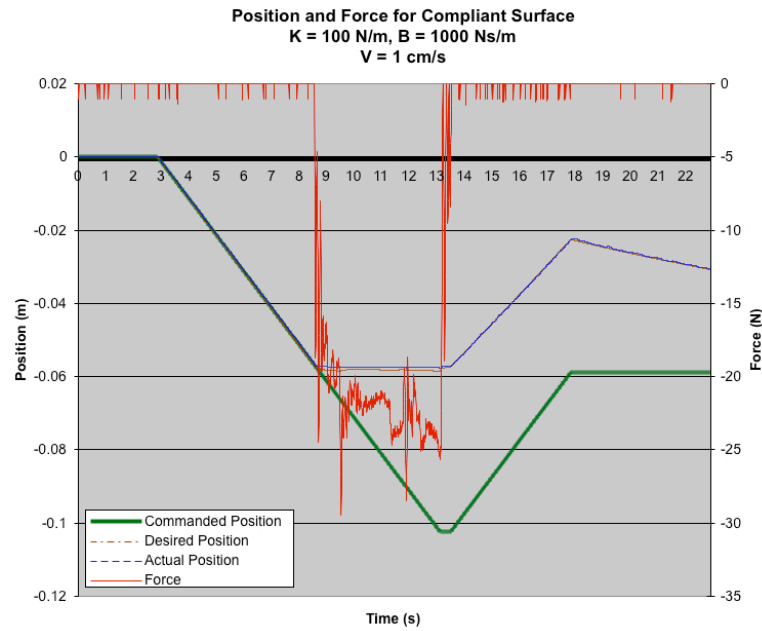
Figure 5.16: Response for K = 100 N/m, B = 1000 Ns/m, V = 1 cm/s on Compliant Surface
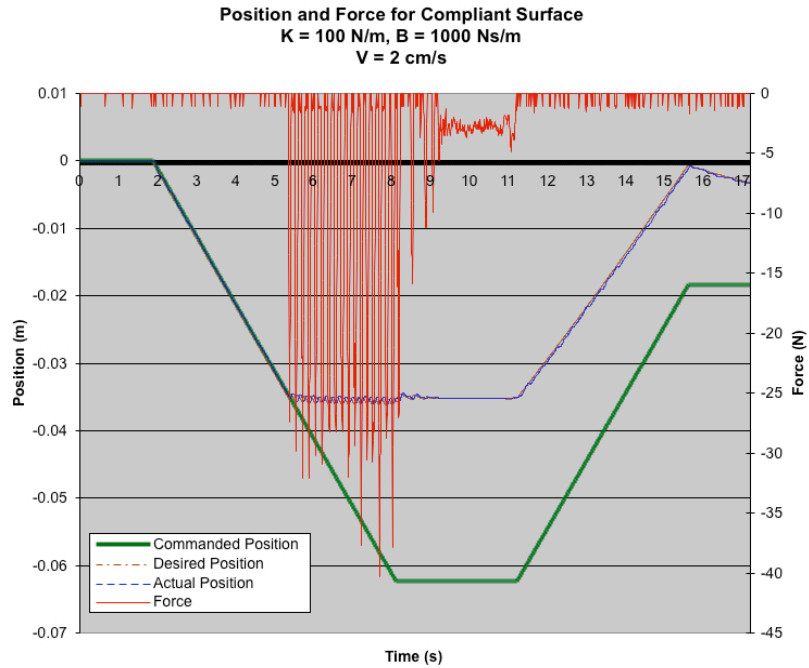
Figure 5.17: Response for K = 100 N/m, B = 1000 Ns/m, V = 2 cm/s on Compliant Surface

To minimize steady-state force, the stiffness is reduced again, to 50 N/m and then to 5 N/m in Figures 5.18 and 5.19 respectively. To cope with instability, the damping is raised to 1500 Ns/m. It is obvious that the higher damping value causes high transient forces due to velocity error, which is especially apparent in Figure 5.18 where the manipulator moves at 2 cm/s, causing the forces to exceed 30 N. Another undesirable effect is the large position error present at the end of the run. When unloaded at a small stiffness and high damping, the manipulator will sluggishly creep back to its commanded position. This can be problematic where accurate positioning is paramount.
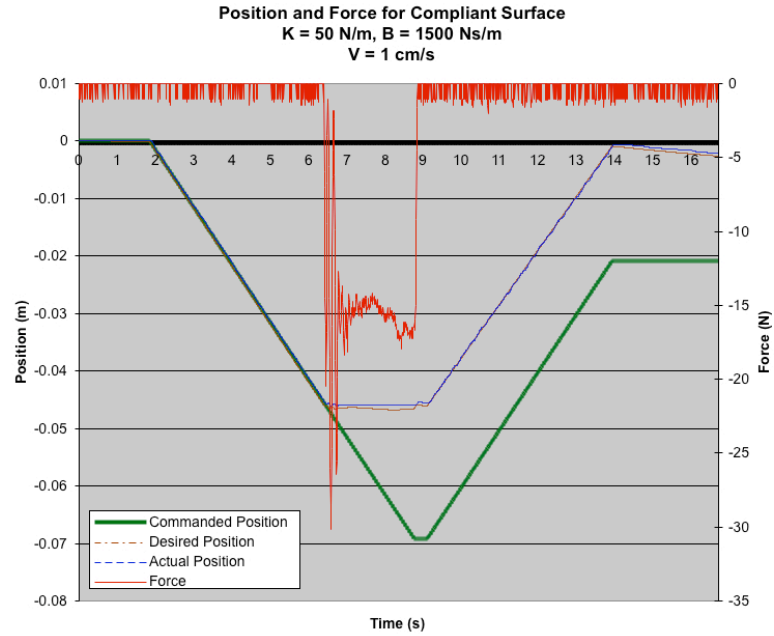
Figure 5.18: Response for K = 50 N/m, B = 1500 Ns/m, V = 1 cm/s on Compliant Surface
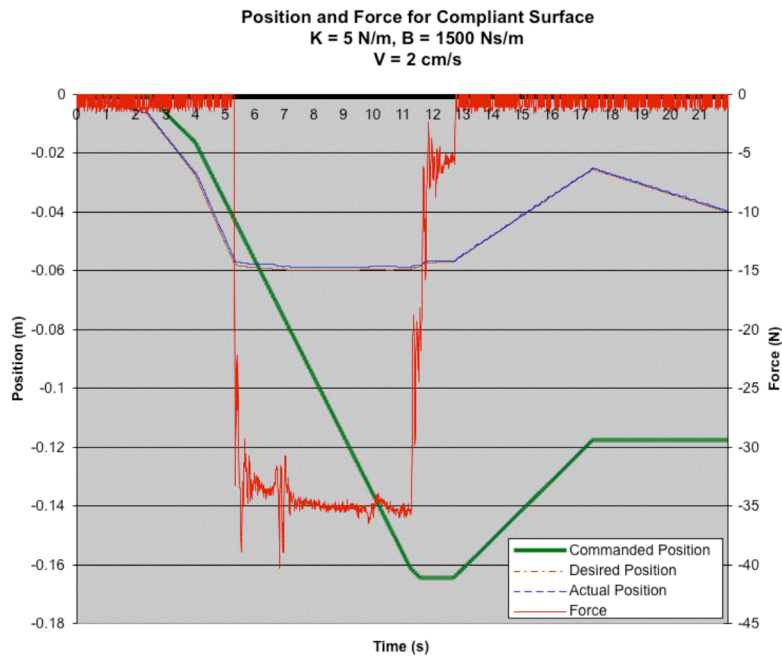
Figure 5.19: Response for K = 5 N/m, B = 1500 Ns/m, V = 2 cm/s on Compliant Surface

117

5.2.2   1-DOF Gain Switching

In the interest of investigating whether abrupt gain switching could be accomplished stably with this admittance controller, a preliminary test was carried out. The manipulator was brought to contact the springboard while in resolved rate mode with the admittance loop turned off. After contact was established and the springboard wall compressed, the admittance controller was switched on with a stiffness of 5 N/m and a damping of 2000 Ns/m. The corresponding response is shown in Figure 5.20. Damping was intentionally set high to slow down and stabilize the response. Results were promising, as the manipulator sprung back smoothly as the springboard stiffness dominated the low manipulator stiffness. This result indicates that a gain-switching controller could be attempted to improve performance on tasks that require different manipulator admittances at different times, for instance the peg-in-hole task that will be tested in Section 5.4.
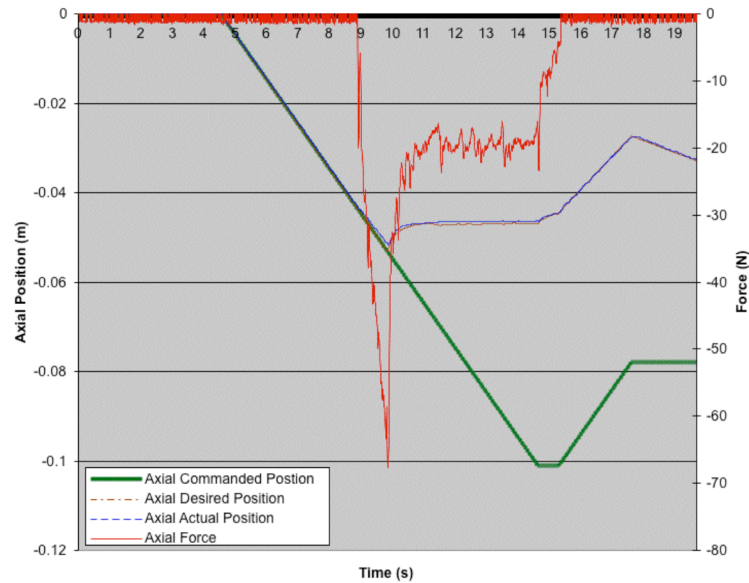
Figure 5.20: Gain Switching from Rigid to K = 5 N/m

118

5.2.3 Foam

Another material Ranger might come into contact with is foam that could be used to render a heavy object neutrally buoyant in the SSL tank. Contact experiments are repeated at 1 cm/s, shown in Figures 5.22-5.25. Since foam is a more delicate surface, as shown by the indentations apparent in Figure 5.21, the stiffness is set low (5 N/m) to minimize steady-state contact force. Damping begins high (1000 Ns/m) and then is reduced until instability occurs. The minimum damping for stability is lower than the springboard, at 425 Ns/m. Note the chatter occurring when the damping is set to 300 Ns/m. The drop in sensed force is noticeable as the damping is reduced, save for the case with chatter.
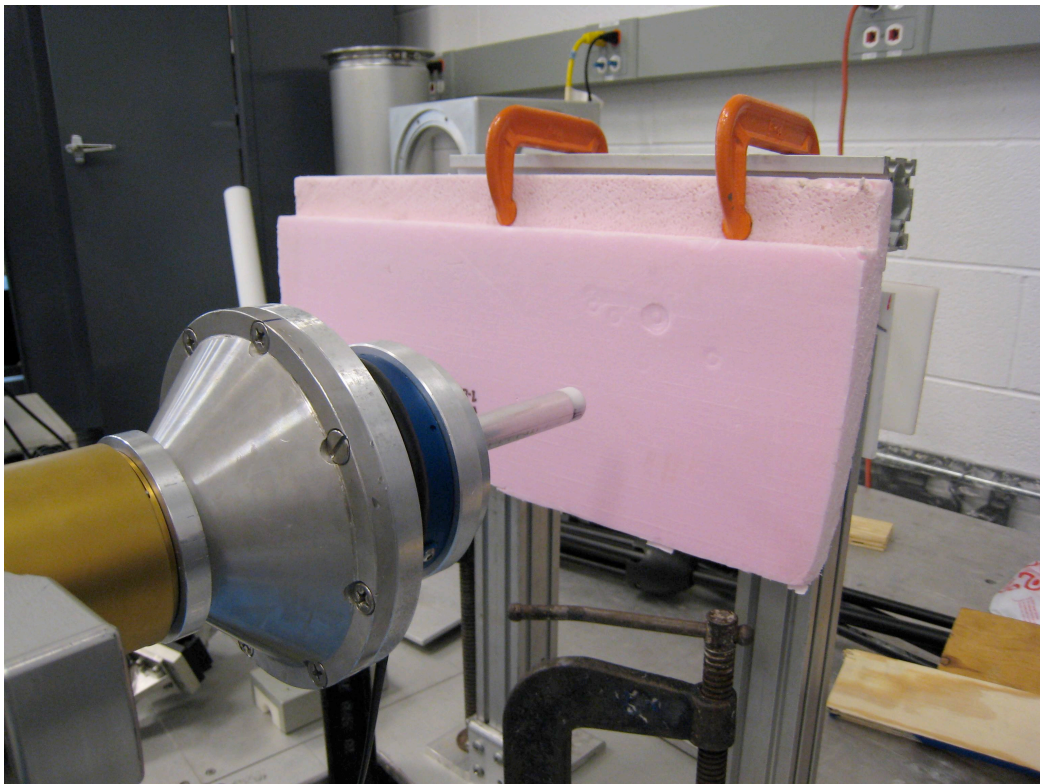
Figure 5.21: Contact Experiment with Foam
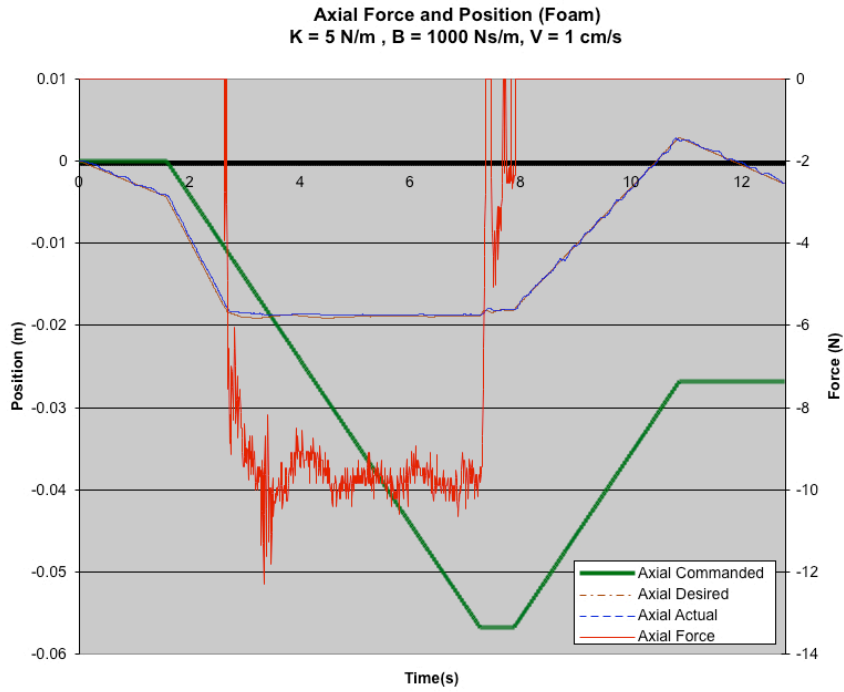
Figure 5.22: Response for K = 5 N/m, B = 1000 Ns/m, V = 1 cm/s on Foam
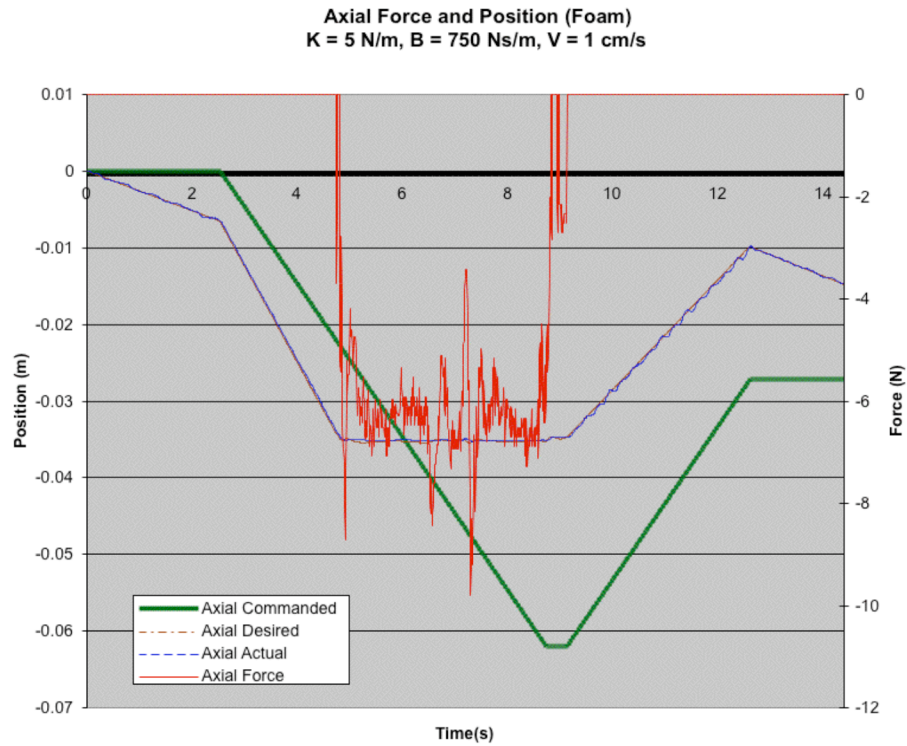
Figure 5.23: Response for K = 5 N/m, B = 750 Ns/m, V = 1 cm/s on Foam
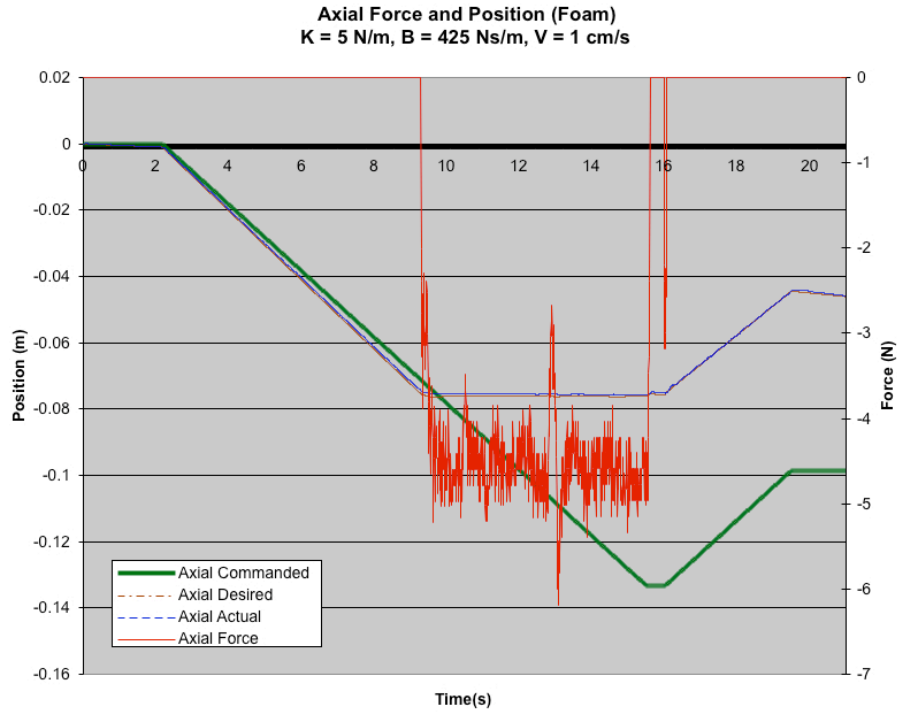
Figure 5.24: Response for K = 5 N/m, B = 425 Ns/m, V = 1 cm/s on Foam
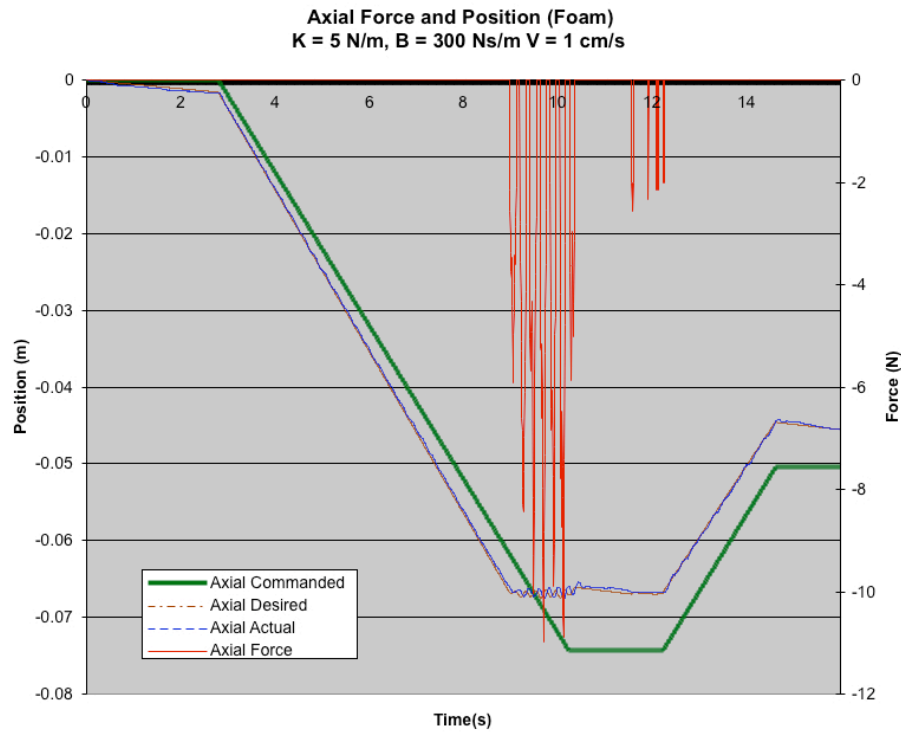
Figure 5.25: Unstable Response for K = 5 N/m, B = 300 Ns/m, V = 1 cm/s on Foam

121

5.2.4 Rigid Surface

Contact tasks with compliant surfaces are a small subset of Ranger's abilities. In general, Ranger interacts with more rigid space structures. In contact with non-forgiving environments, forces can build up quickly using position-control alone, as illustrated in Figure 5.26. If the manipulator were to continue moving forward in this scenario, damage would be done to the robot and/or contacted surface. Clearly, smaller manipulator stiffness would be preferable in rigid contact. This section will investigate if stable contact with low manipulator stiffness can be made, and evaluate the improvement in contact forces over stiff resolved rate control.
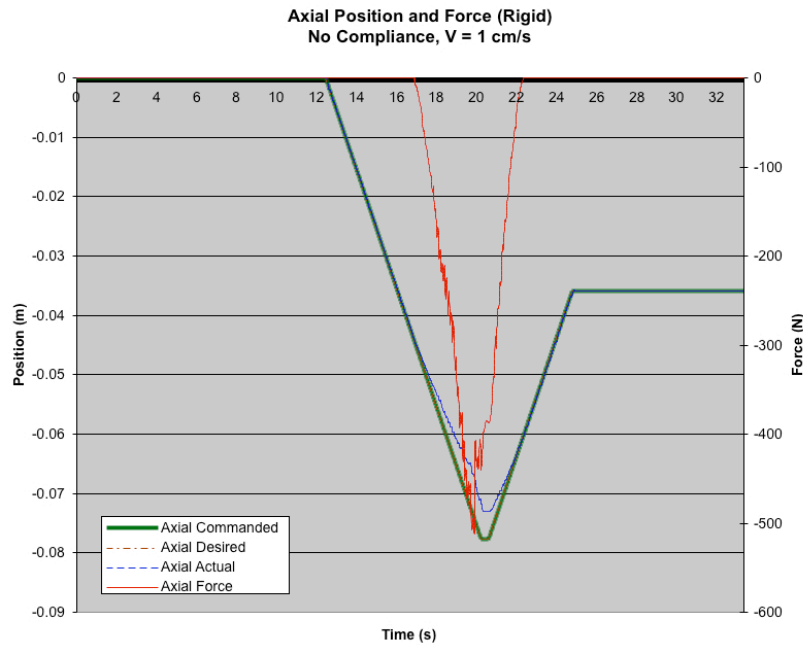
Figure 5.26: Manipulator Contacting Rigid Surface

With the admittance control running, a significant reduction in contact force occurs. Figures 5.27-5.30 illustrate behavior with decreasing manipulator stiffness.

122

Manipulator damping was also set high to prevent unstable chatter that could be particularly damaging with rigid contact. The plots illustrate how the contact force clearly contains two components: Static force, proportional to the desired stiffness and position error, and a transient force, proportional to the desired damping and the velocity error.

$$K_d \left(x_{com} - x \right) + B_d \left(v_{com} - v \right) = F \qquad (5.1)$$

For the high stiffness case (Figure 5.27), the force increases more dramatically as the position error grows. Once the commanded velocity is zero, only the stiffness component of the force remains. The position error at that point is 0.044 m. Multiplying by the desired stiffness of 500 N/m, a force of roughly 22 N is expected, and delivered. For the low stiffness case (Figure 5.30), the damping term dominates and the transient force is level. The expected force from the velocity error of 0.01 cm/s multiplied by the damping of 1500 Ns/m is 15 N, which corresponds to the measured force. Once forward motion ceases, the contact force falls to near-zero quickly, due to the low desired stiffness.

Again, these results indicate that low stiffness can be specified provided that enough damping is supplied. However, they also confirm the tradeoff in positional accuracy seen in the simulation. This occurs because when the manipulator returns to free-space under admittance control, no force is felt and Equation (5.1) can be set to zero.
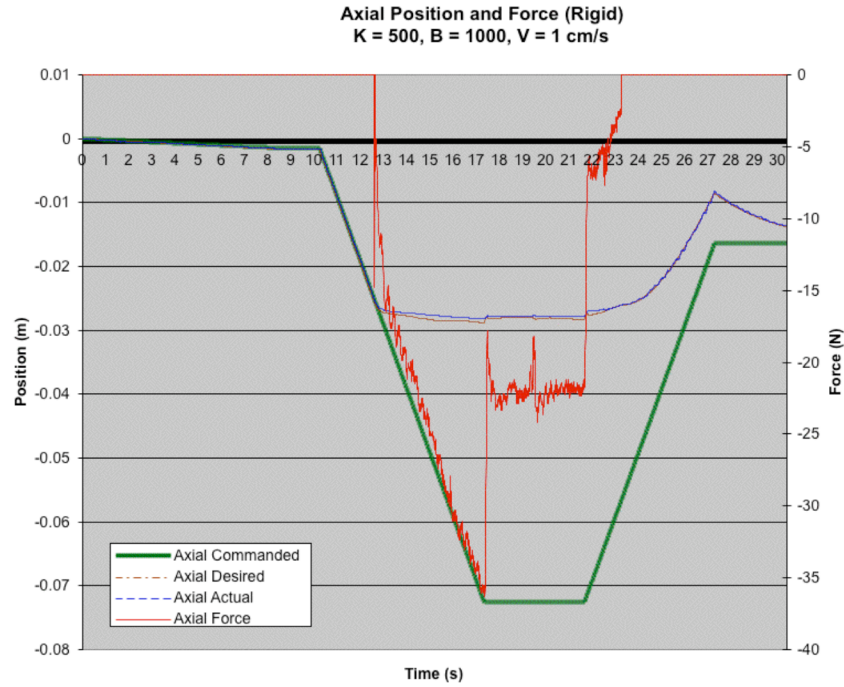
Figure 5.27: Response for K = 500 N/m, B = 1000 Ns/m, V = 1 cm/s on Rigid Surface
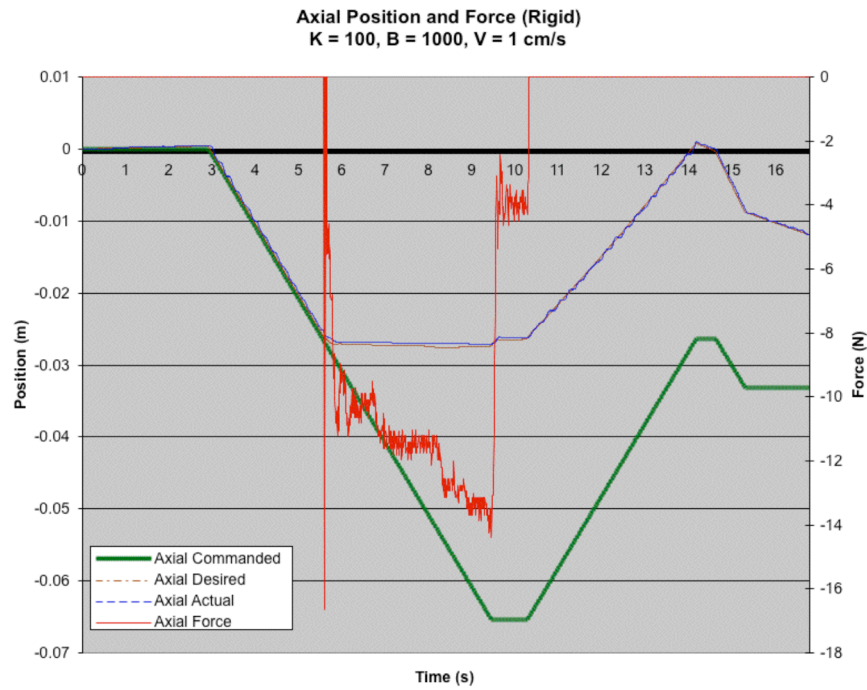
Figure 5.28: Response for K = 100 N/m, B = 1000 Ns/m, V = 1 cm/s on Rigid Surface

124
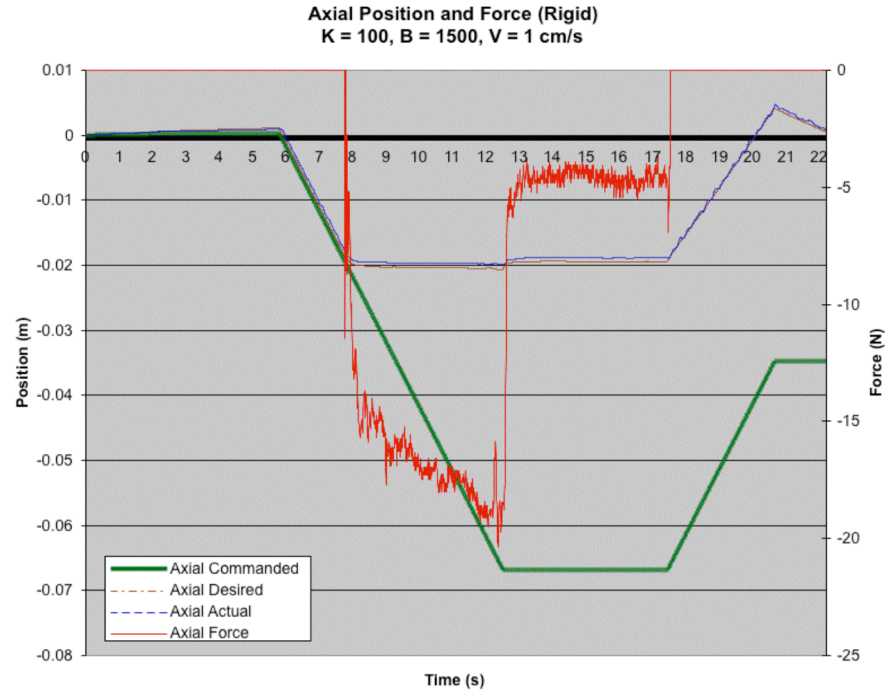
Figure 5.29: Response for K = 100 N/m, B = 1500 Ns/m, V = 1 cm/s on Rigid Surface
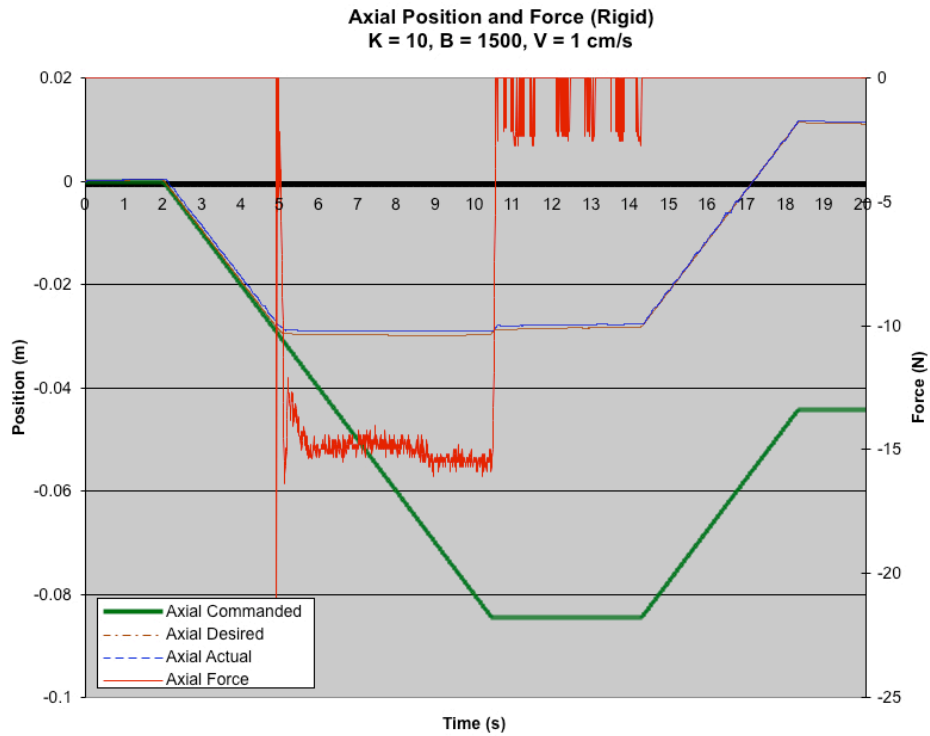
Figure 5.30: Response for K = 10 N/m, B = 1500 Ns/m, V = 1 cm/s on Rigid Surface

Then solving for the velocity with $v_0 = 0$, we obtain

$$v = \frac{K_{des}}{B_{des}}\left(x_{com} - x\right) \tag{5.2}$$

Hence, when the commanded velocity is zero, the actual manipulator velocity in free space is proportional to the stiffness/damping ratio, and decreases as the manipulator approaches its commanded position. For low stiffness/high damping, the manipulator will creep back slowly. At high stiffness/damping ratio, the manipulator will return quickly. This is seen clearly when comparing the free-space responses in Figures 5.27 and 5.30.

5.2.5 Steady-State Force Error

In rigid contact, it is clear that the controller is successfully delivering the commanded impedance at steady state. Equation 2.9 showed that impedance and force are related through velocity. At constant velocity (steady-state), the impedance is proportional to the applied force. At zero commanded velocity, the impedance forces should be proportional to the position error.

$$F_{ss} = \left(x_{com} - x\right)K_{des} \tag{5.3}$$

At nonzero commanded velocity, applied forces are expected to have an additional component that is proportional to the velocity error. Since in rigid contact, the tool tip velocity is held at zero, the velocity error is equal to the commanded velocity. The expected steady-state force is thus:

$$F_{adm} = v_{com}B_{des} + \left(x_{com} - x\right)K_{des} \tag{5.4}$$

For the rigid cases above these can be calculated and compared to the actual

sensed force output. An error can thus be calculated as:

$$E_{adm}(\%) = \frac{F_{adm} - F_{act}}{F_{adm}} = \left(1 - \frac{F_{act}}{v_{com}B_{des} + (x_{com} - x)K_{des}}\right) \times 100\% \qquad (5.5)$$

The average steady-state force error in contact over all the rigid contact runs was less than 11%. It was determined by averaging the force error, during *only* the periods where contact was made (i.e. force readings were nonzero) for 5 runs. The error in general can be attributed to the noisy force readings from the sensor, intermittent contact from vibrations, and the larger oscillatory transient behavior during contact initiation and separation. The matching between desired and actual admittance force during contact can be seen in Figure 5.31 for the cases of Figures 5.27 and 5.30 respectively.
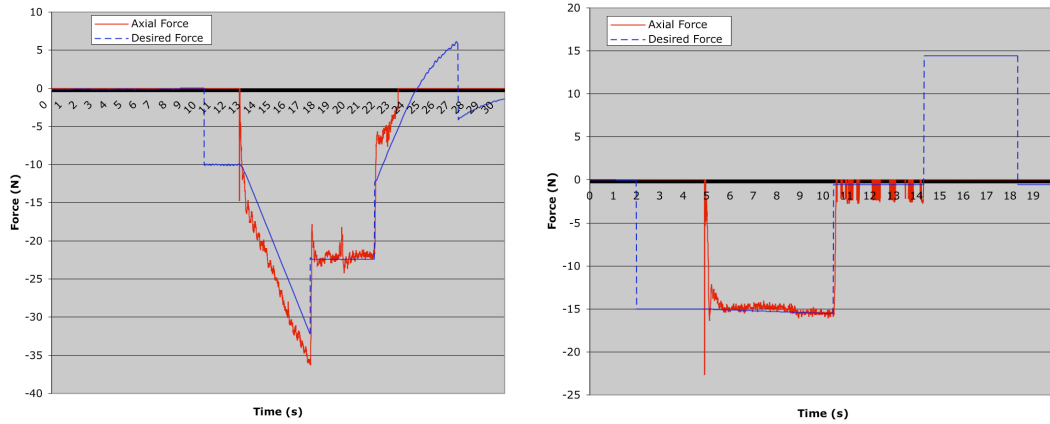
Figure 5.31: Desired Force vs. Actual Force

5.3 Ranger 2-D Test Results

Testing was then expanded to include lateral motion as well. After axial contact is made, the tool-tip is moved in one of the perpendicular directions. Lateral

forces and response will be plotted.

5.3.1 Springboard

The springboard is made from glossy plastic, as well as the tool tip, so lateral friction will be lowest in this case. The case without compliance is shown first, followed by the lateral response without low stiffness and higher stiffness, and finally a response with reduced friction by using a roller-bearing tool tip. With no compliance, axial forces and even lateral forces increase rapidly, especially if there is friction impeding the lateral motion. This is seen in Figure 5.32. However, choosing a low axial stiffness can alleviate the frictional force by decreasing the normal force applied to the surface, as shown in Figure 5.33. By eliminating friction via the roller bearing, Figure 5.34 illustrates how the lateral force is further reduced. In general if the surface is not smooth, the lateral stiffness should be chosen high enough so that the opposing friction force does not cause the tool tip to get "caught". Figure 5.35 illustrates how the position error can be larger with lower stiffness.
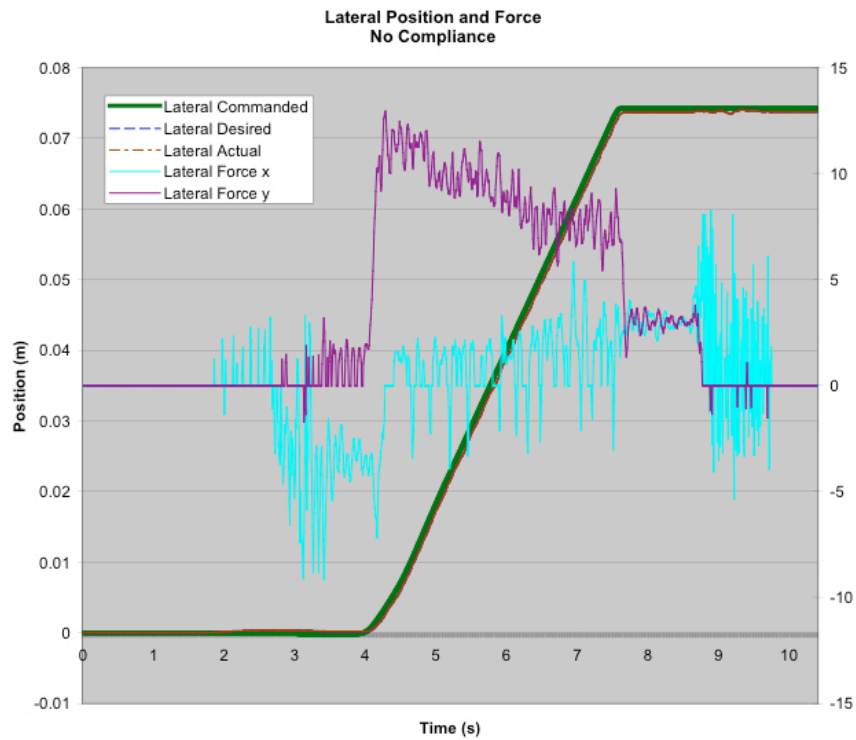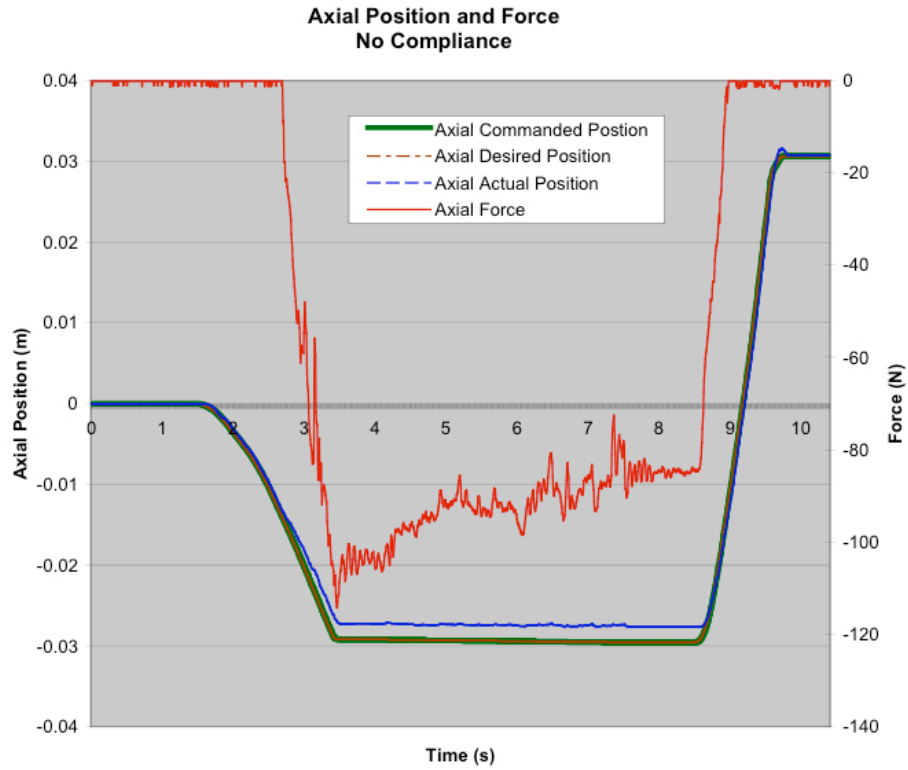
Figure 5.32: 2-DOF Contact with No Compliance

129
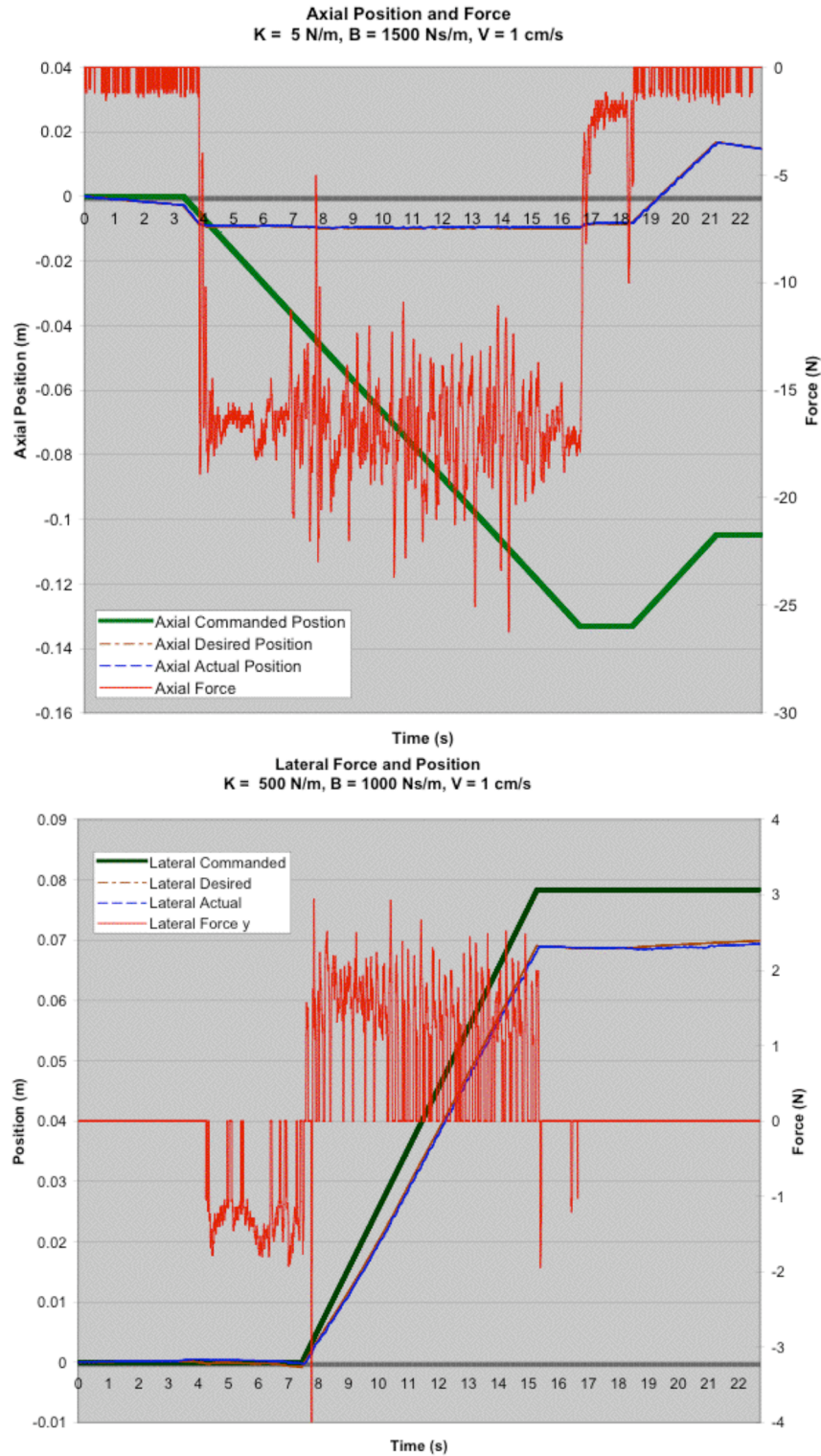
Figure 5.33: 2-DOF Contact with K = 500 N/m, B = 1000 Ns/m, V = 1cm/s
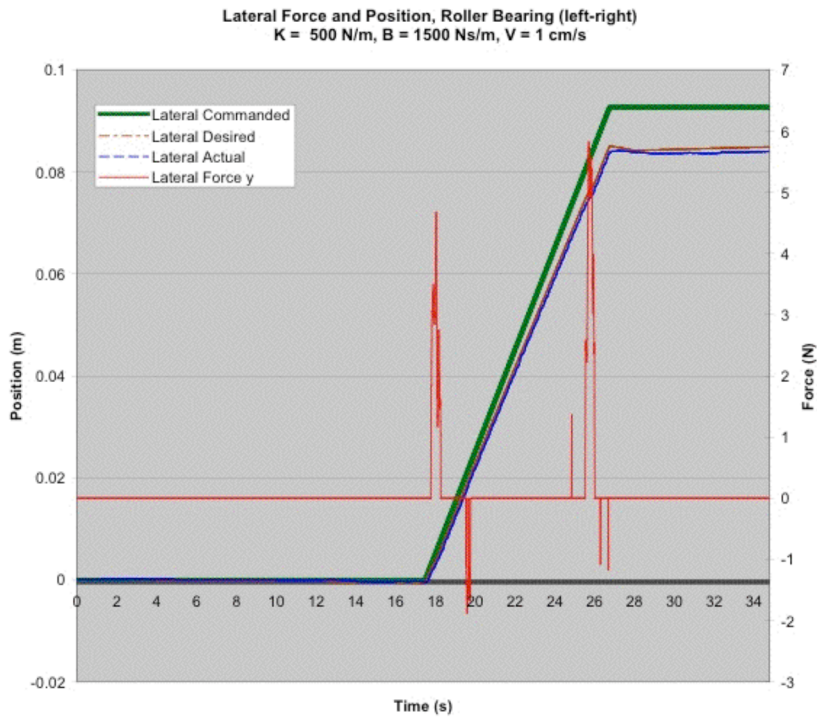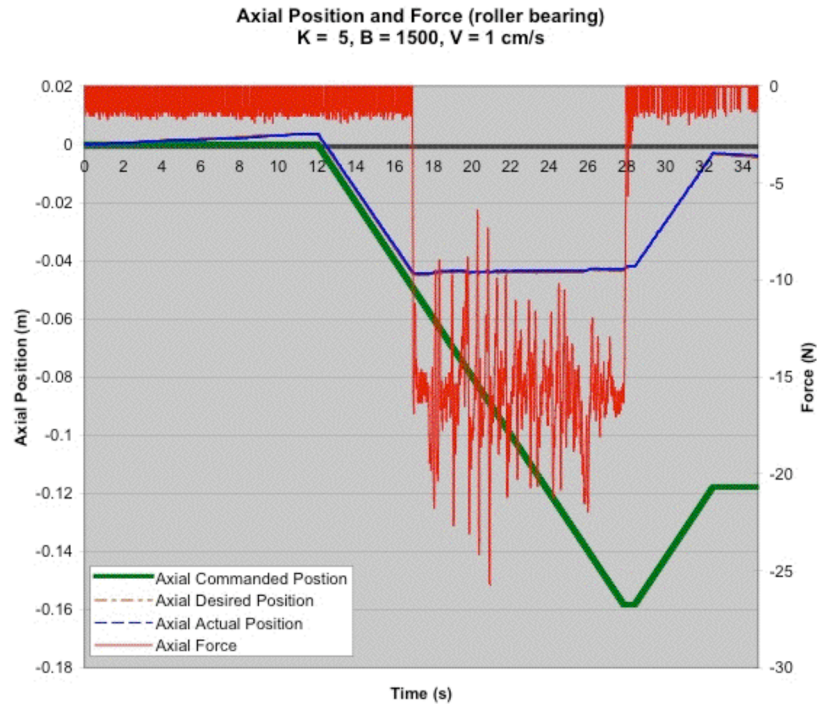
Figure 5.34: 2-DOF Contact on Roller Bearing. K = 500 N/m, B = 1500 Ns/m, V = 1cm/s
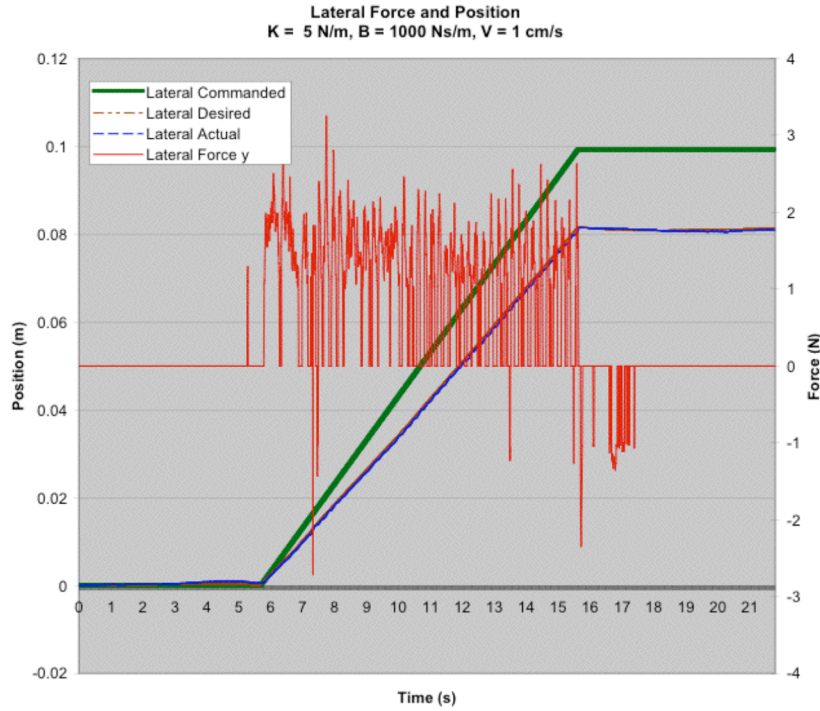
Figure 5.35: Lateral Contact with Lower Lateral stiffness.

5.3.2 Rigid Metal

Similar results are seen when the contact surface used was a rigid aluminum plate. The trajectory followed for this test involved a back-and-forth motion. Low axial stiffness was used so that the normal force would be minimized. Figure 5.37 illustrates how the surface friction causes lateral forces, and how these are relieved with the roller bearing tip.

To investigate the effect of surface roughness, the aluminum plate is replaced by a steel plate with holes machined at 1/2" intervals. In general, the manipulator is capable of traversing the bumpy surface without instability, provided the axial damping is set high enough so that oscillation from the uneven surface is attenuated, as shown in Figure 5.38. For this case, a damping of 2000 Ns/m was chosen.
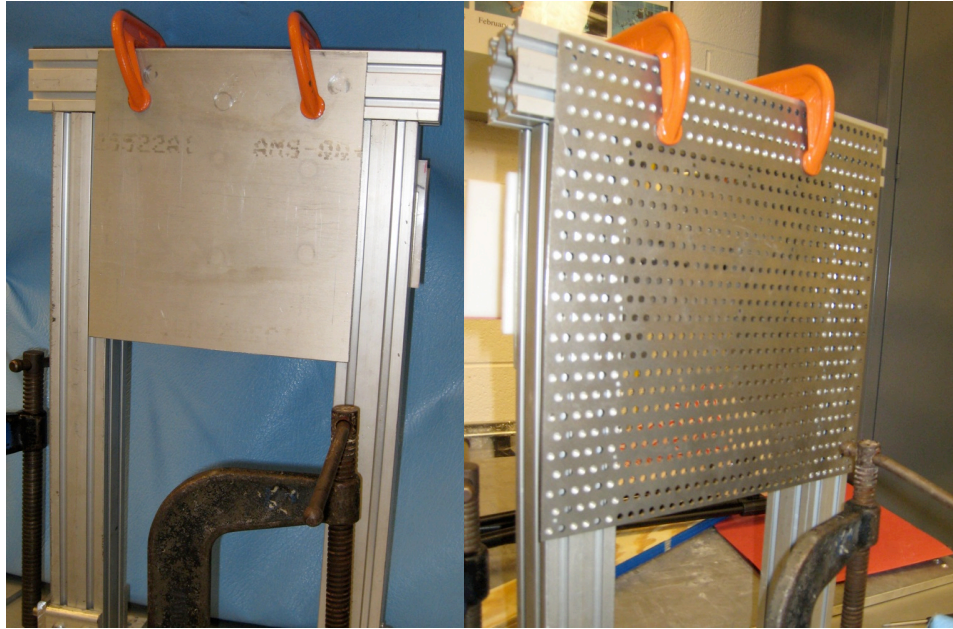
Figure 5.36: Aluminum Plate/Steel Plate with holes
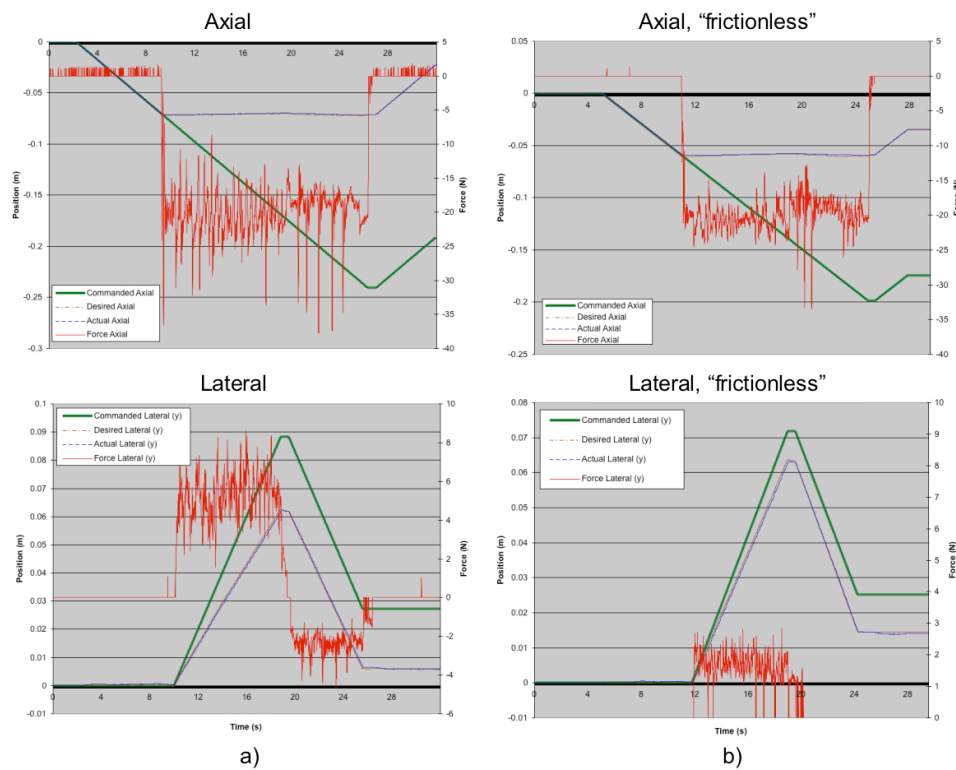
Figure 5.37: 2-DOF Contact with (right) and without (left) Reduced Friction

133
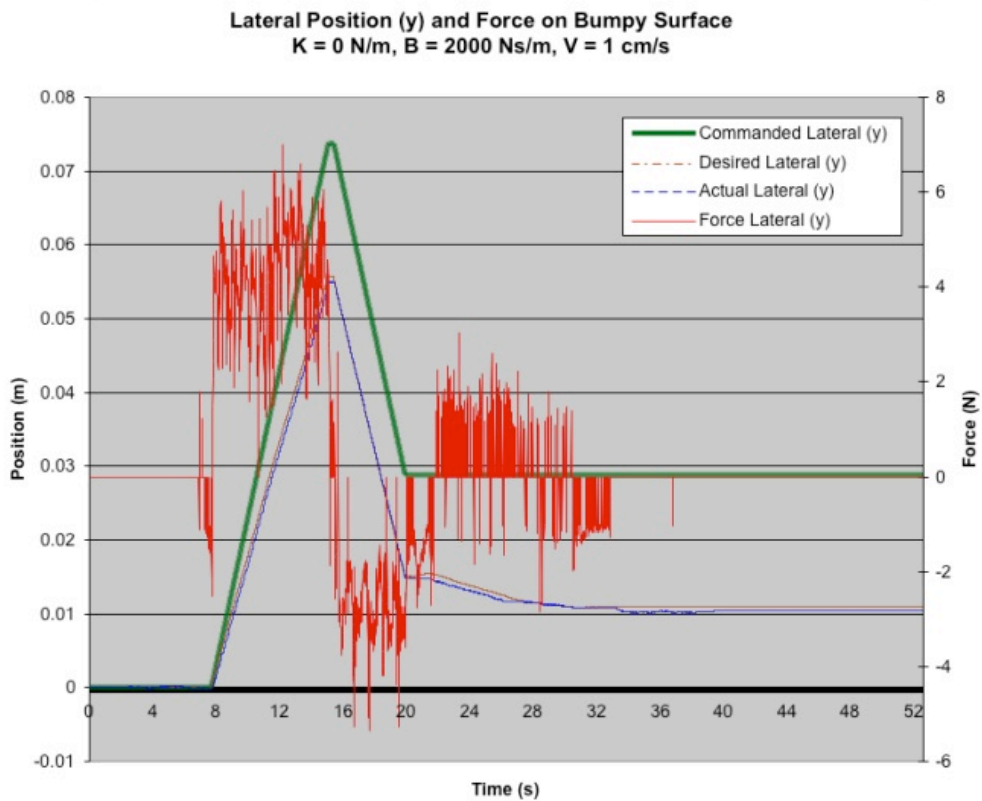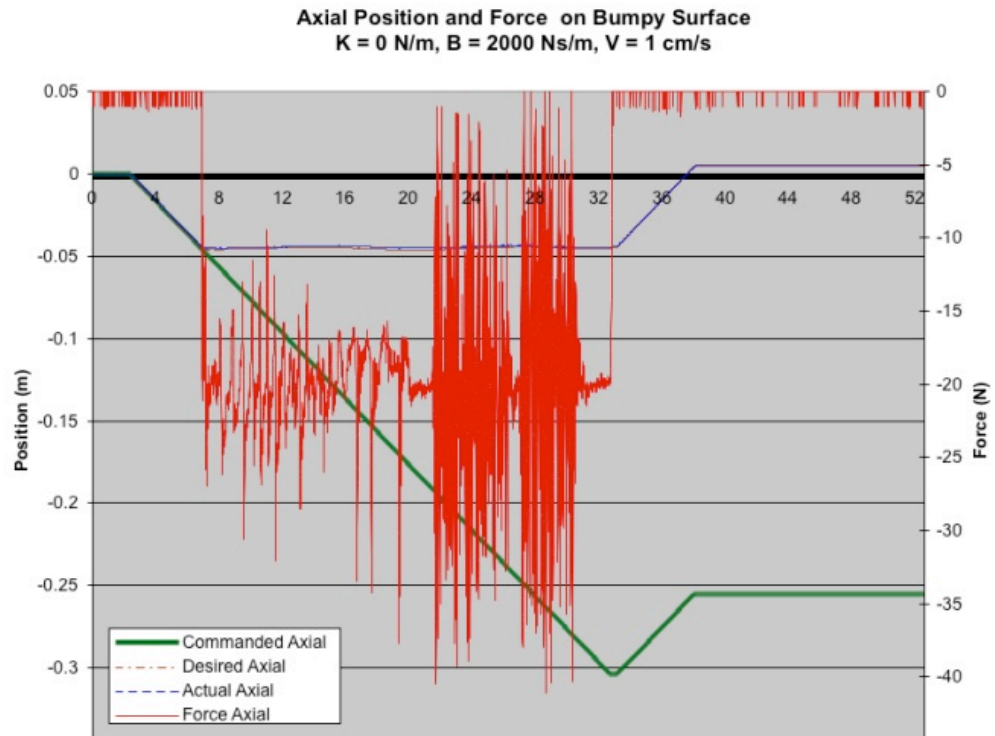
Figure 5.38: 2-DOF Contact on Bumpy Surface

5.4 Ranger Peg-in-Hole Test Results

Qualitative peg-in-hole tests are conducted to prove that they can be successfully accomplished. The trajectory followed for the peg-in-hole task is identical to the 2-DOF task, except with a hole at the end of the lateral motion. With the manipulator pushing axially, the peg is moved toward the hole. Once aligned, the peg should move forward and insert itself, as the resistance is removed. A peg-in-hole task is first accomplished with only lateral compliance, and then rotational compliance is added.

Figure 5.39 shows the peg-in-hole behavior, with low lateral and axial stiffness so as to minimize lateral force and facilitate alignment during insertion. First, the manipulator makes axial contact with the surface, and then moves laterally while still in contact until "interrupted" by the hole. Figure 5.39 depicts the behavior of the manipulator in each phase of motion. During lateral motion, lateral forces increase due to friction from the wooden surface. When the hole is "located", both the axial and lateral forces drop to zero. However, the lateral forces soon increase again because the commanded lateral velocity is still 0.01 m/s, resulting in damping forces of 15 N. These persist until the commanded velocity is set to zero. The compliance in the lateral direction allows the peg to remain aligned with low forces during insertion. The axial force oscillations about zero are due to sensor noise and the force deadband, which is set at 2 N.
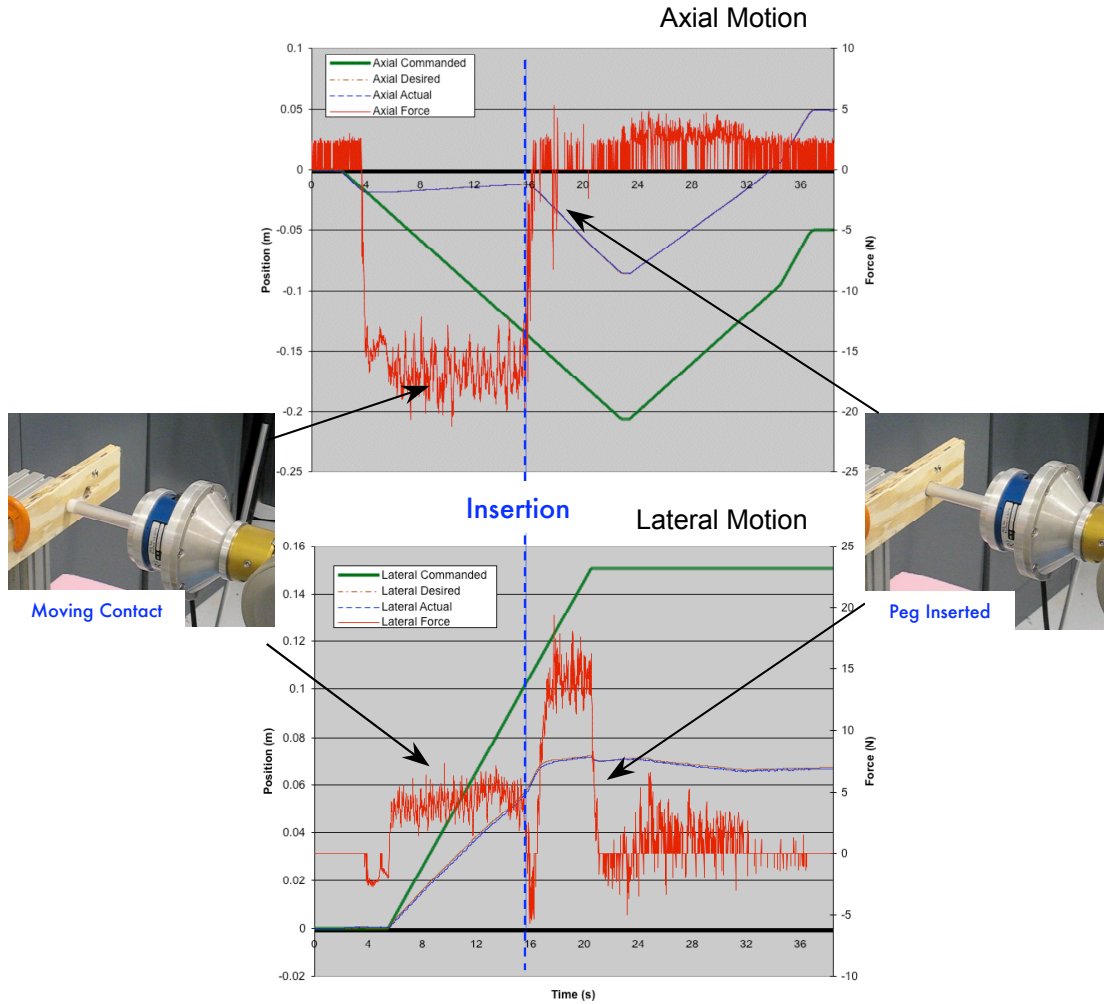
Figure 5.39: Peg In Hole with only Lateral Stiffness

Figure 5.40 then shows the case with the rotational compliance turned on. The rotational damping can be set lower because the link inertia in the wrist is low and the links are stiffer since they are short and compact. Lower rotational damping can help with orientation, but if the damping is set too low, the manipulator can start "getting away" and possibly drift into a joint limit or possibly a singularity, destabilizing the admittance controller. It is suggested that no less than 50 Nms/rad be used. The figure shows high axial forces until the hole is first "found" just before 22 seconds. At this

instant, both lateral and axial forces are momentarily zero, indicating a free-space motion. However, because the entry rate is slow, the peg continues to yaw and move laterally while sitting in the hole until 32 seconds, where it is manually commanded back toward it. At the 48-second mark, the hole is located again, and this time the peg is inserted after which the peg enters and then retracts. Lateral forces increase after the hole is found, indicating that the manipulator is still pushing sideways, until 56 seconds.
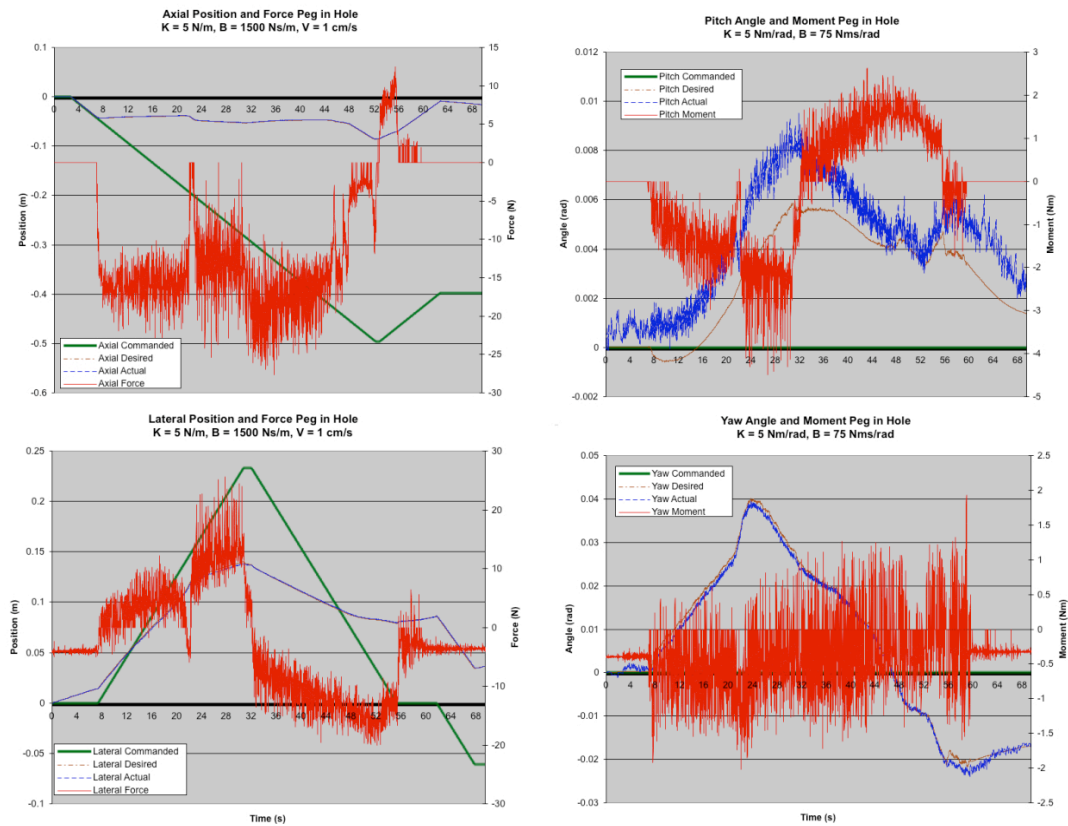
Figure 5.40: Peg In Hole with Rotational Compliance

The peg-in-hole problem is characterized by its natural and artificial constraints. As the peg moves toward the board, high axial stiffness is desirable. As impact is made, low axial stiffness is preferable. Ideally the lateral stiffness should be

137

high when traversing the board laterally, but as the hole encountered, high axial stiffness and low lateral stiffness is desired. The problem could be solved with appropriate gain scheduling/switching, or an adaptive control strategy.

5.5 Summary and Discussion

In general the results are promising, showing that the admittance controller can be used for successful completion of contact tasks, provided that the damping is carefully selected to achieve stability. For rigid contact at a desired stiffness of up to 500 N/m, a damping of 1500 Ns/m is suggested, provided the manipulator tool tip travels at under 2 cm/s. Very low manipulator stiffness can be achieved in this case. For compliant surfaces, such as foam, the damping can be chosen lower for the same stiffness. For motion involving two degrees of freedom, a low axial stiffness may be desirable so that axial forces are low and lateral forces due to friction are reduced. For a peg-in-hole task, using rotational compliance is beneficial for alignment, but can be difficult to control if the damping is too low.

Of course the desired admittance parameters depend greatly on the nature of the task. To determine admittances that are suitable, it is suggested to begin with high damping and low stiffness first, and then gradually decrease damping and/or increase stiffness until the desired behavior is achieved, whether it be low impact force, or good position tracking.

Unfortunately, because the testing stand was not adjustable, determining the effect of arm configuration, as shown in Chapter 4 was not a possibility. Future testing with a more elaborate, larger test stand could allow this to be verified.

Results in practice though, are much different to those obtained in Chapter 4. The stability analysis predicts that the necessary damping for stability increases with desired stiffness. In experimentation, this not always true; occasionally, more damping is required for low stiffness. The erroneous assumption in the stability analysis is that the manipulator never breaks contact with the impacted surface. However, this is untrue, especially in the case of low commanded stiffness. With low commanded stiffness, the manipulator attempts to track a force that is close to zero, driving the modified desired position very close to the surface of the wall, illustrated in Figure 5.41. In practice, this leads to the manipulator breaking contact, which can initiate a limit cycle where the manipulator bounces off the wall, attempting to track a force that cycles between zero and the contact force. The contact force can start becoming large if oscillations occur rapidly and the manipulator accelerates rapidly to compensate. Adding damping slows down the response, allowing the manipulator to attenuate the oscillation and regain contact with the wall. This is why higher damping is required to maintain stability when low stiffness is desired. If a large stiffness is demanded then the modified commanded position will be farther into the surface than for a low stiffness and this problem does not arise.

The model used in Chapter 4 assumes that contact is always maintained. Even if the manipulator were commanded behind the original set point, there would actually be a restoring force in the opposite direction, as shown in Figure 5.42. This might explain why the model is always stable. Of course, discretization and time delays compound the problem as well.
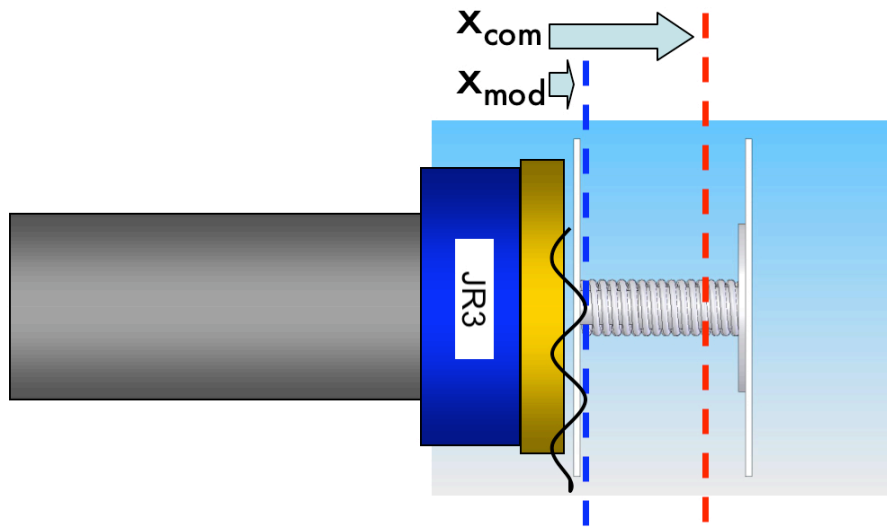
Figure 5.41: Low Desired Stiffness Leads to Instability
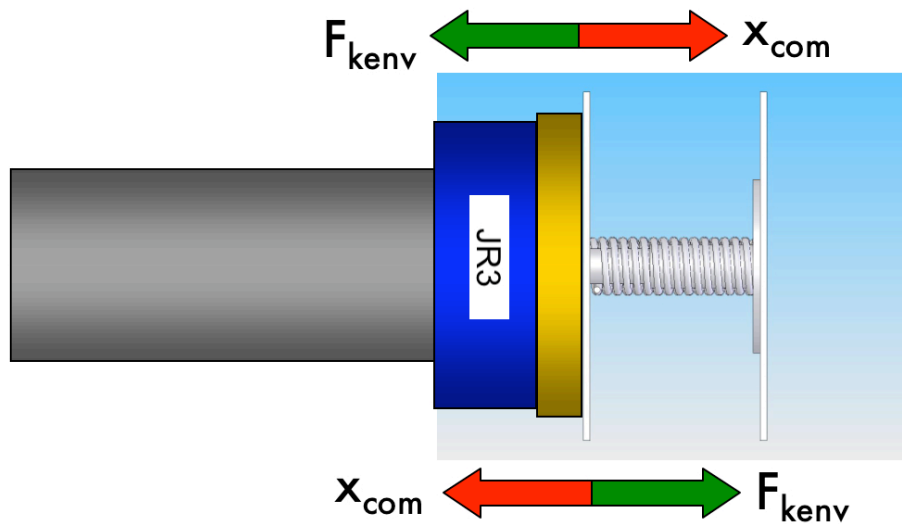
Figure 5.42: Restoring Force when Contact is Maintained

Chapter 6

Conclusions

6.1 Summary

This research provided a framework for determining admittance parameters for performing compliant tasks with a robotic. A stability analysis was developed to find ranges for stable stiffness and damping gains, but the predictions were found to be inaccurate due to the over-simplified model. The model did not fully characterize the nonlinear problems associated with the transition from free space to contact. For Ranger, important effects such as joint friction, link flexibility, force saturation, sensor noise and intermittent contact were not included in the stability model. These contribute to actual behavior that is less stable than the analysis forecasts.

The stability analysis did however give useful insight into the effect of inertia, payload mass and joint position on stability. It revealed that unstable behavior could occur in the vicinity of singularities. The analysis also dismissed the use of the corrective factors introduced by Pelletier and Doyon [15], as they are akin to increasing the system damping.

A simulation was created and used to acquire more insight into Ranger's behavior in contact when operating with the admittance controller. It helped illustrate the shortcomings of the stability analysis and demonstrated what behavior could be expected from the robot under ideal conditions, with different combinations of

stiffness and damping. Tests conducted with Ranger confirmed behaviors from the simulation, and also exposed more inaccuracies predicted by the stability analysis. These experiments also demonstrated that the controller could maintain stable contact with compliant (springs, foam) as well as rigid (metal) environments, provided that enough target damping is specified. The target damping required increases with decreased target stiffness, and higher environment stiffness because intermittent contact was more likely in this case. The controller is also inherently limited to by its bandwidth. Low stiffness and damping increase the system bandwidth, potentially exciting resonances. Examining the expected forces applied at contact revealed that the manipulator was delivering the target admittance. There was a clear proportional relationship between force and velocity via the damping and steady-state force and position error via the stiffness. A quick investigation also revealed that gain-switching was a possibility, whereby the manipulator is switched from stiff positioning in freespace to admittance mode during contact.

Tests also show that stable contact can be maintained while moving across a surface and ultimately, it was demonstrated that Ranger's position-based admittance controller allows a peg-in-hole task to be accomplished successfully with lower overall interaction forces than with rigid position control alone. A gravity compensation algorithm was written so that the effect of gravity at the end effector could be removed from force sensor readings.

There is a tradeoff between low manipulator stiffness and the damping required for stability. Lower steady-state forces are maintained, but in motion, contact forces are higher. This is expected because the steady-state stiffness force is

proportional to the position error and the transient damping force is proportional to the velocity error. Another important tradeoff is that of damping vs. speed and steady-state error. Increasing the manipulator damping results in a more sluggish manipulator response. If the manipulator stiffness is specified low, then when the manipulator is released from contact, it will be very slow to return to its commanded position. If the manipulator stiffness is set to zero, it will not return to its commanded position, and the error will persist, and there is currently no way to re-set the commanded position while the admittance control is active.

Depending on the nature of the task, a sluggish response might be desirable. This brings up another important, point. "Suitable" manipulator gains heavily depend on the goals of the tasks. The overlying assumption in the experiments presented in this thesis was that the force should be minimal at steady-state. However, if a task warrants a certain nonzero force to be applied at steady state, then the operator can specify a small stiffness and move the set point far past the contact surface, or a large stiffness and move the set point only slightly past the contact surface. If positional accuracy is essential, one might consider a higher stiffness, with lower damping and sacrificing the contact forces. If only alignment is required, and low contact forces to achieve this, then low stiffness with high damping may be desired.

Nevertheless, a useful procedure for narrowing down "suitable" gains for any contact scenario is presented here: starting with a low stiffness and high damping, which is stable, and then converging to a higher stiffness and/or lower damping until the desired behavior is obtained.

Compliance is a useful tool that will facilitate tasks involving alignment and

143

contact. Clearly, with enough practice and skill, a peg-in-hole insertion task can be performed without compliance, provided that the operator has adequate visual information throughout. The operator can visually line up the peg with the hole first, and then advance toward it. However, since Ranger only has a limited number of camera views available, some of which may become occluded during manipulator positioning, compliance can certainly help ease the task. It can also afford a less experienced Ranger operator some forgiveness when making contact with a rigid surface so that impact damage is minimized.

6.2 Future Work

All the tests described above are conducted with contact in the axial direction of the manipulator tool tip. This is only a subset of the possible configurations that Ranger is capable of working in. While testing impedance in all the possible arm orientations is outside the scope of this research, tests could be conducted to assess if the behavior is similar to the results already obtained, or what differences arise. Additional testing could be done with added mass at the end-effector to reveal if increasing payload mass or changing the manipulator configuration affects stability as described in Chapter 4. Once suitable gains have been chosen with compliance in the horizontal motion plane, the same gains could be tested for contact in an upward, downward or lateral direction. The manipulator would be made to approach a surface in these directions and the response would be verified for analogous responses. Ultimately, the manipulator would ideally be able to respond appropriately to a random contour. With significant additional testing, a wide range of gains could be

found for every possible contact scenario. While this may not be realistic, what this does suggest is that Ranger could potentially "rehearse" a task to determine suitable admittance parameters and tune to the gains for desired performance.

The gravity compensation could be expanded to include inertial compensation of the payload as well. All throughout testing it was obvious that the force errors due to arm acceleration were nontrivial. Using mass and center of mass estimates, and assuming acceleration can accurately be measured, the inertial effects could also be calculated and subtracted from the force readings.

At this point, there are many directions in which future research could significantly affect the stability, performance and practicality of the admittance controller. The current operating approach is not adequate for an autonomous situation, but workable for tele-operated use, where the operator can adjust position and change gains manually according to how contact is made. Ideally, the admittance controller should be able to run throughout a trajectory, where gain scheduling could be used to switch gains when different contact situations are encountered. An adaptive controller, like the one implemented by Guion [29], that automatically tuned the gains to satisfy some force/position criteria could also be very beneficial. Also, the admittance compensator does not necessarily need to be a mass-spring-damper model, but some other more abstract (less intuitive) controller that would give more stable results, and possibly better performance. It might be worthwhile investigating other compensators. Force estimation work done by Aksman [42] at the Space Systems Lab could be used to detect contact that does not occur at the tool tip or eliminate the need for a force/torque sensor.

Since Ranger was designed as a neutral buoyancy vehicle, the ultimate manifestation of this research would be to test the admittance controller underwater. This might make the manipulator more stable, as the effect of gravity is reduced and the viscous drag of the water might help damp out unwanted oscillation in contact.

A human factors analysis could be an interesting study to perform. Evaluating to what extent compliance helps an operator achieve a task would give an indication as to how useful/important this controller actually is.

It might be worth mentioning that the Ranger's controller was certainly not designed with compliance in mind. The current high-gain servo loop lends itself well to position-based schemes, which are not necessarily the best way to achieve compliance. A better characterization of Ranger's dynamics could lead to incorporation of model feedforward, which would allow other compliance control schemes to be attempted, such as impedance control or natural admittance control. Impedance control looks at the position/velocity errors and outputs the appropriate forces to apply for achieving target impedance. It would allow lower impedances to be specified at low bandwidth. Natural admittance control is a passivity-based scheme that uses to system dynamics to find the target admittance that makes the robot behave passively in contact, thereby improving stability. At this point however, this particular position-based admittance controller provides beneficial compliant capability to Ranger, with definite potential for improvement.

Appendices

Appendix A: Gravity Compensation Testing Results

Gravity Compensation Testing
Enrico Sabelli, 3/21/2007

Only the FTS and Plate:

Mass (kg)	0.895		
Center of Mass (CoM), (m)	0	0	0.029

Trial:	1			2			3			4			5			6			7			8			9			10			Averages		
Estimated EE Mass (kg)	0.806															0.791						0.796						0.796			0.79725		
Estimated CoM (m) [x y z]	-0	-0	0.016													-0	-0	0.015				-0	-0	0.015				-0	-0	-0.15	-0.003	-0.002	-0.026
Estimated EE Mass error (%)	9.944134078			100			100			100			100			11.62011173			100			11.06145251			100			11.06145251			10.92178771		
Estimated CoM error	0.002	0.002	0.013	0	0	0.029	0	0	0.029	0	0	0.029	0	0	0.029	0.003	0.001	0.014	0	0	0.029	0.003	0.001	0.014	0	0	0.029	0.002	0.002	0.179	0.001	0.0006	0.0394
Force Deviation from zero (N):																																	
Position 1 (up)	0.2	0.2	0.7	0.2	0.2	1.1	0.1	0.2	0.7	0.1	0.2	0.7	0.2	0.2	0.7	0.1	0.2	0.6	0.2	0.2	0.8	0.1	0.2	0.8	0.2	0.2	0.9	0.2	0.2	0.9	0.16	0.2	0.79
Position 2 (down)	0.2	0.1	1.4	0.2	0.2	1.7	0.2	0.2	1.7	0.2	0.2	2	0.2	0.2	1.8	0.1	0.2	1.7	0.2	0.2	1.9	0.1	0.1	1.9	0.2	0.2	1.7	0.2	0.2	1.9	0.18	0.18	1.77
Position 3 (side)	1.2	0.4	0.7	1.1	0.5	0.7	1.2	0.5	0.9	1.2	0.4	0.9	1.2	0.5	1	1	0.4	1	1	0.4	0.8	1	0.5	1	1	0.5	1	1.1	0.5	1	1.1	0.46	0.9
Position 4 (45 degrees)	0.5	0.8	1.2	0.5	0.9	1.4	0.5	0.9	1.4	0.6	0.9	1.4	0.5	0.9	1.4	0.4	0.8	1.5	0.5	0.9	1.5	0.4	0.7	1.4	0.5	0.8	1.9	0.5	0.9	1.4	0.49	0.85	1.45
Torque Deviation from zero (Nm):																																	
Position 1 (up)	0.02	0.02	0.02	0.02	0.02	0.02	0.02	0.02	0.02	0.02	0.02	0.02	0.02	0.02	0.02	0.02	0.02	0.02	0.02	0.02	0.02	0.02	0.02	0.02	0.02	0.02	0.02	0.02	0.02	0.02	0.02	0.02	0.02
Position 2 (down)	0.02	0.02	0.02	0.02	0.02	0.02	0.02	0.02	0.02	0.02	0.02	0.02	0.02	0.02	0.02	0.02	0.02	0.02	0.02	0.02	0.02	0.02	0.02	0.02	0.02	0.02	0.02	0.02	0.02	0.02	0.02	0.02	0.02
Position 3 (side)	0.02	0.02	0.02	0.02	0.02	0.02	0.02	0.02	0.02	0.02	0.02	0.02	0.02	0.02	0.02	0.02	0.02	0.02	0.02	0.02	0.02	0.02	0.02	0.02	0.02	0.02	0.02	0.02	0.02	0.02	0.02	0.02	0.02
Position 4 (45 degrees)	0.02	0.02	0.02	0.02	0.02	0.02	0.02	0.02	0.02	0.02	0.02	0.02	0.02	0.02	0.02	0.02	0.02	0.02	0.02	0.02	0.02	0.02	0.02	0.02	0.02	0.02	0.02	0.02	0.02	0.02	0.02	0.02	0.02
Max Force Deviation from zero (N)	1.2	0.8	1.4	1.1	0.9	1.7	1.2	0.9	1.7	1.2	0.9	2	1.2	0.9	1.8	1	0.8	1.7	1	0.9	1.9	1	0.7	1.9	1	0.8	1.9	1.1	0.9	1.9	1.1	0.85	1.79
Percentage of force remaining	13.67	9.112	15.95	12.53	10.25	19.36	13.67	10.25	19.36	13.67	10.25	22.78	13.67	10.25	20.5	11.39	9.112	19.36	11.39	10.25	21.64	11.39	7.973	21.64	11.39	9.112	21.64	12.53	10.25	21.64	12.529	9.6811	20.387
Max Torque Deviation from zero (Nm)	0.02	0.02	0.02	0.02	0.02	0.02	0.02	0.02	0.02	0.02	0.02	0.02	0.02	0.02	0.02	0.02	0.02	0.02	0.02	0.02	0.02	0.02	0.02	0.02	0.02	0.02	0.02	0.02	0.02	0.02	0.02	0.02	0.02
Percentage of trq remaining	7.855	7.855	7.855	7.855	7.855	7.855	7.855	7.855	7.855	7.855	7.855	7.855	7.855	7.855	7.855	7.855	7.855	7.855	7.855	7.855	7.855	7.855	7.855	7.855	7.855	7.855	7.855	7.855	7.855	7.855	7.8549	7.8549	7.8549

With Cylinder:

Mass (kg)	2.08		
Center of Mass (CoM), (m)	0	0	0.092

Trial:	1			2			3			4			5			6			7			8			9			10			Averages		
Estimated EE Mass (kg)	1.941						1.938						1.941																		1.94		
Estimated CoM (m) [x y z]	-0	-0	0.076				-0	-0	0.075				-0	-0	0.075																-0.004	-0.004	0.0753
Estimated EE Mass error (%)	6.682692308			100			6.826923077			100			6.682692308			100			100			100			100			100			6.730769231		
Estimated CoM error	0.004	0.003	-0.05	0	0	0.029	0.004	0.004	-0.05	0	0	0.029	0.004	0.004	-0.05	0	0	0.029	0	0	0.029	0	0	0.029	0	0	0.029	0	0	0.029	0.0012	0.0011	0.0064
Force Deviation from zero (N):																																	
Position 1 (up)	0.7	1.7	1	0.7	1.7	1	0.7	1.7	0.8	0.8	1.7	1	0.7	1.6	0.8																0.72	1.68	0.92
Position 2 (down)	1.2	1.4	0.4	1.2	1.2	0.4	1.3	1.2	0.2	1.2	1.2	0.2	1.3	1.3	0.4																1.24	1.26	0.32
Position 3 (side)	1.4	2.2	0.8	1.4	2.2	1	1.4	2.1	0.4	1.4	2.2	0.8	1.5	2.1	0.6																1.42	2.16	0.72
Position 4 (45 degrees)	0.8	2.5	0.4	0.8	2.4	0.8	0.8	2.3	0.3	0.6	2.4	0.5	0.9	2.4	0.4																0.78	2.4	0.48
Torque Deviation from zero (Nm):																																	
Position 1 (up)	0.13	0.34	0.04	0.13	0.3	0.02	0.15	0.31	0.02	0.14	0.31	0.02	0.14	0.32	0.02																0.138	0.316	0.024
Position 2 (down)	0.03	0.18	0.01	0.02	0.17	0.01	0.03	0.16	0.01	0.02	0.15	0.01	0.03	0.16	0.01																0.026	0.164	0.01
Position 3 (side)	0.19	0.2	0.1	0.18	0.2	0.08	0.19	0.22	0.09	0.19	0.22	0.09	0.19	0.21	0.09																0.188	0.21	0.09
Position 4 (45 degrees)	0.06	0.22	0.04	0.09	0.23	0.07	0.07	0.22	0.08	0.07	0.23	0.08	0.09	0.23	0.08																0.076	0.226	0.07
Max Force Deviation from zero (N)	1.4	2.5	1	1.4	2.4	1	1.4	2.3	0.8	1.4	2.4	1	1.5	2.4	0.8																1.42	2.4	0.92
Percentage of force remaining	6.861	12.25	4.901	6.861	11.76	4.901	6.861	11.27	3.921	6.861	11.76	4.901	7.351	11.76	3.921																6.9591	11.762	4.5087
Max Torque Deviation from zero (Nm)	0.19	0.34	0.1	0.18	0.3	0.08	0.19	0.31	0.09	0.19	0.31	0.09	0.19	0.32	0.09																0.188	0.316	0.09
Percentage of trq remaining	10.1	18.07	5.315	9.568	15.95	4.252	10.1	16.48	4.784	10.1	16.48	4.784	10.1	17.01	4.784																9.993	16.797	4.7839

Appendix B: CAD Drawings of Springboard Parts

Springboard Top

20.00
Ø.27 THRU ALL
⌵ Ø.53X82°
6.00
3.00
4.00
8.00
12.00
16.00
.125

Springboard Bottom

20.00
4.00   4.00   4.00   4.00
16X Ø.16 THRU
10-32 UNF - 2B THRU
Ø.75
2.00
3.00
6.00
1.00
.125

Drawing 1: Springboard Cylinder

4X Ø.20 THRU ALL
⌵ Ø.41 X 82°

Ø.75

Ø.60

1.00

Ø3.00

1.90

.125

5   4   3   2   1

Drawing 2: Springboard Piston

Ø.60

Ø.25

Ø.20 ⍗ 1.00
1/4-20 UNC - 2B ⍗ .50

3.00

5   4   3   2   1

149
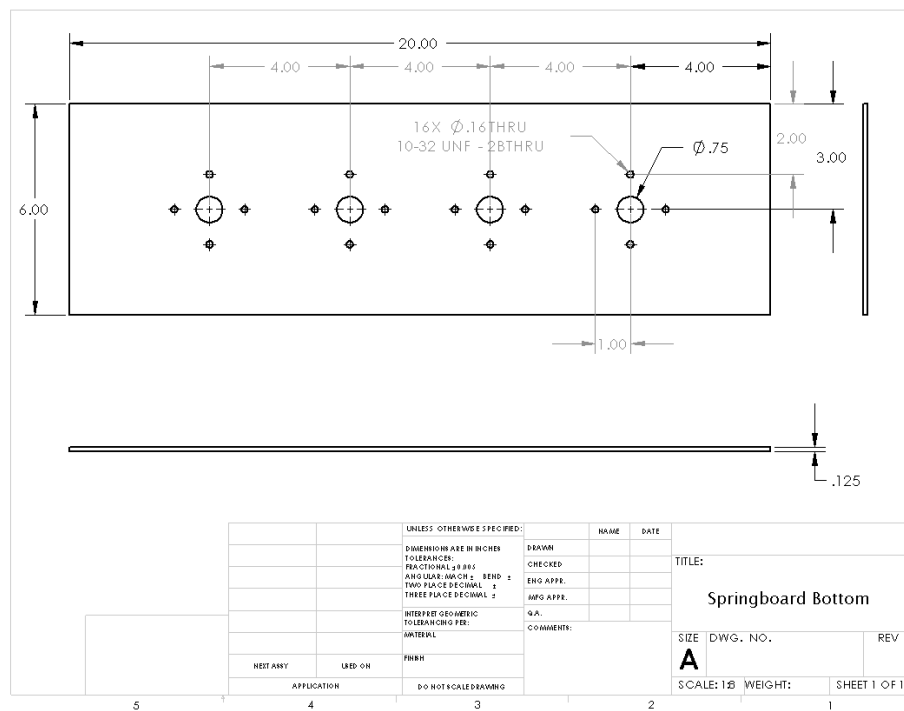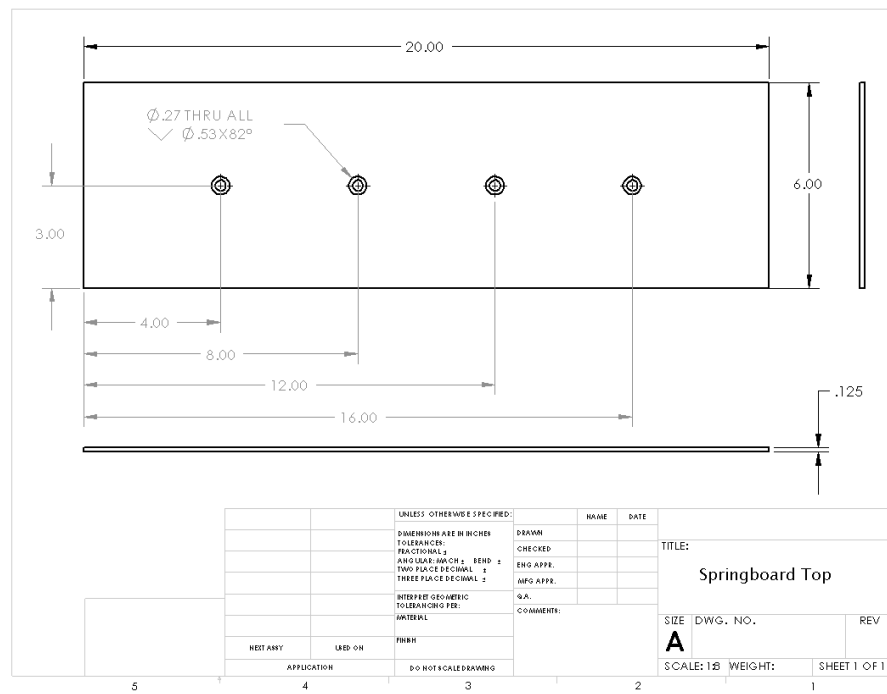
Compression and Die Springs
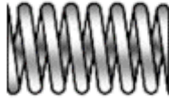
Part Number: **9657K18**

Type	Compression Springs
Material	Steel
Steel Type	Zinc-Plated Spring-Tempered Steel
System of Measurement	Inch
Outside Diameter	7/8"
Wire Size	.091"
Overall Length	3"
Ends	Closed and Ground
Wire Type	Round Wire
Load	25.07 lbs.
Deflection at Load	1.35"
Rate	18.6 lbs./inch
Compressed Length	1.65"
Specifications Met	Not Rated
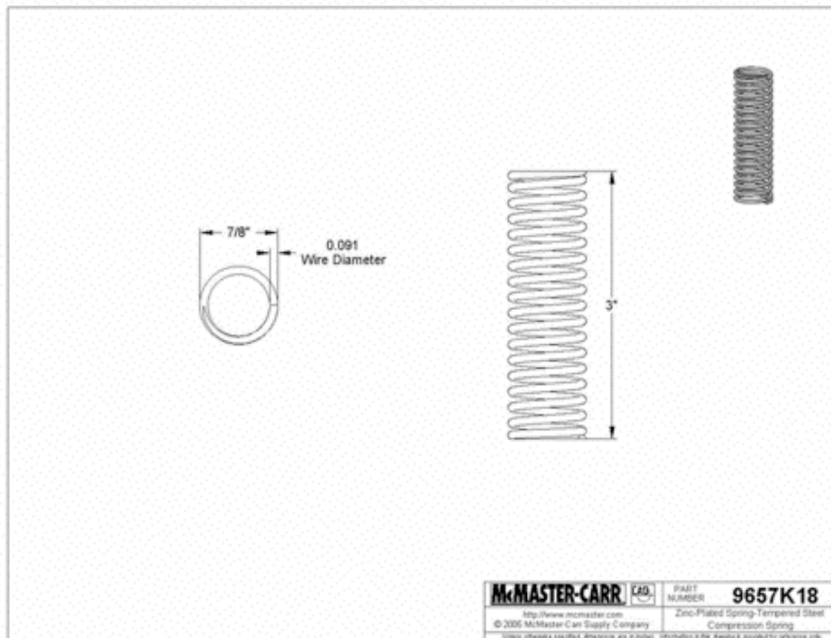
7/8"

0.091 Wire Diameter

3"

McMASTER-CARR
http://www.mcmaster.com
© 2006 McMaster-Carr Supply Company

PART NUMBER **9657K18**
Zinc-Plated Spring-Tempered Steel
Compression Spring

Unless otherwise specified, dimensions are in inches. Information in this drawing is provided for reference only.

Appendix C: CAD drawings of F/T Sensor Attachments

FTS Adapter Plate Front

FTS Adapter Plate Back

F/T Sensor IEEM Adapter

6X Ø.11 ▽.43
6-32 UNC - 2B ▽.28

Ø1.55

6X Ø.18 THRU
⊔ Ø.38 ▽.11

.50

2.60

1.00

1.00

Finger Base

1.00

Ø.20 THRU
1/4-20 UNC - 2B THRU

Ø.20

1.575

2.50

.200

.125

Finger

Ø.20 ▼1.00
1/4-20 UNC - 2B ▼.50

Ø.20 ▼1.00
1/4-20 UNC - 2B ▼.50

3.00

Ø.75

UNLESS OTHERWISE SPECIFIED:

DIMENSIONS ARE IN INCHES
TOLERANCES:
FRACTIONAL ±
ANGULAR: MACH ±   BEND ±
TWO PLACE DECIMAL ±
THREE PLACE DECIMAL ±

INTERPRET GEOMETRIC
TOLERANCING PER:

MATERIAL

FINISH

NAME | DATE

DRAWN
CHECKED
ENG APPR.
MFG APPR.
Q.A.
COMMENTS:

NEXT ASSY | USED ON
APPLICATION

DO NOT SCALE DRAWING

TITLE:
Finger

SIZE | DWG. NO. | REV
A

SCALE: 2:1 | WEIGHT: | SHEET 1 OF 1

Bearing Finger Tip

Ø.27 THRU
⌵ Ø.53X82°

.50

1.00

.500

1.00

.125

.125

1.00

.875

R.125

UNLESS OTHERWISE SPECIFIED:

DIMENSIONS ARE IN INCHES
TOLERANCES:
FRACTIONAL ±
ANGULAR: MACH ±   BEND ±
TWO PLACE DECIMAL ±
THREE PLACE DECIMAL ±

INTERPRET GEOMETRIC
TOLERANCING PER:

MATERIAL

FINISH

NAME | DATE

DRAWN
CHECKED
ENG APPR.
MFG APPR.
Q.A.
COMMENTS:

NEXT ASSY | USED ON
APPLICATION

DO NOT SCALE DRAWING

TITLE:
Bearing Finger Tip

SIZE | DWG. NO. | REV
A

SCALE: 1:1 | WEIGHT: | SHEET 1 OF 1

153

Ø.30
Ø.190
Ø.150

.75
.15
.15

Ø.25

Ø.15 ▽.31
10-24 UNC - 2B ▽.10

5   4   3   2   1

154

Appendix D: MATLAB Code for Stability Analysis

MATLAB Sample Code for 1-DOF Stability Analysis

```
% Analytical 1–DOF stability analysis with multiple positions
% Varying only the angle of theta2

close all;
clear all;
clc;

% ---------------------------------------------------------------------------
% PART I: VARIABLES THAT DON'T CHANGE, OR ARE ONLY SUBSTITUTED LATER
% ---------------------------------------------------------------------------
% for Laplace domain:
syms s

% identity matrix:
% I = eye(2);
syms I H1 H2
I = 1;

% Delay 1:
H1 = 1 % No delay
% Delay 2:
H2 = 1 % No delay


% ------------------------------------------------------------
% Joint angles and link parameters
% ------------------------------------------------------------
syms angles theta1 theta2
angles = [0 15 30 45 60 90 120 150 170] %degrees
angles = angles*3.141592654/180        %radians

% trigonometry:
syms s1 s2 s12 c1 c2 c12
s1 = sin(theta1);
s2 = sin(theta2);
s12 = sin(theta1+theta2);
c1 = cos(theta1);
c2 = cos(theta2);
c12 = cos(theta1+theta2);

syms L_L1 L_L2 L1 L2 L3 Lp m1 m2 m3 payload
% Link lengths:
% For jacobian:
% L_L1 = 1.2;   % Link1 Extended
% L_L2 = 1.2;   % Link2 Extended
L_L1 = 0.54;    % Actual length of link 1
L_L2 = 0.677;   % Actual length of link 2 (to payload)
% For inertia:
% ----- Ranger DXR -------------
L1 = 0.0572;    % metres, to m1
L2 = 0.0762;    % metres, to m2
L3 = 0.446;     % metres, to m3
Lp = 0.677;     % metres, to payload
% ----- Extended Config ---------
% L1 = 0.0572;   % metres, to m1
% L2 = 0.0762;   % metres, to m2
% L3 = 0.98;     % metres, to m3
% Lp = 1.2;      % metres, to payload
```

```
% Link masses (for inertia calculation)
m1 = 22.68;     % kg
m2 = 21.90;     % kg
m3 = 21.90;     % kg
payload = [0 1 5 15];% kg (analysis done for varying payload)


% -------------------------------------------------------------
% Jacobian:
% -------------------------------------------------------------

syms J JT Jinv
J = 1;
JT = 1;
Jinv = 1;


% -------------------------------------------------------------
% P-D gains (default values from rtsx/common/src/CFG.C)
% -------------------------------------------------------------

syms Kp Kv
syms D1 D2 D
K_motor = 0.159;   % motor current to Nm
DAC = 20/4096;      % raw torque to motor current
Counts = 43726;     % radians to counts
Gear = 101;          % Gear ratio
Kv = 25*Gear*Counts*DAC*K_motor/64;
Kp = 5*Gear*Counts*DAC*K_motor;
D1 = Kv*s + Kp;
D2 = Kv*s + Kp;

% PD Controller:
D = D1;


% -------------------------------------------------------------
% Impedance stiffness, inertia and damping terms
% -------------------------------------------------------------

syms Kx Ky Bx By Mx My b k m
syms C1 C2 C K
Kx = k;
Ky = k;
Bx = b;
By = b;
Mx = m;
My = m;

C1 = 1/(Mx*s^2+Bx*s);
C2 = 1/(My*s^2+By*s);

% Admittance Compensator:
C = C1;

% Admittance Stiffness:
K = Kx;

% Enviroment Stiffness:
syms Kenvir
Kenvir = [0 100 1000 10000 25000];


% ----------------------------------------------------------------------------
% PART II: SETTING UP VARIABLES THAT CHANGE IN THE ANALYSIS
% ----------------------------------------------------------------------------

qstart = 2;     % The joint angle index for theta2
qend = 9;   % The number of joint angles used (9 = maximum)
qstep = 1;
```

```matlab
estart = 5;      % The environment stiffness index
eend = 5;   % The number of stiffnesses used (5 = maximum)
estep = 1;
pstart = 1;      % The payload mass index
pend = 1;   % The number of payloads used (4 = maximum)
pstep = 1;

qnum = (qend-qstart)/qstep + 1;
enum = (eend-estart)/estep + 1;
pnum = (pend-pstart)/pstep + 1;

iters = round(qnum*enum*pnum)

% for counting iterations
iter = 0;

for q=qstart:qstep:qend
    for e=estart:estep:eend
        for p=pstart:pstep:pend

            % ------------------------------------------------------------
            % Environment stiffness
            % ------------------------------------------------------------
            syms Kenv Ke
            Kenv = Kenvir(e)
            Ke = Kenv;

            % Equivalent Stiffness:
            syms Keq
            Keq = K + Ke;

            % ------------------------------------------------------------
            % Motor inertia and damping terms
            % ------------------------------------------------------------

            syms Jm Bm N
            Jm = 4.8e-4;
            Bm = 2.3e-5;    % From motor data sheets
            N = 101;
            syms L21   % Lengths used for inertia calculation
            syms JL1 JL2 BL BL
            syms Jp1 Jp2 Bp1 Bp2
            syms Gp1 Gp2
            syms mp m2eq L2eq L21

            mp = payload(p);

            m2eq = m2+m3+mp;
            L2eq = (m2*L2+m3*L3+mp*Lp)/m2eq;
            L21 = sqrt(L_L1^2 + L2eq^2 + 2*L_L1*L2eq*c2); % Law of cosines

            JL1 = m1*(L1^2) + m2eq*(L21^2)
            JL2 = m2eq*(L2eq^2);

            Jp1 = Jm*(N^2)+JL1;
            Jp2 = Jm*(N^2)+JL2;
            Bp1 = Bm*(N^2);
            Bp2 = 0;
            Kp1 = 0;
            Kp2 = 0;

            Gp1 = 1/(Jp1*s^2+Bp1*s+Kp1);    % Getting theta from torque
            Gp2 = 1/(Jp2*s^2+Bp2*s+Kp2);

            % Plant model (simplified motor model)
            syms Gp
            %Gp = [Gp1 0;0 Gp2];
```

```
            Gp = Gp1;

            % Inner loop model:
            syms Gt
            Gt = Gp*H1*D/(I + Gp*(H1*D + JT*Ke*J));
            vpa(Gt)
            fprintf('\nGt =')
            pretty(vpa(Gt))

            % Overall Transfer function with Impedance loop:
            syms Gx
            Gx = J*Gt*H2*Jinv*(I + C*K)/(I + J*Gt*H2*Jinv*C*Keq);
            vpa(Gx)
            fprintf('\nGx =')
            pretty(vpa(Gx))

            % With bias force:
            syms Gf
            Gf = J*Gt*H2*Jinv*C*(inv(I + J*Gt*H2*Jinv*C*Keq));


            % --------------------------------------------------------------------------
            % PART III: OBTAINING CHAR EQNS AND PLOTS OF STABILITY MARGINS
            % --------------------------------------------------------------------------

            syms CharEq1 R1 q1 Eq1 K1 K1a
            Gx = simple(Gx);
            Gx = subs(Gx,m,0);  % m = 0, for now
            Gx = simple(Gx);
            if (Gx~=0)
                [NUM1,DEN1] = numden(Gx);
                CharEq1 = DEN1;
                CharEq1 = subs(CharEq1,theta1,angles(1));
                CharEq1 = subs(CharEq1,theta2,angles(q)); % later make this angles(n)
                CharEq1 = collect(CharEq1,s);
                [q1,r1] = coeffs(CharEq1,s)

                polyq1 = [q1(4),q1(3),q1(2),q1(1)];
                syms EPS
                RA1 = routh(polyq1,EPS)
                Eq1 = 0;
                Eq1 = RA1(3,1)

                K1 = solve(Eq1,k);
                K1a = collect(expand(K1(1)),b);
                K1a = vpa(eval(K1a));

                figure(1);
                if (length(K1)>1)
                    subplot(2,1,1)
                end
                ezplot(K1a,[0 2000])
                if (iter<1)
                    setcurve('color','green','linestyle','--');
                end
                if (iter>iters-2)
                    setcurve('color','red','linestyle','-.');
                end
                title('Effect of \theta_2 on Shoulder Joint Stability')
                xlabel('B (Nms/rad)')
                ylabel('K (Nm/rad)')
                hold on;
            end
            iter = iter +1
        end % Payload for-loop
    end % Stiffness for-loop
end % Joint Angle for-loop
```

158

MATLAB Sample Code for 2-DOF Stability Analysis

```
% ----------------------------------------------------------
% Joint angles and link parameters
% ----------------------------------------------------------
% Setup for different angles:
angles = [0 15 30 45 60 90 120 150 170] %degrees
angles = angles*pi/180       %radians

% trigonometry:

for theta1=1:1:length(angles)
   for theta2=1:1:length(angles)
      s1(theta1,theta2) = sin(angles(theta1));
      if (s1(theta1,theta2)<1e-6)
         s1(theta1,theta2) = 0;
      end
      s2(theta1,theta2) = sin(angles(theta2));
      if (s2(theta1,theta2)<1e-6)
         s2(theta1,theta2) = 0;
      end
      s12(theta1,theta2) = sin(angles(theta1)+angles(theta2));
      if (s12(theta1,theta2)<1e-6)
         s12(theta1,theta2) = 0;
      end
      c1(theta1,theta2) = cos(angles(theta1));
      if (c1(theta1,theta2)<1e-6)
         c1(theta1,theta2) = 0;
      end
      c2(theta1,theta2) = cos(angles(theta2));
      if (c2(theta1,theta2)<1e-6)
         c2(theta1,theta2) = 0;
      end
      c12(theta1,theta2) = cos(angles(theta1)+angles(theta2));
      if (c12(theta1,theta2)<1e-6)
         c12(theta1,theta2) = 0;
      end
   end
end

% Link lengths:
% For jacobian:
L_L1 = 1.2;    % Extended Arm
L_L2 = 1.2;    % Extended Arm
% L_L1 = 0.54;    % Actual length of link 1
% L_L2 = 0.677;   % Actual length of link 2 (to payload)
% For inertia:
% ------------ Extended Arm -------------
L1 = 0.0572;   % metres, to m1
L2 = 0.0762;   % metres, to m2
L3 = 0.98;     % metres, to m3
Lp = 1.2;      % metres, to payload

% ------------ RTSX Arm Config-------------
% L1 = 0.0572;    % metres, to m1
% L2 = 0.0762;    % metres, to m2
% L3 = 0.446;     % metres, to m3
% Lp = 0.677;     % metres, to payload

% Link masses (for inertia calculation)
m1 = 22.68;    % kg
m2 = 21.90;    % kg
m3 = 21.90;    % kg
```

```
payload = [1 5 10 20];
% payload = [60 70 80 100];% kg (analysis done for varying payload)


% ------------------------------------------------------------
% Jacobian:
% ------------------------------------------------------------

% use tool-tip jacobian

for theta1=1:length(angles)
   for theta2=1:length(angles)
      J11(theta1,theta2) = L_L1*s2(theta1,theta2);
      J12(theta1,theta2) = 0;
      J21(theta1,theta2) = L_L1*c2(theta1,theta2)+L_L2;
      J22(theta1,theta2) = L_L2;
   end
end


% ------------------------------------------------------------
% P-D gains (default values from rtsx/common/src/CFG.C)
% ------------------------------------------------------------

% used values that make the inner-loop controller stable

K_motor = 0.159;   % motor current to Nm
DAC = 20/4096;     % raw torque to motor current
Counts_1 = 43726;    % radians to counts of shoulder
Counts_2 = 33114;    % radians to counts of elbow
Gear = 101;        % Gear ratio
Kv1 = 25*Gear*Counts_1*DAC*K_motor/64;
Kp1 = 5*Gear*Counts_1*DAC*K_motor;
Kv2 = 25*Gear*Counts_2*DAC*K_motor/64;
Kp2 = 5*Gear*Counts_2*DAC*K_motor;

D1 = tf([Kv1 Kp1],[1]);
D2 = tf([Kv2 Kp2],[1]);

% PD Controller:

D = [D1 0;0 D2];

% ------------------------------------------------------------
% Corrective factor:
% ------------------------------------------------------------

% cf = 0; % Pelletier and Doyon use 0.75

% for equivalent damping
% C = C/(1-cf)


% --------------------------------------------------------------------------
% PART II: SETTING UP VARIABLES THAT CHANGE IN THE ANALYSIS
% --------------------------------------------------------------------------

qstart = 5;     % The joint angle index for theta2
qend = 5;   % The number of joint angles used (9 = maximum)
qstep = 1;
estart = 1;     % The environment stiffness index
eend = 4;   % The number of stiffnesses used (5 = maximum)
estep = 1;
pstart = 4;     % The payload mass index
pend = 4;   % The number of payloads used (4 = maximum)
pstep = 1;

qnum = (qend-qstart)/qstep + 1;
```

160

```
enum = (eend-estart)/estep + 1;
pnum = (pend-pstart)/pstep + 1;

iters = round(qnum*enum*pnum)

% for counting iterations
iter = 0;
figure(1)
title('Region of Stability for Varying \theta_2')

for q=qstart:qstep:qend
    for e=estart:estep:eend
        for p=pstart:pstep:pend
            subplot(2,2,iter+1)
            for k=1:200:1001
                for b = 1:50:1001


                    % ------------------------------------------------------------
                    % Impedance stiffness, inertia and damping terms
                    % ------------------------------------------------------------
                    % (we'll want a range of these, for comparison)
                    C1 = tf([1],[b 0]);
                    C2 = C1;

                    % Admittance Compensator:
                    C = [C1 0;0 C2];

                    % Admittance Stiffness:
                    K = [k 0;0 k];

                    % Enviroment Stiffness:
                    Kenvir = [0 100 1000 10000 25000]; %Gt become unstable at Kenv = 220000
                    Kenvir = [0 500 10000 25000]


                    % ------------------------------------------------------------
                    % Environment stiffness
                    % ------------------------------------------------------------
                    Kenv = Kenvir(e)
                    Ke = [Kenv 0;0 0];
                    %Ke = [Kenv 0;0 0]; % for x force only
                    %Ke = [0 0;0 Kenv]; % for y force only


                    % Equivalent Stiffness:
                    syms Keq
                    Keq = K + Ke;

                    % ------------------------------------------------------------
                    % Motor inertia and damping terms
                    % ------------------------------------------------------------

                    Jm = 4.8e-4;
                    Bm = 2.3e-5;
                    N = 101;

                    mp = payload(p)

                    m2eq = m2+m3+mp;
                    L2eq = (m2*L2+m3*L3+mp*Lp)/m2eq;
                    L21 = sqrt(L_L1^2 + L2eq^2 + 2*L_L1*L2eq*c2(1,q)); % Law of cosines

                    JL1 = m1*(L1^2) + m2eq*(L21^2)
                    JL2 = m2eq*(L2eq^2);

                    Jp1 = Jm*(N^2)+JL1
```

161

```matlab
        Jp2 = Jm*(N^2)+JL2
        Bp1 = Bm*(N^2);   %2.3e-5;    % zero damping, as per Jenny Smith's thesis
        Bp2 = Bm*(N^2);   %2.3e-5;    % 2.3e-5 as per motor data sheets

        Gp1 = tf([1],[Jp1 Bp1 0]);
        Gp2 = tf([1],[Jp2 Bp2 0]);

        % Plant model (simplified motor model)
        Gp = [Gp1 0;0 Gp2];

        % Jacobian:
        J = [J11(1,q) J12(1,q);J21(1,q) J22(1,q)];
        JT = transpose(J);
        Jinv = inv(J);

        I = eye(2,2);

        % Inner loop model:
        syms Gt
        Gt = Gp*D*(inv(I + Gp*(D + JT*Ke*J)));

        % Overall Transfer function with Impedance loop:
        syms Gx
        Gx = J*Gt*Jinv*(I + C*K)*(inv(I + J*Gt*Jinv*C*Keq));
        poles1 = pole(Gx(2,1));
        poles1 = real(poles1);
        hold on;
        for i=1:length(poles1)
           if (abs(poles1(i))<1e-6)
              poles1(i) = 0;
           end
           check_stab1 = sign(poles1(i))
           if (check_stab1 == 1)
              plot(b,k,'rx','MarkerSize',10)
              break
           end
        end
        if (check_stab1 ~= 1)
           plot(b,k,'go','MarkerSize',10)
        end
      end % k loop
    end % b loop
    iter = iter +1
    axis([0 1001 0 1001])
    xlabel('B (Ns/m)')
    ylabel('K (N/m)')
    title(['k_e_n_v = ',num2str(Kenv),' N/m'])
  end % Payload for loop
 end % Stiffness for loop
end % Joint Angle for loop
```

162

MATLAB Sample Code for Bandwidth Calculation

Begins after the transfer functions are calculated in the 1-DOF stability code

```
% -------------------------------------------------------------------------
% PART III: FINDING SYSTEM BANDWIDTH
% -------------------------------------------------------------------------

        Gx = simple(Gx);
        Gx = subs(Gx,m,0);  % m = 0, for now
        Gx = subs(Gx,theta1,angles(1));
        Gx = subs(Gx,theta2,angles(q));
        Gx = simple(Gx);
        Jp = subs(Jp1,theta2,angles(q));

        syms EqNum EqDen
        [NUM1,DEN1] = numden(Gx);
        EqNum = NUM1;
        EqDen = DEN1;

        index = 1;
        figure;

        for u=1:499:500
          for v=1:999:1000
            numtest = Kv*b*s^2 + (Kv*k+b*Kp)*s + Kp*k;
            dentest = b*Jp*s^3 + Kv*b*s^2 + ((Kp+Ke)*b+Kv*(k+Ke))*s + Kp*(K+Ke);
            numtest = subs(numtest,k,u);
            numtest = subs(numtest,b,v);
            dentest = subs(dentest,k,u);
            dentest = subs(dentest,b,v);
            numtest = sym2poly(numtest);
            dentest = sym2poly(dentest);
            sys = tf(numtest,dentest);
            subplot(2,2,index)
            bodemag(sys);
            title(['Bode Diagram for K = ',num2str(u),' Nm/rad, B = ',num2str(v),' Nms/rad'])
            hold on;
            bw(iter,index) = bandwidth(sys)/2/pi;
            index = index +1;
          end
        end
```

References

[1] Christian Sallaberger, "Space Robotics". Larson, Wiley J., and Pranke, Linda K., *Human Spaceflight: Mission Analysis and Design* (pp. 739-759), McGraw-Hill, New York, NY, 1999

[2] Volpe, Richard, "Techniques for Collision Prevention, Impact Stability, and Force Control by Space Manipulators". Skaar, Steven B., Ruoff, Carl F., *Teleoperation and Robotics in Space* (pp. 175-212), Progress in Astronautics and Aeronautics, Vol. 161, AIAA, 1994

[3] Raibert, M.H. and Craig, J.J., "Hybrid Position/Force Control of Manipulators", *Journal of Dynamic Systems, Measurement, and Control*, Vol. 102, pp. 126-133, ASME, June 1981

[4] Hogan, N., "Impedance Control, An Approach to Manipulation: Part I-III", *Journal of Dynamic Systems, Measurement, and Control*, Vol. 107, pp 1-24, ASME, 1985

[5] DiMaio, S.P., Hashtrudi-Zaad, K., Salcudean, S.E., "Optimal Selection of Manipulator Impedance for Contact Tasks", Proc. IEEE Conference on Robotics and Automation, 2004

[6] Carignan, C.R., Smith, Jennifer, A., "Manipulator Impedance Accuracy in Position-Based Impedance Control Implementations" Proc. IEEE Conference on Robotics and Automation, 1994

[7] Smith, Jennifer A., "Position-Based Impedance Control Tracking in Space Manipulator Applications", M.S. Thesis, University of Maryland, College Park, MD, 1994

[8] Carignan, C.R., Akin, D.L., "Achieving Impedance Objectives in Robot Teleoperation" Proc. IEEE Conference on Robotics and Automation, 1997

[9] Zeng, G and Hemami, A., "An overview of robot force control", Robotica, Vol. 15, pp. 473-482, 1997

[10] Hutchinson, S., Spong, M.W., Vidyasagar, M., *Robot Modeling and Control*, John Wiley & Sons, Inc., Hoboken, NJ, 2006

[11] Salisbury, J.K., "Active Stiffness Control of a Manipulator in Cartesian Coordinates" Proc. IEEE Conference on Decision and Control, 1980

[12] Whitney, D.E., "Historical Perspective and State of the Art in Robot Force

Control", Proc. IEEE Conference on Robotics and Automation, 1985

[13]   An, C.H., Hollerbach, J.M., "Dynamic Stability Issues in Force Control of Manipulators", Proc. IEEE Conference on Robotics and Automation, 1987

[14]   Anderson, R.J., Spong, M.W., "Hybrid Impedance Control of Robotic Manipulators", *IEEE Journal of Robotics and Automation*, Vol. 4, October 1988

[15]   Pelletier, M., Doyon, M., "On the Implementation and Performance of Impedance Control on Position Controlled Robots", Proc. IEEE Conference on Robotics and Automation, 1994

[16]   Sakaki, T., Iwakane, T., Tachi, S., "Impedance Control of a Robot Manipulator Satbilized by PID Endpoint Motion Compensation", Proc. International Symposium on Measurement and Control in Robotics, 1992

[17]   Maples, J.A., Becker, J.J., "Experiments in Force Control of Robotic Manipulators", Proc. IEEE Conference on Robotics and Automation, 1986

[18]   Lawrence, D.A., "Impedance Control Stability Properties in Common Implementations", Proc. IEEE Conference on Robotics and Automation, 1988

[19]   Biagiotti, L., Liu, H., Hirzinger, G., Melchiorri, C., "Cartesian Impedance Control for Dexterous Manipulators", Proc. IEEE/RSJ International Conference on Intelligent Robots and Systems, 2003

[20]   Glosser, G.D., Newman, W.S., "The Implementation of a Natural Admittance Controller on an Industrial Manipulator", Proc. IEEE Conference on Robotics and Automation, 1994

[21]   Dohring, M., Newman, W., "Admittance Enhancement in Force Feedback of Dynamic Systems", Proc. IEEE Conference on Robotics and Automation, 2002

[22]   Dohring, M., Newman, W., "The Passivity of Natural Admittance Control Implementations", Proc. IEEE Conference on Robotics and Automation, 2003

[23]   Naksuk, N., "The Implementation of a Natural Admittance Controller on an Industrial Manipulator", M.S. Thesis, Case Western Reserve University, Cleveland, OH, 2000

[24]   Carignan, C.R., Cleary, K.R., "Closed-Loop Force Control for Haptic Simulation of Virtual Environments", *Haptics-e*, Vol. 1, February 2000

[25]   Love, L. and Book, W., "Environment Estimation for Enhanced Impedance

Control", Proc. IEEE Conference on Robotics and Automation, 1995

[26] Diolatti, N., Melchiorri, C., Stramiglioli, S., "Contact Impedance Estimation for Robotic Systems", *IEEE Transactions on Robotics*, Vol. 21, October 2005

[27] Surdilovic, D., "Contact Transition Stability in the Impedance Control", Proc. IEEE Conference on Robotics and Automation, 1997

[28] Seraji, H., Colbaugh, R., "Adaptive Force-Based Impedance Control", Proc. IEEE Conference on Robotics and Automation, 1993

[29] Guion, Peter, "Impedance Control with Friction Adaptation for a Two Link Robotic Manipulator", M.S. Thesis, University of Maryland, College Park, MD, 2003

[30] Gershon, D., Baruch, V., "Impedance Control with Autonomous Mode Switching", Proc. IEEE Conference on Robotics and Automation, 1991

[31] Volpe, R. and Khosla, P., "Experimental Verification of a Strategy for Impact Control", Proc. IEEE Conference on Robotics and Automation, 1991

[32] Carignan, C.R., Howard, R., "A Partitioned Redundancy Management Scheme for an Eight Joint Revolute Manipulator", *Journal of Robotic Systems*, Vol. 17, pp 453-468, 2000

[33] Kreutz-Delgado, K., Long, M., and Seraji, H., *Kinematic Analysis of 7 DOF Manipulators.* International Journal of Robotics Research, Vol. 11, No. 5, 1992, pp. 469-481.

[34] Naylor, Michael P., "Autonomous Target Recognition and Localization for Manipulator Sampling Tasks", M.S. Thesis, University of Maryland, College Park, MD, 2006

[35] Craig, John J., *Introduction to Robotics*, 3rd ed., Prentice Hall, Upper Saddle River, NJ, 2005

[36] Sciavicco, L. and Siciliano, B., *Modelling and Control of Robot Manipulators*, 2nd ed., Spinger-Verlag, London, England, 2000

[37] Roderick, S. or Smith, W., DT21-0039 Test Report: Ranger Static Performance Measurements, Space Systems Laboratory internal document #06-005

[38] Roderick, S. or Smith, W., DT21-0041 Test Report: Ranger Dynamic Performance Measurements, Space Systems Laboratory internal document #06-006

[39]   Roderick, S. or Smith, W., Test Report: Arm Dimensions and Weight Measures, Space Systems Laboratory internal document #07-006

[40]   Roderick, S., Henriette, J.M., DT07-9026 Encoder Conversion v0.7, Space Systems Laboratory internal document, 2003

[41]   Ogata, K., *Modern Control Engineering*, 4th ed., Prentice Hall, Upper Saddle River, NJ, 2002

[42]   Aksman, Leon, "Force Estimation Based Compliance Control of a Two Link Harmonically Driven Robotic Manipulator", M.S. Thesis, University of Maryland, College Park, MD, 2006